AD-A086 697   PRATT AND WHITNEY AIRCRAFT GROUP WEST PALM BEACH FL G--ETC   F/G 11/6
PLASTIC FLOW AND FRACTURE PROCESSES IN POWDER METALLURGICAL NIC--ETC(U)
FEB 80   C C LAW, M J BLACKBURN   F49620-77-C-0083
UNCLASSIFIED   PWA-FR-13317   AFOSR-TR-80-0468   NL

1 OF 2
AD
A086697

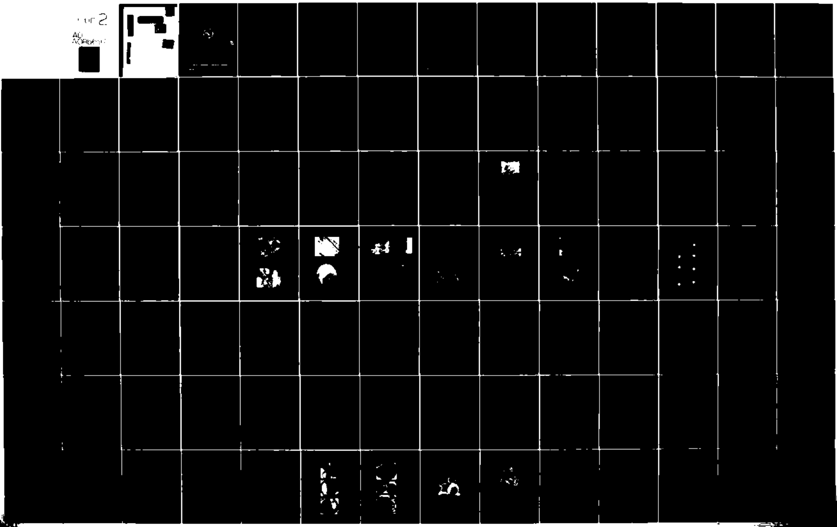

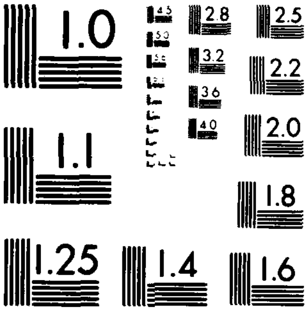
1.0
4.5
5.0
5.6
6.3
7.1
8.0
9.0
2.8
3.2
3.6
4.0
2.5
2.2
2.0
1.1
1.8
1.25
1.4
1.6

MICROCOPY RESOLUTION TEST CHART
NATIONAL BUREAU OF STANDARDS-1963-A

(11)

PLASTIC FLOW AND FRACTURE PROCESSES IN
POWDER METALLURGICAL NICKEL-BASE
SUPERALLOYS

AFOSR-TR- 80-0468

FINAL REPORT

LEVEL II

ADA086697

DDC FILE COPY

DTIC
ELECTE
JUL 7 1980
S C D

(11)

PLASTIC FLOW AND FRACTURE PROCESSES IN POWDER METALLURGICAL NICKEL-BASE SUPERALLOYS

AFOSR-TR- 80-0468

FINAL REPORT

March 1, 1977-February 29, 1980

UNITED STATES AIR FORCE OFFICE OF SCIENTIFIC RESEARCH
BUILDING 140
BOLLING AIR FORCE BASE, D.C. 20332

F49620-77-C-0083

DTIC
ELECTE
JUL 7 1980
S D
C

PREPARED BY:

C. C. LAW AND M. J. BLACKBURN

MATERIALS ENGINEERING & RESEARCH LABORATORY

AIR FORCE OFFICE OF SCIENTIFIC RESEARCH (AFSC)
NOTICE OF TRANSMITTAL TO DDC
This technical report has been reviewed and is approved for public release IAW AFR 190-12 (7b).
Distribution is unlimited.
A. D. BLOSE
Technical Information Officer

PRATT & WHITNEY AIRCRAFT GROUP
Government Products Division
P. O. Box 2691
West Palm Beach, Florida 33402
UNITED TECHNOLOGIES®

80 7 2 098

Printed in the United States of America

REF. NO. EII 80-200-7053-FR

This document printed on recycled paper

Unclassified

SECURITY CLASSIFICATION OF THIS PAGE (When Data Entered)

(19) REPORT DOCUMENTATION PAGE	READ INSTRUCTIONS BEFORE COMPLETING FORM
~~1. REPORT NUMBER~~ (18) AFOSR-TR-80-0468	2. GOVT ACCESSION NO. AD-A086697
3. RECIPIENT'S CATALOG NUMBER	
4. TITLE (and Subtitle) (6) Plastic Flow and Fracture Processes in Powder Metallurgical Nickel-Base Superalloys.	5. ~~TYPE OF REPORT & PERIOD~~ COVERED (9) Final Report, (1) Mar [redacted]77-Feb [redacted]80
	6. ~~PERFORMING ORG. REPORT NUMBER~~ (14) PWA-FR-13317 (21)
7. AUTHOR(s) (10) C. C. Law [redacted] M. J. Blackburn	8. ~~CONTRACT OR~~ GRANT NUMBER(s) (15) F49620-77-C-0083
9. PERFORMING ORGANIZATION NAME AND ADDRESS United Technologies Corporation Pratt & Whitney Aircraft Group Government Products Division, West Palm Beach, FL	10. PROGRAM ELEMENT, PROJECT, TASK AREA & WORK UNIT NUMBERS 61102F (16) 2306/A1
11. CONTROLLING OFFICE NAME AND ADDRESS Air Force Office of Scientific Research /NE Bolling Air Force Base D. C. 20322	12. ~~REPORT DATE~~ (11) Feb [redacted]80
	13. NUMBER OF PAGES 127
14. MONITORING AGENCY NAME & ADDRESS (if different from Controlling Office) (17) A1	15. SECURITY CLASS. (of this report) Unclassified
	15a. DECLASSIFICATION/DOWNGRADING SCHEDULE

16. DISTRIBUTION STATEMENT (of this Report)

Approved for public release;
distribution unlimited.

(12) 131

17. DISTRIBUTION STATEMENT (of the abstract entered in Block 20, if different from Report)

18. SUPPLEMENTARY NOTES

19. KEY WORDS (Continue on reverse side if necessary and identify by block number)

Nickel-Base Superalloys, Powder Metallurgy, Hot Isostatic Pressing, Creep and Rupture Properties, Fracture, Ductility, Notched Section Properties, Mesh Size, Stress Relaxation, Life Improvement, Low Cycle Fatigue, Nonmetallic Inclusions, Fracture Mechanics, Crack Initiation, Crack Propagation

20. ABSTRACT (Continue on reverse side if necessary and identify by block number)

The advent of powder metallurgical methods for nickel-base superalloys has made it possible to use high-strength alloys for large components such as turbine disks. Although much of the manufacturing and process technology for such products is reasonably well understood, many of the features of the structure-property relationships in these alloys remain unclear. This document describes the results of a three-year effort undertaken to provide insight into the factors that control specific properties in advanced powder

DD FORM 1 JAN 73 1473 EDITION OF 1 NOV 65 IS OBSOLETE

Unclassified 392 887

Jm

20 metallurgical nickel-base superalloys. The first-year effort examined the stress-rupture characteristics of smooth sections of a number of alloys including AF115 and MERL 76. It was concluded that the ability of a material to store dislocations controls the creep rate but that the fracture processes were dictated by grain boundary structures. Models that satisfactorily accounted for the behavior pattern were developed. The second-year effort extended the study to notch-rupture properties which were found to depend upon a larger number of variables. An interesting parallel between short notch lives and the fracture times of smooth sections tested under stress relaxation was found. Based on this observation, certain mechanical criteria for poor notch characteristics could be identified. However, a complete theory will have to include environmental and structural parameters that can only be qualitatively expressed at present. Another segment of the second-year effort dealt with the influence of mesh size on properties of MERL 76; the use of finer meshes will reduce the defect sizes and improve fatigue capability. It was shown that mesh fractions as fine as -325 mesh yielded acceptable mechanical properties. The third-year program considered in more detail the influence of defects on fatigue properties of MERL 76. Oxides of aluminum and magnesium were chosen for evaluation as typical of species found in powder metallurgical superalloys. Anticipated effects of thermally induced local stress fields and inclusion shape were not found. On the contrary, detailed measurements of the early stages of crack formation and growth showed that they were virtually independent of these parameters. The results could be more closely approximated by assuming that inclusions acted as notches rather than cracks. An analytical procedure to bound the fatigue results was established and successfully applied.

TABLE OF CONTENTS

Page

1.0 GENERAL INTRODUCTION 1

2.0 FIRST-YEAR PROGRAM: CREEP-RUPTURE IN POWDER METALLURGICAL NICKEL-BASE SUPERALLOYS AT INTERMEDIATE TEMPERATURES

- 2.1 INTRODUCTION 3
- 2.2 EXPERIMENTAL 5
- 2.3 RESULTS 7
- 2.4 DISCUSSION 14
- 2.5 CONCLUSIONS 21
- REFERENCES 22
- TABLES 24
- FIGURES 28

3.0 SECOND-YEAR PROGRAM: MESH SIZE EFFECTS AND NOTCH STRESS-RUPTURE PROPERTIES OF MERL 76

- 3.1 INTRODUCTION 51
- 3.2 EXPERIMENTAL 52
- 3.3 EFFECTS OF MESH SIZE ON THE MICROSTRUCTURES AND PROPERTIES OF MERL 76
  - 3.3.1 INTRODUCTION 53
  - 3.3.2 RESULTS 53
  - 3.3.3 CONCLUSIONS 55
- 3.4 NOTCH-RUPTURE PROPERTIES OF MERL 76 - PHENOMENOLOGY AND ANALYSIS
  - 3.4.1 INTRODUCTION 56
  - 3.4.2 NOTCH-RUPTURE BEHAVIOR 56
  - 3.4.3 ANCILLARY TESTS 60

3.4.4 DISCUSSION 61

3.4.5 CONCLUSIONS 67

APPENDIX 68

REFERENCES 70

TABLES 71

FIGURES 80

4.0 THIRD-YEAR PROGRAM: EFFECT OF NONMETALLIC INCLUSIONS ON FATIGUE PROPERTIES OF A NICKEL-BASE SUPERALLOY

4.1 INTRODUCTION 97

4.2 EXPERIMENTAL 99

4.3 RESULTS 100

4.4 DISCUSSION 104

4.5 CONCLUSIONS 107

REFERENCES 108

TABLES 109

FIGURES 113

ACKNOWLEDGEMENTS 127

Accession For
NTIS ☑
DDC TAB ☐
Unannounced ☐
Justific
By
Distri
Availa
Dist. Av
A

SECTION 1.0 GENERAL INTRODUCTION

Current and future powerplants for use in Air Force systems require the use of advanced materials. The operational factors set by the specific aircraft type and mission profile in turn control the properties demanded in engine components. Properties required in components will differ and the situation is further complicated by varying requirements with location in a given part. This is especially true in large components such as a turbine disk. The disk rim which is closest to the gas path demands superior creep-rupture characteristics. The disk bore, which operates at lower temperatures, requires high tensile strength to resist plastic displacements and maintain an adequate burst margin. For turbine disks, high rotational speeds and rim temperatures result in increased engine efficiency and thus the specific material properties noted above must be optimized. Turbine disks operate under cyclic loads, viewed simply one complete mission corresponds to one fatigue cycle. The ability of a disk to tolerate repeated cycles can be related to engine maintenance and life cycle costs which include inspection, overhaul, replacement, etc. A final point of importance in a discussion of disks is acquisition cost, which is determined by the process cycle used for disk fabrication. Selection of a minimum cost procedure, capable of achieving the property requirements in the finished disk, impacts the cost effectiveness of the total system.

These three areas of turbine disk technology, performance, durability, and acquisition cost are implicit in current and projected Air Force Programs. Pratt & Whitney Aircraft has also structured a development program, which has many objectives common to those of the Air Force Program. One direct method of accomplishing intermeshing of these programs is through contractural efforts,and this document is concerned with one such program. It deals with a basic study aimed at elucidating some of the processes and mechanisms that control certain properties of alloys used in turbine disks.

Nickel-base superalloys, because of their unique elevated temperature properties,are used exclusively for high pressure turbine disks. The advent of powder metallurgical (P/M) techniques for such alloys has opened up new areas of alloy composition and processing. Barriers such as ingot heterogeneity and forging problems in high strength alloys have been circumvented by the use of alloys in the powder form. Although several fabrication methods have been proven to be effective, direct consolidation of powders by hot isostatic pressing (HIP) has been shown to be the most cost effective method of disk fabrication. These changes in the raw material (powder) and manufacturing method (HIP) lead to property-structural relationships whichdiffer from the more conventional wrought products. This document describes a program which was undertaken to evaluate selected aspects of the processing and properties of powder metallurgy alloys. Several alloys were included in the study, but a high strength disk alloy based on IN100 and designated MERL 76 was studied most extensively. In the first year of the program, the basic property chosen for study was the stress-rupture characteristics of this class of material. The second-year effort considered further aspects of the notch rupture and the modification of properties that may occur by utilizing a finer mesh powder to make consolidations. This practice has been suggested as a method of alleviating problems encountered in P/M alloys which were traced to small non-metallic inclusions in powders. Such inclusions can act as nuclei for stress-rupture cracks and, more importantly, exert a dominant influence on fatigue properties. A comprehensive study of inclusion effects on fatigue capability was selected for the third year of the program. Each of these projects is described in a separate section in this document, which has been so structured that each topic can be read independently.

SECTION 2.0 FIRST-YEAR PROGRAM

CREEP-RUPTURE IN POWDER METALLURGICAL NICKEL-BASE SUPERALLOYS AT INTERMEDIATE TEMPERATURES

2.1 INTRODUCTION

In an earlier paper(1) some of the requirements for turbine components that operate at intermediate temperatures (650-775°C) were described, and the need for good creep and stress-rupture capability was noted. The paper also described an alloy development program on nickel-base superalloys in the powder form which had the goal of achieving superior tensile and creep properties. A second requirement for these alloys was that the powder metallurgical (P/M) product should be processable by hot isostatic pressing (HIP), one of the newer and more cost-effective fabrication procedures(2). A large number of alloys were screened in the course of the development program and a surprising feature of the results was the large range of creep-rupture properties measured in various material groups. For example, an alloy series based on the MAR-M432 composition had poor properties, while AF115 showed rupture lives up to three orders of magnitude longer than the MAR-M432 alloys. Both AF115 and modified MAR-M432 alloys exhibited rather low rupture ductilities. On the other hand, a modified IN100 alloy designated MERL 76 showed a combination of good rupture life and ductility. It is considered that an explanation of these differences would not only be of intrinsic interest, but also could be most useful for any further development efforts.

In this report we shall deal with the creep-rupture properties of smooth sections of P/M superalloys. The process of stress rupture consists of the nucleation and growth of cracks until a condition for overload failure is reached. There has been a recent trend to emphasize the crack growth part of the process. It will be shown that under the conditions studied in the present investigation the crack nucleation stage comprised a considerable fraction of the life. Thus, although independent crack growth measurements were made, we shall attempt to account for all stages leading to the failure of a specimen.

It is usual in introducing a report to review briefly the previous work that has accumulated over the years. Much of the information in the creep-rupture properties of nickel-base superalloys has been derived for high temperatures (> 900°C). The predominant application of these alloys in these temperatures is for turbine blades, the majority of which are typically produced by casting. With such differences in fabrication methods and use (test) temperatures, it is probably worthwhile to indicate some of the anticipated differences in behavior characteristics.

The size, amount, distribution, etc. of the hardening phase, γ', has been recognized as an important factor controlling creep-rupture properties at high temperatures. For example, coarsening of γ' particles during high temperature creep can lead to acceleration of creep rates and premature rupture(3, 4). The kinetics of the coarsening are governed by the nature of the γ/γ' interface; in particular, particles with low energy coherent interfaces would be expected to coarsen at slower rates compared with particles with semi-coherent interfaces. This expectation has been confirmed in several studies(3, 5), leading to the prescription for zero γ/γ' lattice misfit as an alloy design guideline for good creep-rupture resistance(3). However, in alloys for use at lower temperatures where γ' particle coarsening is relatively unimportant, this guideline may no longer be useful. Another design guideline advocated for good creep-rupture properties is to produce a large volume fraction of γ' phase (60%), in the form of small particles at small spacings(3). Presumably this condition results in an increased tendency for shearing of the γ' particles and hence the better creep resistance. In practice, this condition may be difficult to attain, especially in P/M superalloys with high volume fraction of γ' phase since, as will be shown later, two types of γ' particles and three particle size distributions are present. It might be considered that this guideline implies that the tensile yield stress is a good measure of creep resistance. Although this may hold for a single alloy after various heat treatments, we will show it does not explain the differences between the alloys evaluated in this study.

Grain size is another major factor which controls creep-rupture properties, as would be expected for failure occurring at grain boundaries. It is generally observed that increasing the grain size or elimination of grain boundaries, as in single crystal components, leads to enhanced stress-rupture life. In the case of the powder alloys studied, the grain sizes are determined predominantly by HIP-consolidation temperatures and are relatively independent of alloy compositions. The grain sizes resulting from HIP-consolidation below and above the γ' solvus are approximately 15μm and 45μm, respectively, much smaller sizes than found in cast products. However, grain size effect on stress-rupture properties have been shown to occur in P/M superalloys; material consolidated above the γ' solvus exhibits better rupture properties than the corresponding composition consolidated below the γ' solvus. On the other hand, as we shall show, the variation of rupture properties between different alloy compositions cannot be explained by the grain size effect.

There are, no doubt, many other differences that could be considered, such as alloy stability, defect population, and types, etc., but as such factors were shown to be unimportant in the present study, we shall not discuss them here.

2.2 EXPERIMENTAL

Preparation of Materials. The alloys AF115, modified MAR-M432 (B6) and MERL 76 used in the present study were vacuum induction melted and argon atomized. The -80 mesh powder fraction of each alloy was outgassed at 260°C and transfered to a stainless steel container. The evacuated powder container was sealed and then consolidated by hot isostatic pressing. Heat treatments of the consolidated materials were performed in a muffle furnace with temperature control of ± 10°C. The details of the HIP and heat treatment conditions are given in Table I.

Specimens and Creep-Rupture Testing. The dimensions of the creep-rupture specimens are given in Figure 1a. Tensile specimens were similar to the creep-rupture specimens. Creep-rupture testing was performed under constant loads at several temperatures; the majority of tests were performed at 704°C. Creep strains were continuously recorded from an extensometer fixed to the test specimens; the accuracy of the strain measurement was 0.01%. Selected creep-rupture tests were also interrupted at various creep strains for examination of dislocation structures using transmission electron microscopy techniques and for inspection of surface cracks using metallographic and fluorescent penetrant techniques. Because of the surface roughness associated with the machined surface and the oxidation which occurred during creep-rupture tests in air, a surface layer of about 12 μm was removed by polishing prior to metallographic studies. To permit examination of an undisturbed surface, several electropolished specimens of alloys B6 and MERL76 were also tested in a vacuum. The fluorescent penetrant inspection technique can reveal a surface crack on the machined surface; however, the resolution is relatively low, about 250 μm. The creep crack propagation rates for the three alloys were measured at 704°C using center-notched sheet specimens, shown in Figure 1b. Prior to the creep crack growth experiments, cracks were introduced at the ends of the center notch by an alternating stress of 15 - 150MPa at 20°C.

Microstructure and Phase Identification. The microstructure of the alloys were studied using standard metallographic techniques on both as-received and creep tested materials. More specialized techniques used are described below. The techniques used for the extraction of phases were similar to those described by Baris and Kriege(6). Briefly, for the extraction of the γ' phase, the γ phase was anodically dissolved from a sample of about 1 g in an electrolyte consisting of 1 weight percent ammonium sulphate, 1 weight percent citric acid, and 98 weight percent water using a current density of 200 ma per cm^2. The residue was then centrifuged, dried and weighed. For the extraction of minor phases, a sample of about 1 g was anodically dissolved in an electrolyte consisting of 10 volume percent hydrochloric acid in methanol in which 1 weight percent of tartaric acid was also added. After dissolution of the γ and γ' phases, the residue was removed by a millipore filter with 0.5 μm openings, dried and weighed.

For the extraction of minor phases, a sample of about 1 g was anodically dissolved in an electrolyte consisting of 10 volume percent hydrochloric acid in methanol in which 1 weight percent of tartaric acid was also added. After dissolution of the γ and γ' phases, the residue was removed by a millipore filter with 0.5 μm openings, dried and weighed.

X-ray diffraction techniques, using the Ni-filtered CuK_α radiation, were used to determine γ and γ' lattice parameters and to identify minor phases. The γ and γ' lattice parameters were measured from filings taken from the heat treated materials and from extracted γ' using a precision lattice parameter camera. To achieve separation of the γ and γ' reflections, the filings were annealed at 870°C for 8 hours. The {331} and {420} reflections were used for the measurements. The precision is considered to be within ± 0.00008A. Identification of the minor phases from the extracted residue was performed using a diffractometer.

Transmission Electron Microscopy. Thin foils for transmission electron microscopy were cut from the gage section, normal to the stress axis of the creep tested samples. Thinning was performed using a twin-jet electro-polisher. The polishing solution was a mixture of 150 ml methanol, 150 ml ethanol, 150 ml butyl alcohol and 6% of perchloric acid (~30 ml). The operating potential was 55 volts and the current was 10 ma/mm^2.

2.3 RESULTS

Alloy Characterization. The compositions of the alloys selected for this study are given in Table II. In general the alloy compositions are rather similar although the following differences may be noted. Alloys AF115 and the modified MAR-M432 (B6) have similar carbon contents which are higher than that of MERL 76. The base compositions of MERL 76 and AF115 are similar except that the latter has a higher Hf content and also contains 6% W, while MERL 76 does not contain this element. Alloy B6 does not contain Mo and is the only material with a (small) Ta addition.

The tensile properties of the heat treated alloys are listed in Table III, which shows that MERL 76 and B6 have similar yield and ultimate tensile strength; however, the former alloy is considerably more ductile than the latter one. AF115 has somewhat higher tensile strength but with a relatively low ductility, similar to that of B6.

Microstructures of these alloys after heat treatments are shown in Figure 2, and average grain diameters in AF115, B6 and MERL 76 are 12.7 μm, 9.0 μm and 21.0 μm, respectively. The primary γ' phase in these alloys is distributed both intergranularly and intragranularly, with the γ' particle size being larger at the grain boundaries. The finer secondary γ' particles, which are precipitated during cooling and subsequent aging, are not resolved in these photomicrographs but may be seen in electron micrographs shown below. The volume fractions of γ' phase present in the alloys were determined both by weight measurements before and after dissolution of the γ phase, and by image analysis on electron micrographs using a Quantimet system. The agreement between these two techniques was within 6% for MERL 76. However, for alloys AF115 and B6 no reliable results could be obtained from the gravimetric technique due to partial dissolution of the γ' phase. Therefore, the quantitative metallographic results are presented in Table IV and will be used in subsequent discussion. From Table IV it can be seen that the total γ' phase volume fractions in all three alloys are about the same. However, there are differences between these alloys in terms of γ' particle size and relative amounts of primary and secondary γ' phase. Alloy B6 has the smallest primary and secondary γ' particle sizes and the largest volume fraction of fine secondary γ' particles. The volume fractions of the primary and secondary γ' phase of MERL 76 are intermediate between those of alloys AF115 and B6; however, particle sizes are the largest. Since these three alloys were given similar heat treatments, the above differences can only be attributed to compositional effects.

Another significant microstructural difference between these alloys is in the morphology of the γ' particles. Alloys AF115 and MERL 76 have similar γ' particle morphologies, the intragranular γ' particles are cuboidal while those at the grain boundaries are angular. In contrast, both the primary and secondary γ' particles in alloy B6 are spherical. The difference in γ' particle morphologies as well as the differences in the γ' particle size between alloys AF115 and MERL 76 as a group and alloy B6 can be understood in terms of the misfit strain, ϵ_a, between the γ and γ' phases defined as

$$\epsilon_a = \frac{a_\gamma - a_{\gamma'}}{a_\gamma} \qquad (1)$$

where a_γ and $a_{\gamma'}$ are the lattice parameters of the γ and γ' phases, respectively. These parameters were determined by x-ray diffraction on annealed (870°C for 8 hours) filings and on extracted γ' phase. The latter determination is necessary since the γ' lattice parameters could not be obtained from the superlattice lines generated by the filings because of their low intensities. The measured parameters and the mismatch strains determined for the three alloys are shown in Table V, which shows that the lattice mismatch is the lowest in B6 and the highest in AF115. The lattice parameters of the γ' phase in the bulk alloys are expected to be different from those of the extracted γ' particles since the latter are in a relaxed state. However, Maniar and Bridge(7) have shown that the difference between the embedded and the extracted γ' lattice parameters are sufficiently small to afford some degree of confidence in the mismatch data generated from the extracted γ' phase. Therefore, the data in Table V should be meaningful at least in a relative sense.

It has been shown by continuum mechanics calculations that with increasing mismatch strain between the matrix and the precipitate, the particle shape changes from sphere to rod to plate so as to minimize the total energy(8). Further, it has been observed that spherical γ' precipitates were formed in certain nickel-base alloys when the lattice mismatch strains were less than 0.5%, while for a higher degree of lattice mismatch (0.5-1%), cuboidal γ' precipitates were produced(9). Therefore, the correlation of the spherical γ' particle morphology in alloy B6 with the lowest mismatch among the three alloys is no surprise. The smaller γ' particle sizes in alloy B6 can be associated with the particle coarsening process and the precipitation process, both of which are influenced by the mismatch strain. The driving force for particle growth, by Ostwald ripening during high temperature treatments, is the reduction of the surface energy of the particles. A smaller lattice mismatch also leads to more homogeneous and faster nucleation during cooling from solution treatment which account for the larger number of smaller secondary γ' particles in B6.

It is also interesting to note that the lattice parameters for the primary and secondary γ' in AF115 are different which implies a corresponding compositional variation. However, such a difference is not unique to AF115. MERL 76 exhibits a similar difference when the heat treatment is changed; for example, when the material is cooled by quenching in oil instead of air cooling following the solution treatment, the primary and secondary γ' lattice parameters are 3.5961A and 3.5981A, respectively.

The characteristics of the minor phases in the three alloys are given in Table VI, from which it can be seen that the carbide particles are primarily of the MC-type, and those in AF115 and MERL 76 are of similar composition. As can be expected from the carbon contents in these alloys, AF115 and B6 have higher carbide contents than MERL 76. The larger weight fraction of the residue extracted from B6 may be associated with the presence of a small amount of $M_{23}C_6$ carbide which was not detected in either AF115 or MERL 76.

Creep and Rupture Behavior. The shape of creep strain: time relationships for the alloys AF115, B6 and MERL 76 are similar. Typical creep curves are shown in Figure 3 and can be seen to consist of secondary and tertiary creep stages with little or no primary creep. The absence of extensive stage one or primary creep seems characteristic of powder metallurgy alloys in the 650°-750°C temperature range. If we define the creep strains and times as done in Figure 4, it is possible to describe the relative contributions of secondary and tertiary creep as shown in Figure 5.

For alloys AF115 and MERL 76, the ratios of the secondary creep strain, ϵ_R, and the secondary creep time, t_S, to the rupture life, t_R, increase with stress. At low stresses, the contribution of the secondary creep to the creep-rupture life is small. For example, in MERL 76, t_S is about 20 percent of the rupture life at 620 MPa; however, it increases to about 50 percent at 860 MPa. For B6, both ϵ_S/ϵ_R and t_S/t_R are less stress-sensitive. Further, t_S/t_R is greater than 0.5 except at the lowest stress (448 MPa).

In high temperature creep, it is customary to express the secondary creep rate by the phenomenological equation:

$$\dot{\epsilon}_S = A\,\sigma^n \exp\frac{-Q}{RT} \tag{2}$$

from which the stress exponent n and the apparent activation energy for creep Q can be determined experimentally using the following expressions:

$$n = \left(\frac{\partial \ln \dot{\epsilon}_S}{\partial \ln \sigma}\right)_T \tag{3}$$

$$Q = -R\left(\frac{\partial \ln \dot{\epsilon}_s}{\partial \ln 1/T}\right)_\sigma \tag{4}$$

Further, rupture life t_R can often be described by a simple power law,

$$t_R = M\sigma^{-p} \tag{5}$$

The stress dependence of the (secondary creep rate)$^{-1}$, secondary creep time, tertiary creep time and the rupture life for the three alloys are illustrated graphically in Figures 6, 7, and 8. It can be seen from these figures that within the limited stress ranges used, both ln ϵ_S and ln t_R are linearly related to σ although some deviation at low and high stresses may be noted. In these cases, as will be shown later, deviations are accompanied by changes in fracture mode. Another interesting feature in these figures is the slopes of the curves which are summarized in Table VII. The stress exponents n and p are equal for both AF115 and B6 with values of 15.8 and 7.4, respectively. The stress dependence of both the secondary creep time and tertiary creep time appear to be similar to the secondary creep rate in alloys AF115 and B6 and to the rupture time in the case of alloy MERL 76.

In addition to the above relationships, it is also interesting to compare the magnitudes of the secondary creep rates and the rupture lives for these three alloys from data shown collectively in Figures 9 and 10. The secondary creep rates of B6 are the highest, being two to three orders of magnitude higher than those of AF115, which exhibited the lowest creep rates. Correspondingly large differences in rupture lives can be observed in Figure 10. The rupture lives of B6 are about two orders of magnitude lower than those of AF115. The inverse relationship between the secondary creep rate and the rupture life, as originally observed by Monkman and Grant(10), also applies in the present case, i.e.,

$$t_R \, \dot{\epsilon}_S^{m} = \text{constant} \qquad (6)$$

The exponent m equals unity for alloys AF115 and B6 because of the similar stress dependence of the secondary creep rate and the rupture time. In the case of MERL 76, the exponent m is 3.4.

The temperature dependence of the secondary creep rates at constant applied stresses for alloys AF115, MERL 76 and B6 is shown in Figure 11. The apparent activation energies for creep as determined from the slopes of these plots are summarized in Table VII. It can be seen that the activation energy of B6 is appreciably smaller than those of AF115 and MERL 76. The latter alloys give activation energies which are considerably higher than those for self-diffusion in nickel and solid solutions of nickel (280 - 305 KJ mol^{-1})(11, 12), but are similar to values reported for other nickel-base superalloys(13).

Creep Deformation Processes. Transmission electron microscopy was used to gain insight into the mechanisms of creep deformation. Thin foils were prepared from stress-rupture specimens that had been tested to various creep strains or to failure. Figure 12 shows a micrograph of an AF115 specimen tested to a strain of 0.002 in which two types of structures can be observed. Stacking fault ribbons on two planes can be seen which lie in γ' phase. Such superlattice intrinsic faults, which have been seen in other superalloys(14), are bounded by 1/3 <112> partials. The second feature of the micrograph is the long, rather straight dislocation segments that lie in the matrix or the γ/γ' interface. The deformation substructure observed in B6 after fracture (strain $\sim$0.05) is remarkably similar, as shown in Figure 13. In contrast, at fracture both MERL 76 and AF115 show a profusion of microtwins as illustrated in Figure 14. These microtwins extend through both the γ and γ' phase and are thought to form by the spontaneous degeneration of the stacking fault layers when a sufficiently high density has accumulated(14).

The above observations show that the basic deformation modes are similar in all three alloys. Differences are seen in the rates of accumulation of defects, which occur far more rapidly in AF115 and MERL 76 than in B6.

Creep-Rupture Processes. Examination of the ruptured specimens indicated that all failures in the three alloys were initiated on the specimen surfaces. The appearance of a typical fracture is illustrated in Figure 15. The dominant crack formed on the surface at A and propagated across region B until fast (overload) cracking occurred in region C. (The demarcation between region B and C is caused by a change in oxide thickness in these regions). Numerous grain boundary cracks could be observed on specimen surfaces after fracture. Typically, these cracks encompass several grains on the surface (Figure 16a) but penetrate only a very short distance (one to two grains) beneath the surface (Figure 16b), suggesting an important role of environmental effects on crack nucleation and propagation. Lateral extension of these shallow cracks resulted in the formation of a dominant crack which propagated slowly into the material until a critical crack size was reached.

To ascertain the importance of crack nucleation life to the total life, selected creep-rupture tests at 704°C were interrupted at various creep stages and inspected for cracks. Alloy AF115 was studied after air testing. Cracking in B6 and MERL 76 was studied after tests in a vacuum of 2.5×10^{-4} Torr. For AF115, no cracks could be detected by the metallographic techniques during the secondary creep. However, since the metallographic techniques involved removal of a 12.5 μm deep surface layer, it is possible that surface cracks less than about 12.5 μm might have formed during the secondary creep. As metallographic inspection of electropolished specimens tested to the secondary creep stage in a vacuum also failed to reveal surface cracks in alloys B6 and MERL 76, we conclude surface cracks probably form during tertiary creep. Figure 17 shows the appearance of the surface of a MERL 76 specimen tested at 704°C under a stress of 655 MPa to a strain of 0.008 in the secondary creep stage. The fiducial marks, which are parallel to the tensile axis, were intended for grain boundary sliding measurements. As can be seen from this Figure, no microcrack could be observed. However, grain boundary sliding, as evidenced by the relief effect at grain boundaries is quite obvious*. The surface appearance of MERL 76 after testing to a strain of 0.04 in the tertiary creep stage, is shown in Figure 18 in which cracking at grain boundary triple junctions can clearly be seen. Coarse slip bands have also developed at this strain level. Attempts to detect internal microcracks on longitudinal sections of specimens tested to the secondary creep stage also failed to yield evidence of cavitation or microcracking. However, it should be realized that the limit of detectability for the scanning electron microscopy techniques used is about 0.2 μm. Thus, our observation does not exclude the possibility that cavities smaller than tbout 0.2 μm may be generated during secondary creep.

---

* Noticeable displacement of the fiducial markings due to grain boundary sliding is not expected because of the small amount of total strain (0.008) and the small grain size (21 μm).

The results of the crack inspection using a fluorescent penetrant technique, given in Table VIII, demonstrate that the formation of a detectable crack (~ 250 μm) constitutes a major portion of the rupture life in these alloys. The propagation of this crack to fracture consists of only a small fraction (~ 10%) of the rupture life. Similar observations have been made by Wilson in wrought Waspaloy(15).

Although the dominant crack always forms on the gage surface, rather uniformly distributed internal microcracks are also observed. These are illustrated in Figures 19, 20 and 21 for alloys AF115, B6 and MERL 76, respectively, tested with stresses where the secondary creep rates and rupture time exhibit linear stress dependence. The mechanisms of microcrack formation in AF115 and B6 appear to be similar. Cavities (indicated by arrows in Figures 19 and 20) nucleated at carbide particles in grain boundaries. Microcracks which formed by enlargement and linkage of these cavities propagated along the boundaries and joined with adjacent microcracks. In contrast, microcracks formed at triple junctions in MERL 76. As will be discussed later, this observation, together with the observed differences in stress dependence of secondary creep rate and rupture time, suggest that grain boundary sliding was responsible for formation of microcracks in this alloy. The similarity in distribution and appearance of the surface and internal microcracks suggests that the mechanism of formation of the dominant crack at the surface was the same as that which occurred internally. However, the former nucleated and propagated more rapidly, which could be due to smaller geometrical constraint of the surface grains and enviromental effects.

In Figures 6, 7 and 8 it may be noted that rupture times deviate from linearity at both low and high stresses. These deviations were accompanied by a change of creep-rupture processes. At low stresses (< 448 MPa for B6 and < 690 MPa for AF115) the rupture occurred by cavitation around carbide particles. These cavities are round and distributed uniformly throughout the material (Figure 22). At high stresses (> 760 MPa for B6 and ≥ 860 MPa for MERL 76) both B6 and MERL 76 failed with mixed transgranular and intergranular modes of fracture, as illustrated in Figure 23.

Creep-Rupture Ductility. The average fracture strain at 704°C for AF115, B6 and MERL 76 are 0.046, 0.052 and 0.114, respectively. The effect of stress on fracture strain, if any, is smaller than the scatter in data. We shall discuss below the factors that control the creep-rupture ductility in the first two alloys.

Creep Crack Growth (Rates). The creep crack propagation rates for alloys AF115, B6 and MERL 76 determined at 704°C, using center-notched and fatigue-precracked sheet specimens, are shown in Figure 24. One problem encountered in the measurement of creep crack growth, which has been noted by other investigators(16, 17) was that the crack growth rate was not uniform across the specimen thickness. The crack propagated faster at the center and at a slower rate near the surface. Therefore, the data presented in Figure 24 provide only lower estimates of the creep crack growth rates. We shall attempt to use these data in an explanation of the tertiary creep time in a subsequent section.

2.4 DISCUSSION

In the above sections various aspects of the creep-rupture behavior of the three nickel-base superalloys at intermediate temperatures have been presented in some detail. In this section an attempt is made to account for the differences in creep behavior and to give a semi-quantitative treatment of the overall fracture processes. The latter work tries to blend the microscopic nucleation behavior into the more macroscopic crack growth processes. We shall also attempt to point to some of the implications for alloy design that this study has revealed.

A common feature found in all three alloys is that creep-rupture life is inversely related to the secondary creep rate by the Monkman-Grant (M-G) type expression (Equation 6). The strain rate exponents m in the M-G relationship depends upon the fracture process. For alloys AF115 and B6 in which fracture occurs by nucleation of microcracks at grain boundary carbide particles and subsequent linking of these cracks, m equals unity. For alloy MERL 76, in which fracture is caused by formation of wedge-type cracks at grain boundary junctions, the rupture time has a significantly lower stress dependence than the secondary creep rate. In this case m equals 3.4. From the M-G relationship it is obvious that rupture life is dominated by the creep resistance (or secondary creep rate) which is discussed in the next section.

Creep Properties. The important material parameters which govern the creep resistance can be observed from the modulus-corrected expression for the secondary creep rate,

$$\dot{\epsilon}_s = B\left(\frac{\sigma}{E}\right)^n \exp\left(-Q/RT\right) \qquad (7)$$

In most pure metals the values of n are typically in the range of 4 - 6, and the apparent activation energy for creep is approximately equal to that for vacancy diffusion(18), which for Ni is about 276 KJ mol^{-1}(19). Alloying generally increases the creep resistance by increasing the value of n and/or the value of Q. Interestingly, two classes of highly creep-resistant alloys can be distinguished on the basis of these creep parameters. The first one is the particle strengthened solid solutions in which the creep resistance has been attributed solely to very large values of n, as high as 75(20); an example would be the ODS alloys. The second group, which includes the γ'-strengthened nickel-base superalloys, are characterized by unusually large Q values and moderately high n values, e.g. 720 KJ mol^{-1} and 8.5, respectively for IN100 at about 920°C and 300 MPa(4). In the present case where creep-rupture tests were conducted at lower temperatures and higher stresses, both larger values of n and Q have been obtained for MERL 76 and AF115. In contrast, both n and Q are low for B6.

The reasons for the significant difference in n and Q values between alloys AF115 and MERL 76 as a group and alloy B6 lie in the basic creep mechanisms in these alloys. However, some insight for this difference can also be obtained if the creep rate is described in terms of the effective stress,

$$\dot{\epsilon}_s = B'\left(\frac{\sigma-\sigma_i}{E}\right)^{n'} \exp\,(Q'/RT) \qquad (8)$$

where σ_i is the internal stress and Q' is the activation energy for creep under constant effective stress $(\sigma-\sigma_i)$. The values of n' and Q' determined for several nickel-base superalloys are much lower than n and Q, but approach those determined for nickel and its solid solutions(21). Further, Purushothaman and Tien have shown recently that if the internal stress can be assumed to be independent of the applied stress, then as σ_i/σ ratio approaches unity, n can be very large(22). Thus, both high values of n and Q for nickel-base superalloys can be attributed to the high internal stress developed during creep deformation. The significantly lower values of n and Q for alloy B6 are likely to be due to the presence of a lower internal stress during creep deformation. Since the internal stress results from the stress fields of dislocations and perhaps the γ/γ' lattice coherency strain also, one implication is that B6 should have a lower dislocation content compared with AF115 and MERL 76. This is the major conclusion from the transmission electron microscopy. It is also possible that the lower values of n and Q in B6 are due to a different creep mechanism in this alloy, but this is considered unlikely since the deformation structures of the three alloys are essentially the same during secondary creep. Therefore, the main difference between AF115 and MERL 76 as a group and B6 may be traced to the faster recovery rate in the latter alloy.

The specific recovery processes in these alloys are not clear, but since the creep tests were conducted at temperatures about 0.6 T_M, climb of dislocations along the γ/γ' interface may be an important recovery mechanism(23). In this case the nature of the γ/γ' interface should affect the rate of recovery. The nature of the γ/γ' interface is governed by the lattice misfit between the γ and γ' phases and by the size of the γ' particles. For γ' particles less than 1 μm, as in our case, the lattice misfit is accommodated by an elastic coherency strain field around the γ' particles. (For larger γ' particles, the lattice misfit is accommodated by interfacial dislocations(24, 25). Therefore, in the present case, the interaction of dislocations with the coherency strain field probably governs the recovery process. This interaction is repulsive, the magnitude of which depend directly on the misfit strain(26). Therefore, one would expect a higher recovery rate and lower creep resistance in a material with lower lattice misfit, a postulate consistent with our observations. Conversely, to produce alloys with superior creep capability at intermediate temperatures, relatively high mismatch between the γ' and the matrix is required.

It should be noted that this conclusion is opposite to that of Davis and Johnson(3), Mirkin and Kancheev(5), and Maniar and Bridge(7), but is consistent with that of Gibbons and Hopkins(27). Differences in alloy chemistry, test conditions, etc. may account for some of these differences. Further, it may be noted that many advanced alloys to be used in the temperature range 590°C-760°C are derived from cast alloys intended for use above 870°C. There is no doubt that at such higher temperatures structural stability and coarsening characteristics of the phases are of much greater importance.

Creep-Rupture Processes in AF115 and B6. Creep-rupture processes in both alloys depend upon the applied stress. At low stresses (below half the yield strength), failure occurred by a cavitation process, which involved formation and growth of cavities around carbide particles. These cavities are round (r-type) and distributed uniformly throughout the material (Figure 22). Failure occurred by linkage of these cavities, probably after a critical volume of cavities had been produced, as shown for Nimonic 80A(28). At intermediate stresses, cavities are again nucleated on carbide particle surfaces. However, these cavities are more crack-like and propagated along grain boundaries normal to the stress axis (Figures 19 and 20). Impingement of these "planar" carbide-centered cavities resulted in microcracks on grain boundaries. More microcracks are formed on the surface than in the interior(Figure 16), suggesting an important role of the test environment. Linkage of microcracks on the surface produced a dominant crack which propagated intergranularly until rapid transgranular (tensile) mode of failure occurred (Figure 15). At high stresses, (near the yield strength of the material) cavities formed at grain boundaries and inside the grains. Failure in this case occurred by propagation of a surface-nucleated crack along an intergranular/transgranular path (Figure 23).

In the following, a semi-quantitative description of the creep-rupture processes at intermediate stresses in alloys AF115 and B6 will be developed. Some of the evidence cited is indirect since most of our observations were made at the interior of specimens while all fractures started on the surface. However, it is reasonable to assume that the creep-rupture processes on the surface are the same as those in the interior except that they occur at faster rates in the former case because of the environmental effects. No cavities or microcracks were detected in longitudinal sections of specimens during the secondary creep stage, which could mean either that nucleation of cavities occurs at the onset of tertiary creep or that cavities are simply too small to be detected. Using high precision density measurements, it has been shown that cavity nucleation begins at the inception of creep deformation in pure metals, however, such cavities are not resolvable by optical microscopy(29-32). It has also been observed that the creep rupture life of copper containing a dispersion of silica particles is determined by the growth of the particle-nucleated cavities at the grain boundaries rather than the nucleation of cavities(33). Therefore, we shall assume that the small cavities nucleate during the initial stage of creep deformation in our alloys. These cavities grow during the secondary creep stage. Following Davis and Williams(34), it is further proposed that the onset of tertiary creep occurs when the cavities become thermodynamically stable. The minimum radius, r_S, of a thermodynamically stable cavity is given by

$$r_S = \frac{2\Gamma}{\sigma} \qquad (9)$$

where Γ is the surface energy and σ is the tensile stress across the boundary containing the cavity. To estimate the thermodynamically stable cavity size in our case, put $\Gamma = 2\mathrm{Nm/m^2}$, the value for pure nickel at 950°C(35) and $\sigma = 550$ MPa. The diameter of the stable cavity is calculated to be 0.015 μm which is below the limit of detectability in our experiments. Therefore, the fact that no voids could be detected in specimens tested in secondary creep in the present study may not mean that cavities were not nucleated. Enlargement and linkage of these thermodynamically stable grain boundary cavities on a particle surface results in a "planar" cavity which propagates along the grain boundary until it merges with an adjacent cavity to form a microcrack (Figure 25). The latter is the dominant process in the specimen interior during tertiary creep. Creep-rupture processes occur at faster rates on the specimen surface than in the interior. However, because of the experimental difficulties encountered in detailed surface examination, the relationship between the creep-rupture processes: microcrack formation and the coalescence of microcracks to form dominant crack, and the creep stages have not been clearly identified. Proposed sequence of events for creep-rupture of a specimen is illustrated in Figure 26.

If the transition from secondary creep to tertiary creep is marked by cavities reaching a certain size, then one can estimate the secondary creep time, t_S from the kinetics of the cavity growth. The high stress dependence of the secondary creep time (Figures 6 and 8) suggests that the cavity growth is plastic strain controlled, rather than diffusion controlled. Using equation (9) to define the critical cavity size and the Raj modification of the Nagpal et al. equation for hole growth(37), one obtains, after integration and the necessary substitution,

$$t_S \geq \frac{4\Gamma}{1.48\, l_o\, \sigma^{n+1}\, A \exp(-Q/RT)} \qquad (10)$$

where l_o is the cavity spacing. Since cavities nucleate on carbides, values of l_o range from a fraction (say, 0.2) of the carbide diameter to the carbide spacing. A and n are defined in equation (1). Using a value of $2\mathrm{Nm/m^2}$ as surface energy for both AF115 and B6 and the experimentally determined values of l_o, A, Q, and n:

	AF115	B6
lo (μm)	0.1 to 1.5	0.1 to 2.1
Aexp-Q/RT*	5.7×10^{-51}	3.95×10^{-24}
n	16.0	7.0

*$\dot{\epsilon}_S$ in h^{-1}, σ in $\mathrm{MN/m^2}$

values for t_S can be calculated. A comparison of the observed secondary creep times and the calculated values (shaded bands) for the alloys AF115 and B6 is shown in Figure 27 and the agreement is surprisingly good.

This calculation could be extended to the linkage of cavities between particles in the manner envisaged by Raj(36). If such a process occurred uniformly throughout a specimen, this would lead to specimen failure by a general degradation process. As the rupture time (t_R) is inversely proportional to the stress with an exponent n (See Figures 6 and 8), it is clear that the solution would have the correct form. However, the experimental evidence points to different processes occurring during tertiary creep, viz.,formation of a dominant crack on the surface by linkage of shallow microcracks and propagation of this crack. The predominant role of surface cracking indicates a strong influence of the environment on the cracking process. Limited vacuum testing on the B6 alloy confirmed this, in that rupture lives were increased by an order of magnitude. In the present study, specimens with machined surfaces were used; these rather rough surfaces, coupled with the oxidation during the test, made the resolution of the early stages of crack formation very difficult. The smallest crack which could be reliably detected by visual inspection was ~250 μm. If the propagation of the surface nucleated crack can be assumed to be the dominant process during the tertiary creep, the tertiary creep time, t_T, may be estimated from the crack growth data*. The crack growth data for AF115 and MERL 76 exhibit two stages (Figure 28). At low stress intensities (stage I) the crack growth rates are highly sensitive to the stress intensity. For AF115, the slope of the stage I crack growth is about 20, which is close to the stress exponent observed for the secondary creep. At higher stress intensities (stage II) the crack growth rates are less sensitive to the stress intensity. The slopes of the stage II crack growth range from 1 to 5 for the three alloys. Similar curves for nickel-base alloys have also been reported by Sadananda and Shahinian(17). Since the major portion of the crack propagation life is expected to be spent in the stage I crack growth, it is obvious that the calculated crack propagation lives would have similar stress dependence as that observed for the tertiary creep times (Figures 6 and 8). To determine the magnitude of the crack propagation lives for the AF115 used for the creep-rupture studies (hot isostatically pressed below the γ' solvus, grain size 12.7 μm), the crack propagation rates can be reasonably assumed to be between those of MERL 76 and the coarser grain AF115, as shown by the dashed lines in Figure 28. Using the approximate crack growth behavior, the crack propagation life was calculated assuming a semi-circular crack with various initial crack lengths less that 250 μm (the first visually detectable crack). The calculated crack propagation lives were found to be much longer than the observed tertiary creep times. If the stage I curve is shifted to a lower stress intensity, as shown by the dotted line in Figure 28, good agreement between the calculated propagation lives and the observed tertiary times was obtained when the initial crack radius was assumed to be about 70 μm (Figure 29 Likewise, good agreement between the calculated creep crack propagation lives and the observed tertiary creep time has also been obtained for alloy B6 using a similar initial crack size. The assumed initial crack sizes are consistent with those observed on the specimen surface (Figure 16a). However, one may question the validity of moving the stage I crack growth curves to lower stress intensities. Limited work reported in the literature indicates that the threshold level for crack propagation (stage I) depends upon specimen thickness and magnitude of applied stress. A crack in a thin specimen, as in our center-notched sheet specimen, has a larger threshold value than in a thick specimen(17). Likewise, self-nucleated cracks in stress-rupture specimens also propagate at stress intensities well below the apparent threshold in AF115. Thus, we consider that for high stress situations the stage II curve could well be displaced to lower values.

---

* In the following discussion, we have chosen to use linear elastic fracture mechanics methods to express the stress dependence of cracking. The applicability of this approach is still somewhat controversial.

In summary, the (tertiary) rupture process consists of formation of a dominant surface crack and the propagation to failure, but one should not conclude that life could be increased by reducing the crack growth rate alone. Such a conclusion is valid only when the rupture life is dominated by crack growth, e.g. when a specimen contains a large pre-existing flaw. To improve the creep-rupture life, one should increase the creep resistance (decrease the secondary creep rate) as indicated by the M-G relationship. On the other had, if creep crack growth occurs by the accumulation of creep damage at the crack tip(16), then such increases could improve growth characteristics as well. This could be implied in the present work as the growth rates of the three alloys fall in the same order as creep capability, but the mechanistic similarities are obscure.

Creep-Rupture Ductility of AF115 and B6. The rupture ductility consists of strain contributions from the interior of grains and from localized regions surrounding the grain boundaries (ϵ_b) where cavitation occurs. A lower bound of ductility, ϵ_{1b} can be expressed as

$$\epsilon_{1b} = \frac{\lambda}{d}\,\epsilon_b \qquad (11)$$

where λ is the spacing of cavity and d is the grain diameter. Using the calculation of growth of a row of holes in a localized deformation band in a nonhardening material for estimating ϵ_b to coalesce the cavities, Pavinich and Raj(33) have shown that

$$\epsilon_{1b} = 0.23\,\frac{\lambda}{d} \qquad (12)$$

when $0.1 \leq w/\lambda \leq 0.5$, where w is the diameter of particles at grain boundaries. Using this expression and equating the cavity spacing to carbide particle spacing, the rupture ductility for B6 ($\lambda = 2.1\ \mu$m, d = 9.0 μm) and AF115 ($\lambda = 1.5\ \mu$m and d = 12.7 μm) is calculated to be 5% and

2.8%, respectively. The observed values are 5.5% and 4.6% respectively, which agree rather well with the lower bound ductility. Equation (12) suggests that the ductility of both AF115 and B6 can be increased by increasing the spacing of carbide particles which can be achieved by reducing the carbon content.

Creep-Rupture Processes in MERL 76. It was shown that creep-rupture in MERL 76 was caused by cracking at grain boundary triple junctions. Further, there is a significant difference between the stress dependence of the secondary creep rate and the rupture time which implies that the secondary creep deformation process does not contribute directly to the rupture process. Both of these observations suggest that grain boundary sliding is the major fracture mechanism in MERL 76, since it generally results in lower stress dependence than matrix deformation. The stress exponents of matrix deformation and grain boundary sliding for pure metals are typically in the range of 4-6(18) and 2-3(37), respectively. Note, however, that the magnitude of stress exponents alone cannot be used as a guide to the process occurring; the values for B6 and MERL 76 do not differ markedly although the rupture modes do.

2.5 CONCLUSIONS

The major conclusions are as follows:

1. For the materials studied, the creep-rupture lives are inversely related to the secondary creep rates, although the duration of the secondary creep stage may constitute a small fraction of the rupture life.

2. The marked difference in creep resistance between AF115 and B6 is due to the faster recovery rates in the latter alloy. Low γ/γ' lattice mismatch appears to be responsible for the difference. This suggests that increasing the mismatch may be an effective means of improving creep-rupture properties for the temperature range 650°C-760°C. Structural stability would set the useful limit of such an approach.

3. The mode of fracture initiation is governed by the carbon content. Materials with high carbon levels nucleate cavities at carbide particles; in low carbon alloys, cracks form by grain boundary sliding. Higher rupture ductility is associated with alloys with a lower carbon content. These results suggest that the carbon content should be balanced for any alloy to give the best rupture characteristics. For example, a lower carbon level in AF115 may lead to improved properties.

REFERENCES

1. M. J. Blackburn and R. A. Sprague: Metal Technology, 1977, Vol. 4, pp. 388-395.

2. "Advanced Fabrication Techniques in Powder Metallurgy and Their Economic Implications" Proceeding of the 42nd Panel Meetings AGARD, Neuilly sur Seine, 1976.

3. R. G. Davies and T. L. Johnston in "Ordered Alloys" Ed. B. H. Kear, C. T. Sims, N. S. Stoloff and J. H. Westbrook, p. 460, Claitor's Publishing Division, Baton Rouge 1970.

4. J. P. Dennison, P. D. Holmes and B. Wilshire: Materials Sci. and Engrg., 1978, Vol. 33, pp. 35-47.

5. I. L. Mirkin and O. D. Kancheev: Met. Sciences and Heat Treatment, 1967, No. 1 and 2, p. 10.

6. O. H. Kriege and J. M. Baris: Trans. ASTM, 1969, Vol. 62, p. 195.

7. G. N. Maniar and J. E. Bridge, Jr.: Met. Trans., 1971, Vol. 2, p. 95.

8. F. R. N. Nabarro: Proc. Roy. Soc., 1940, Vol. 175A, p. 519.

9. W. C. Hagel and H. J. Beattie, Jr. in "Precipitation Processes in Steels", pp. 98-107, Iron and Steel Institute Special Report No. 64, London, 1959.

10. F. C. Monkman and N. J. Grant: Proc. ASTM, 1956, Vol. 56, p. 834.

11. D. Sidey and B. Wilshire: Metal Sci. J., 1969, Vol. 3, p. 56.

12. K. Monma, H. Suto and H. Oikawa: J. Japan Inst. Metals, 1964, Vol. 28, p. 253.

13. G. R. Leverant and B. H. Kear: Met. Trans., 1970, Vol. 1, pp. 491-498.

14. J. M. Oblak and B. H. Kear in "Electron Microscopy and Structure of Materials" Ed. G. Thomas, University of California Press, Berkeley, 1972.

15. D. J. Wilson: J. Basic, Engr., 1972, Vol. 94, p. 13.

16. S. Floreen: Met. Trans. A, 1975, Vol. 6A, p. 1741.

17. K. Sadanada and P. Shahinian: Met. Trans. A, 1977, Vol. 8A, p. 439.

18. O. D. Sherby and P. M. Burke: Progress. Mat. Sci., 1967, Vol. 13, p. 325.

19. C. L. Meyer and O. D. Sherby: J. Inst. Metals, 1961-1962, Vol. 90, p. 380.

20. R. W. Lund and W. D. Nix: Acta Met., 1976, Vol. 24, p. 469.

21. K. R. Williams and B. Wilshire: Metal Sci. J., 1973, Vol. 7, p. 176.

22. S. Purushothaman and J. K. Tien: Acta Met., 1978, Vol. 26, pp. 519-528.

23. C. Carry and J. L. Strudel: Acta Met., 1978, Vol. 26, pp. 859-870.

24. G. C. Weatherly and R. B. Nicholson: Phil Mag., 1966, Vol. 7, p. 801.

25. A. Lasalimonie and J. L. Strudel: Phil.Mag., 1975, Vol. 32, p. 935.

26. V. Gerold and H. Haberkorn: Phys. Stat. Sol., 1966, Vol. 16, pp. 675-684.

27. T. B. Gibbons and B. E. Hopkins: Metal Science J., 1971, Vol. 5, p. 233.

28. B. F. Dyson and D. McLean: Metal Science J., 1972, Vol. 6, pp. 220-223.

29. R. C. Boethner and W. D. Robertson: Trans. Met. Soe. AIME, 1961, Vol. 221, p. 613.

30. R. T. Ratcliffe and G. W. Greenwood: Phil. Mag., 1965, Vol. 12, p. 59.

31. R. T. Ratcliffe: Brit. J. Appl. Phys., 1965, Vol. 16, p. 1193.

32. P. E. Brookes, N. Kirby and W. T. Burke: J. Inst. Met., 1959-1960, Vol. 88, p. 500.

33. W. Pavinich and R. Raj: Met. Trans. A, 1977, Vol. 8A, p. 1917.

34. P. W. Davies and K. R. Williams: Phil. Mag., 1968, Vol. 18, p. 137.

35. J. M. Blakely and P. S. Maiya, "Surface and Interfaces", Eds. J.J. Burke, N. L. Reed and V. Weiss', p. 325, Syracuse Univ. Press, 1967.

36. R. Raj, "Intergranular Fracture in Bicrystals" Cornell University Report No. 2842, April 1977.

37. R. N. Stevens: Met. Rev., 1966, Vol. 11, p. 129.

TABLE I

HOT ISOSTATIC PRESSING (HIP) AND HEAT TREATMENT CONDITIONS

Alloy	γ' Solvus, °C	HIP, °C/MPa/Hr	HT, °C/Hr/Cooling Method
AF115	1191	1157/100/3	1174/2/AC + 760/8/AC
Ta-Hf-Modified Mar-M432(B6)	1141	1107/100/3	1116/2/AC + 760/8/AC
MERL 76	1188	1177/100/3	1121/2/AC + 760/8/AC

AC: Air-cooled

TABLE II

ALLOY COMPOSITIONS (WEIGHT %)

	MERL 76	AF115	Ta-Hf-Modified Mar-M432 (B6)
Ni	Bal.	Bal.	Bal.
Cr	12.3	10.5	15.4
Co	17.9	15.0	19.6
V	--	--	--
Ta	--	--	0.7
Mo	3.3	2.8	--
W	--	6.0	2.9
Al	5.0	3.9	3.1
Ti	4.3	3.9	3.5
Nb	1.7	1.8	1.9
Hf	0.74	2.1	0.7
B	0.018	0.020	0.021
Zr	0.06	0.05	0.06
C	0.025	0.15	0.14
O	94 ppm	88 ppm	90 ppm
N	30 ppm	34 ppm	10 ppm

TABLE III

704°C TENSILE PROPERTIES

Alloy	0.2% Yield Strength	Ultimate Strength (MPa)	Elongation (%)	Reductio in Area (%)
AF115	1066[a]	1331	8.5	10.9
B6	992	1261	8.1	13.5
MERL 76	983	1247	29.3	40.1

[a] Intrapolated values.

TABLE IV

γ' PARTICLE SIZES AND VOLUME FRACTIONS

Alloy	Primary γ'			Secondary γ'		Total γ' Volume Fraction
	Particle Size, μm		Volume Fraction	Particle Size, μm	Volume Fraction	
	Intergranular	Intragranular				
AF115	0.76-3.30	0.13-0.51	0.30	0.01-0.06	0.39	0.69
B6	0.25-1.50	0.05-0.20	0.15	0.01-0.03	0.53	0.68
MERL 76	3.81-7.62	0.51-2.54	0.20	0.05-0.25	0.47	0.67

TABLE V

LATTICE PARAMETERS OF γ AND γ', AND MISMATCH

Alloy	γ, Annealed Filings Å	γ', Extracted Phase Å	Mismatch Strain, %
AF115	3.5883	Primary 3.6003 Secondary 3.5956	-0.34 -0.20
36	3.5900	3.5931	-0.087
MERL 76	3.5893	3.5951	-0.16

Precision: ±0.00008Å

TABLE VI

MINOR PHASES: TYPES, LATTICE PARAMETERS, AMOUNTS AND SIZES

Alloy	Minor Phases					Total Weight % Extracted
	Type	Quantitative Estimate	Major Element (Descending Order)	Particle Size, μm	Lattice Parameter Å	
AF115	MC MC	Major Trace	Hf, Nb, Ti —	0.65 —	4.518 4.330	1.08
B6	MC $M_{23}C_6$	Major Trace	Ta, Nb, Ti —	0.56 —	4.420 —	1.28
MERL 76	MC	Major	Hf, Nb, Ti	0.20	4.424	<0.69*

*Weight percent includes a small amount of γ phase.

TABLE VII

STRESS EXPONENTS AND ACTIVATION ENERGIES FOR CREEP AND RUPTURE

Alloys	n	p	Q KJ mol^{-1}
MERL 76	15	5	520
AF115	16	16	700
B6	7	7	370

TABLE VIII

NUCLEATION OF A DOMINANT CRACK IN CREEP RUPTURE AT 704°C

Alloy	HIP & HT Conditions[a]	Stress (MPa)	Crack Inspection Results	Fracture Life (Hr.)
AF115	L and 2	760	NI[b] at 814 Hr.	849
AF115	L and 3	760	NI at 372 Hr.	409
AF115	H and 3	760	~0.3mm crack at 519 Hr.	590
B6	B	690	~0.3mm crack at 95 Hr.	101
B6	B	690	NI at 42 Hr.	54

[a] L = HIP: 1135°C/100 MPa/3 Hr.
H = HIP: 1205°C/100 MPa/3 Hr.
2 = HT: 1174°C/2 Hr/AC + 760°C/8 Hr/AC
3 = HT: 1174°C/2 Hr/AC + 982°C/8 Hr/AC + 760°C/8 Hr/AC
B = HIP: 1190°C/100 MPa/3 Hr., HT: 1130°C/2 Hr/AC + 982°C/8 Hr/AC + 760°C/8 Hr/AC

[b] NI = No crack indication

[c] Tested in vacuum 2.5×10^{-4} torr

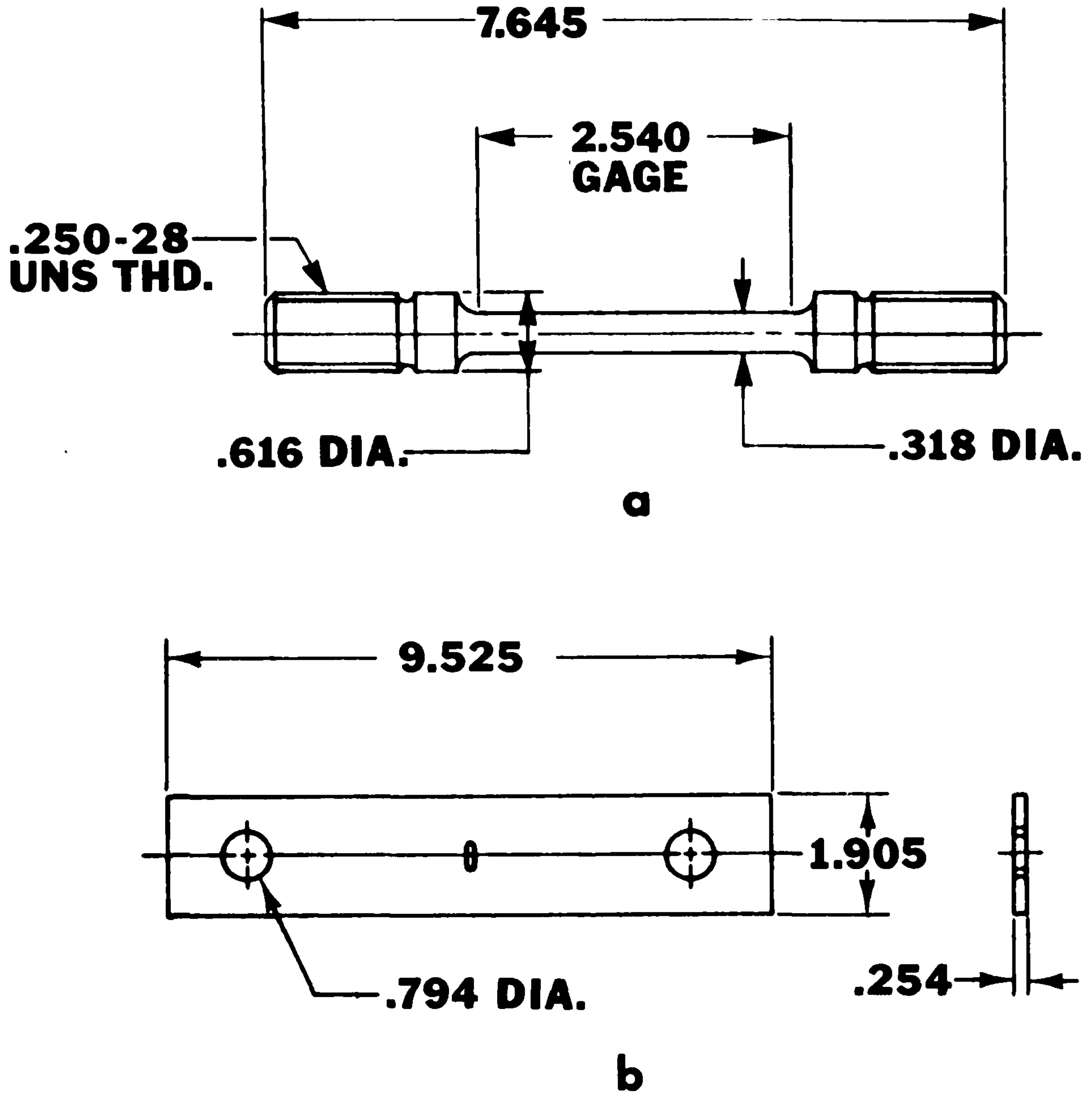
7.645
2.540
GAGE
.250-28
UNS THD.
.616 DIA.
.318 DIA.
a
9.525
1.905
.794 DIA.
.254
b

Figure 1 Dimensions of (a) creep-rupture specimen
(b) creep crack propagation specimen, in cm.

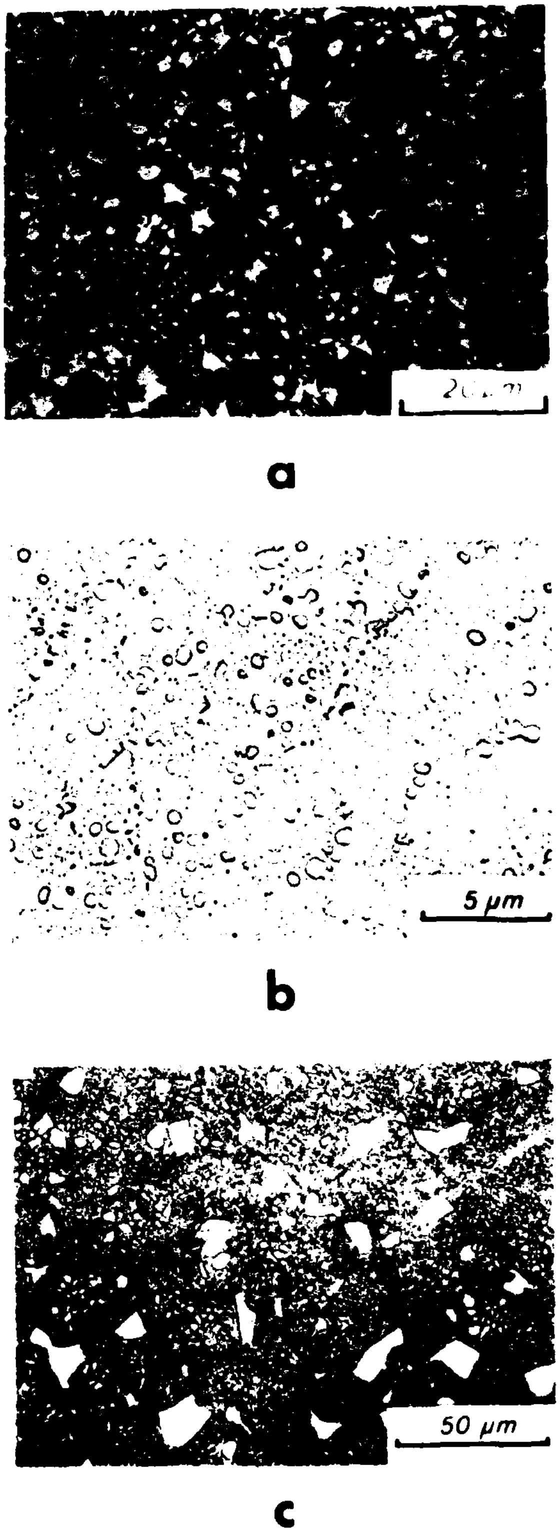

Figure 2 Microstructures of alloys (a) AF115 (b) B6 (c) MERL 76. Note the differences in size and morphology of the γ' particles between either AF115 or MERL 76 and B6. The consolidation and heat treatment conditions of these alloys are given in Table I.

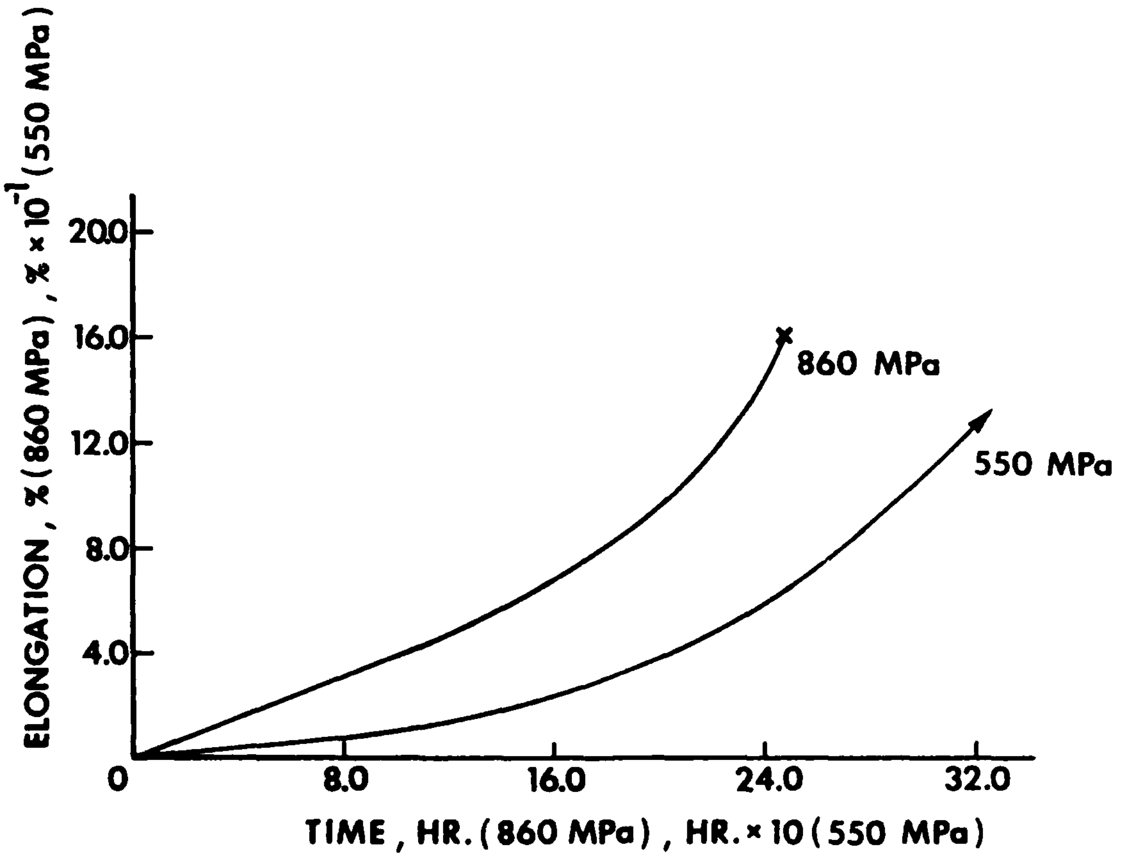

Figure 3 Typical shape of creep curves. MERL 76 at 704°C.

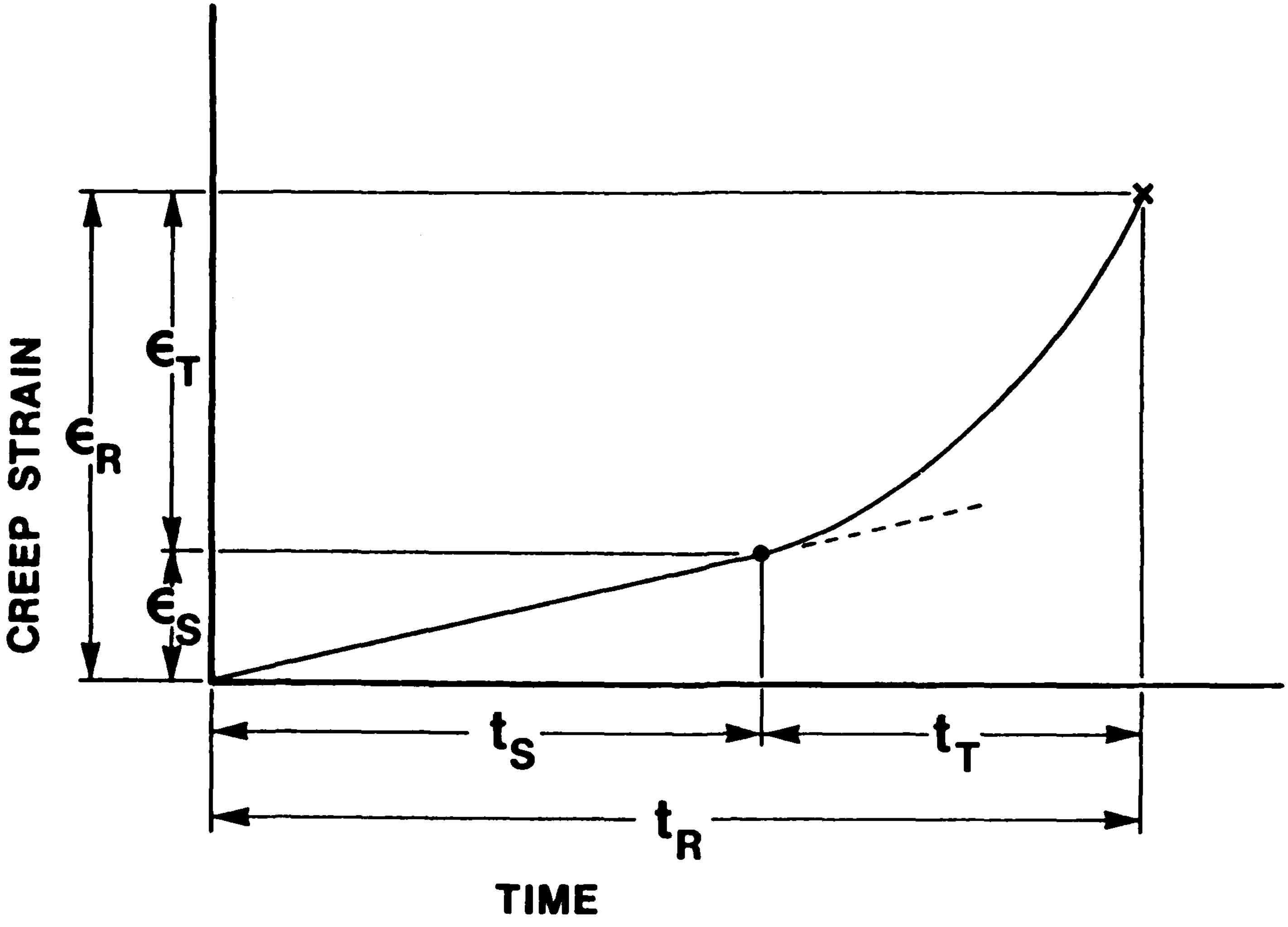
CREEP STRAIN
ϵ_R
ϵ_T
ϵ_S
t_S
t_T
t_R
TIME

Figure 4 Schematic illustrating the nomenclatures used to describe the creep curve. e_S and e_T are the secondary and tertiary creep strains, t_S and t_T are the secondary and tertiary creep times, e_R and t_R are the creep-rupture strain and time, respectively.

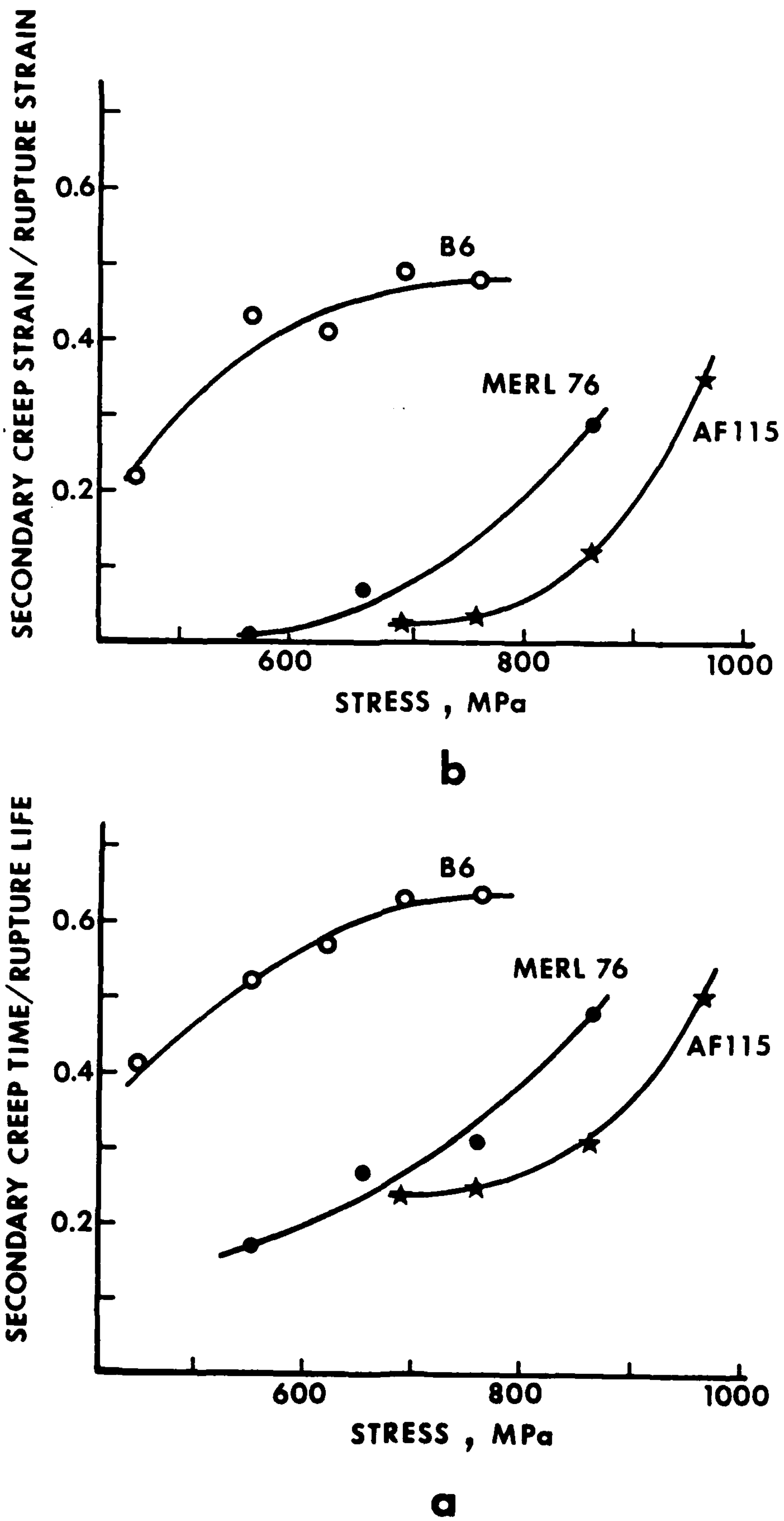

Figure 5 Ratios of secondary creep time to creep-rupture life (a) and secondary creep strain to creep-rupture strain (b) for alloys AF115, modified Mar-M432 (B6) and MERL 76, all at 704°C.

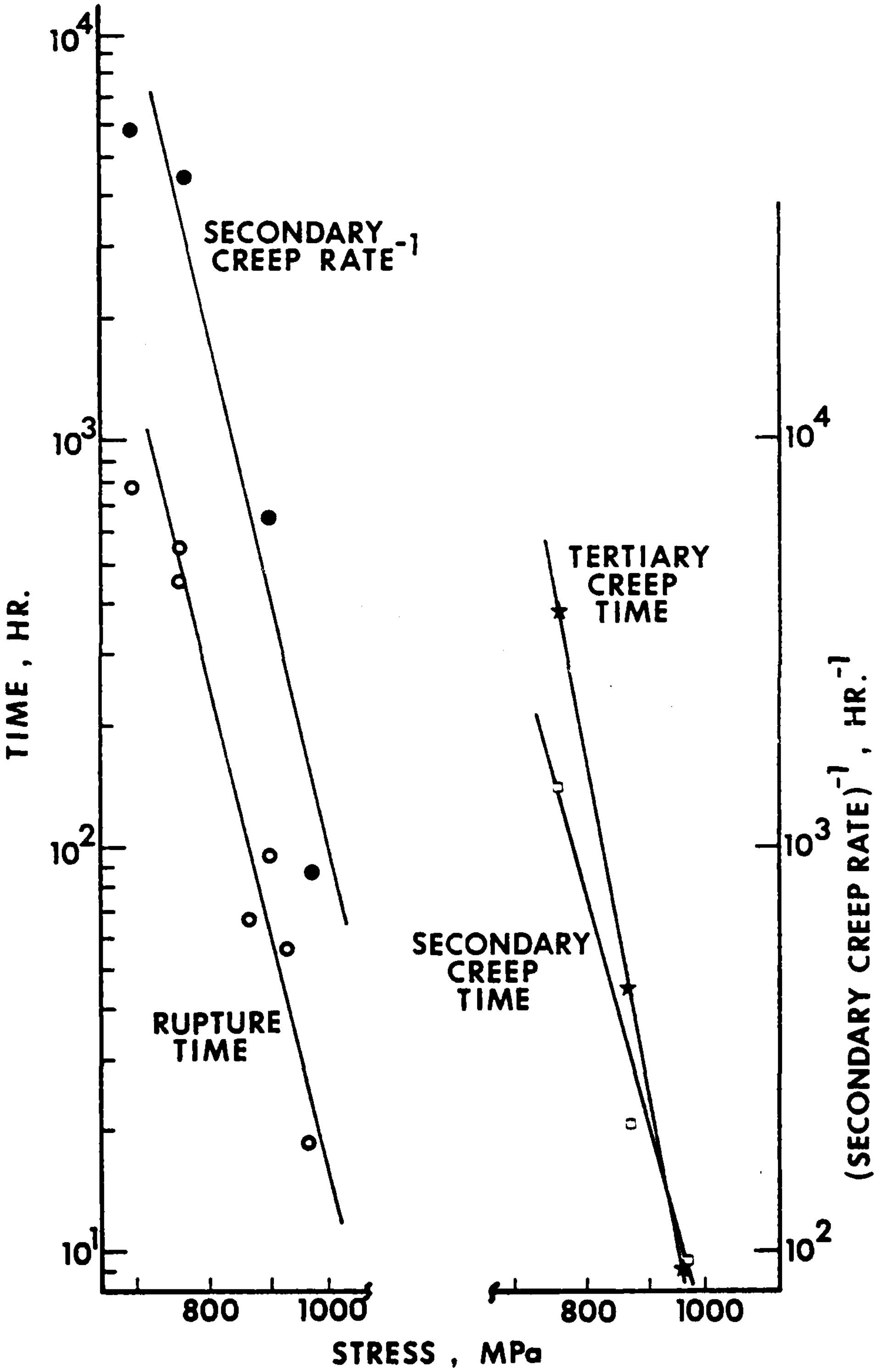

Figure 6 Creep-rupture life, secondary creep rate, secondary creep time and tertiary creep time versus stress for AF115 at 704°C.

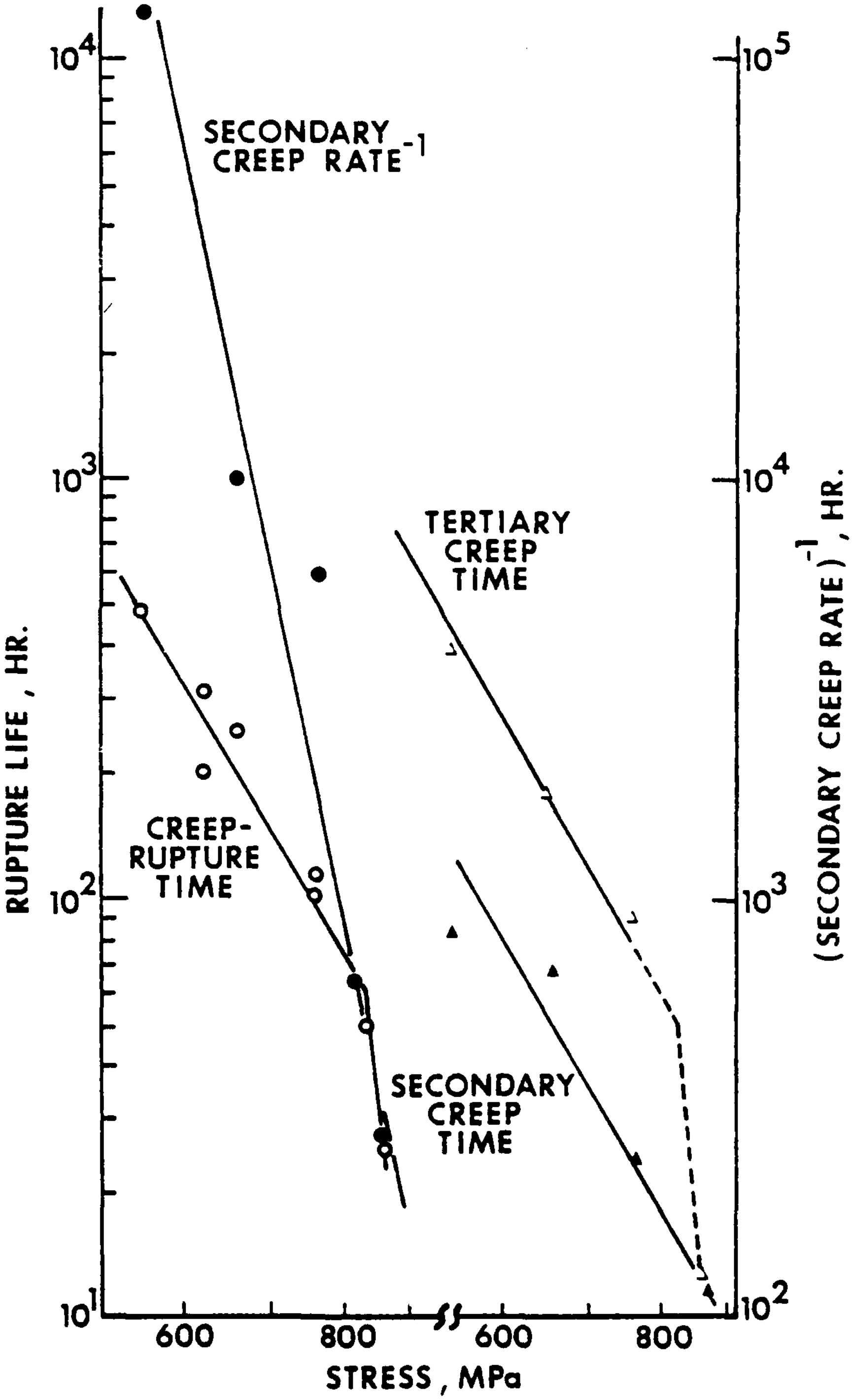

Figure 7 Creep-rupture life, secondary creep rate, secondary creep time and tertiary creep time versus stress of MERL 76 at 704°C.

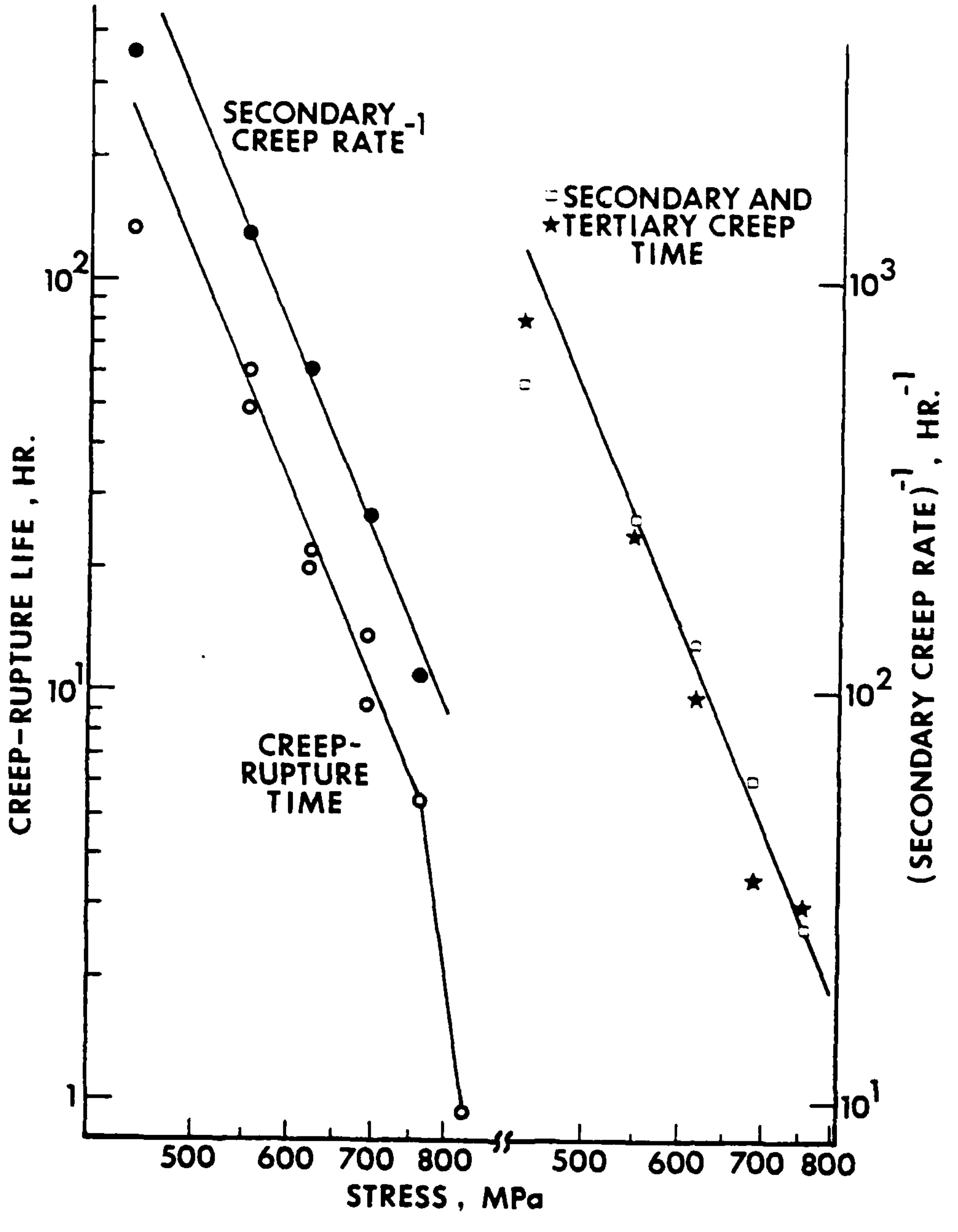

Figure 8 Creep-rupture life, secondary creep rate, secondary creep time and tertiary creep time versus stress for modified Mar-M432 (B6) at 704°C.

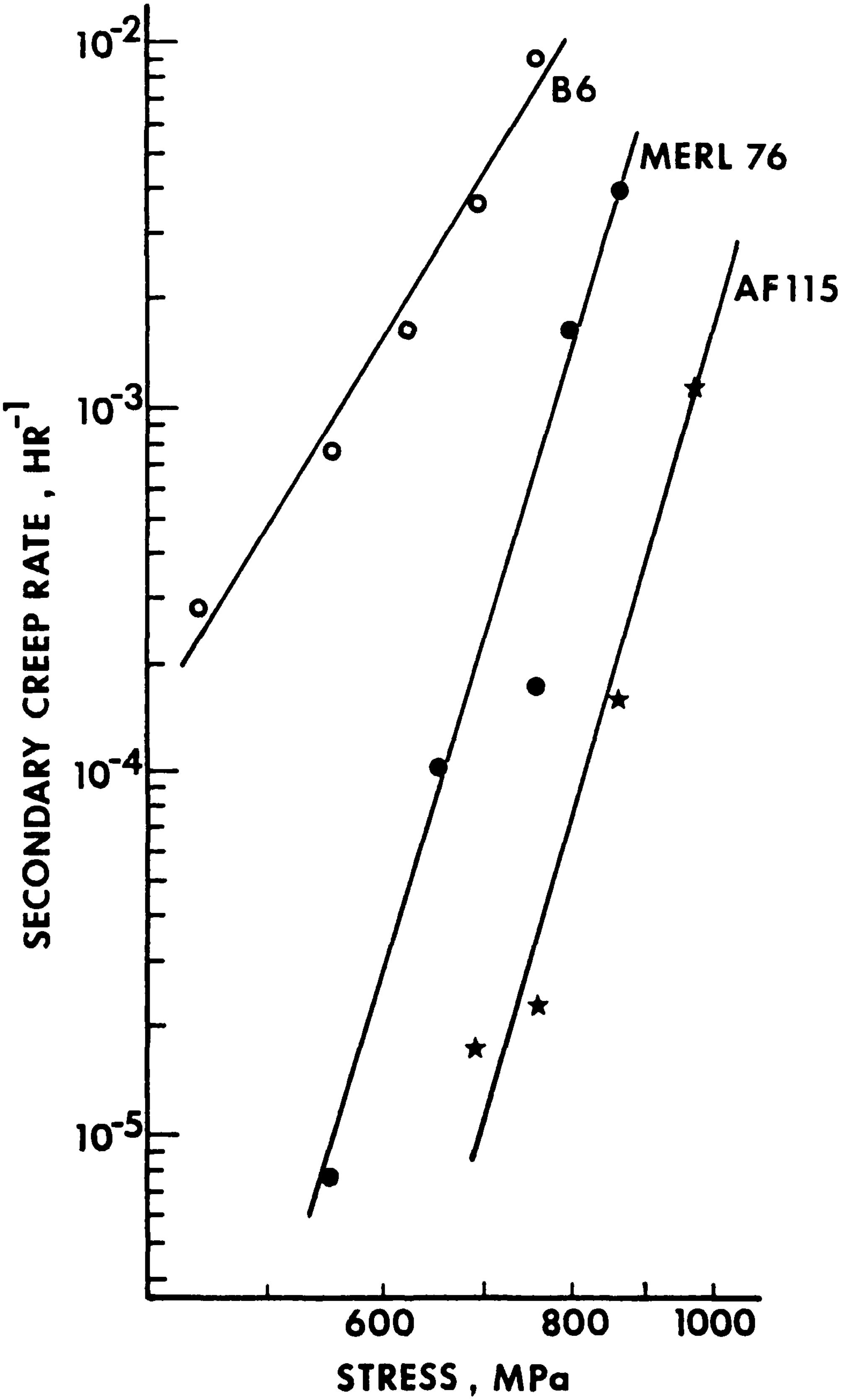

Figure 9 Secondary creep rate versus stress at 704°C.

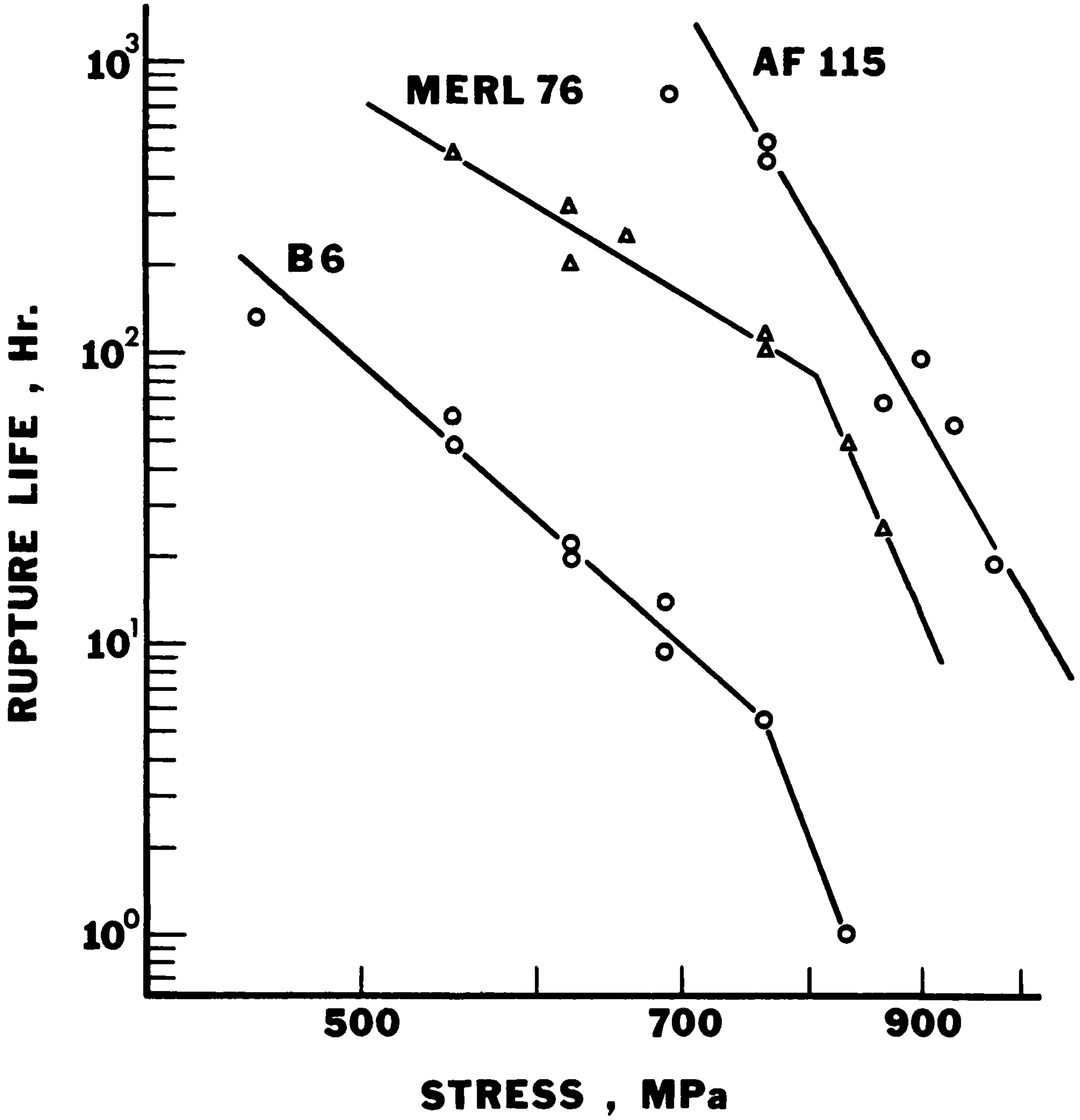

Figure 10 Creep-rupture life versus stress at 704°C.

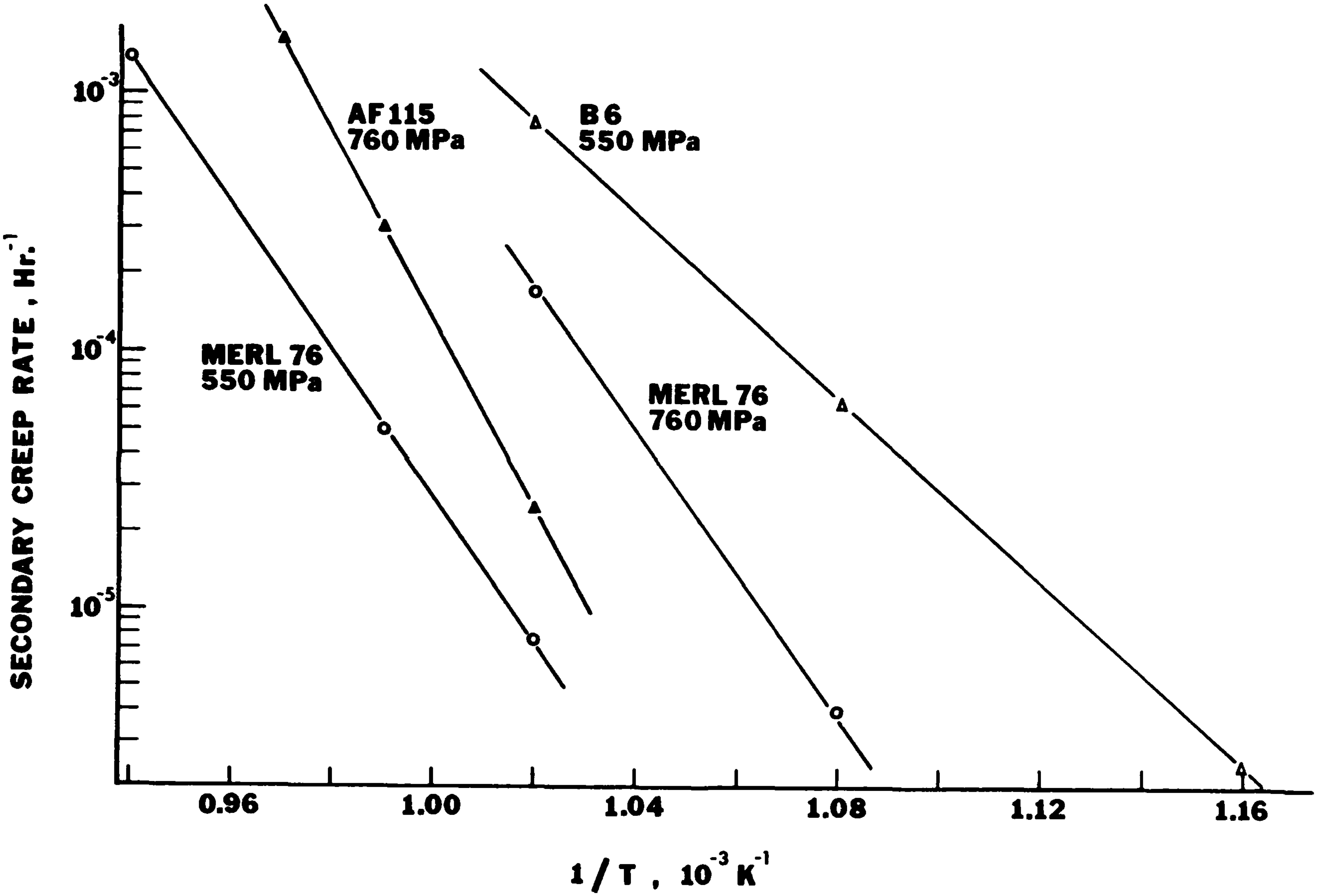

Figure 11 Secondary creep rate versus 1/T.

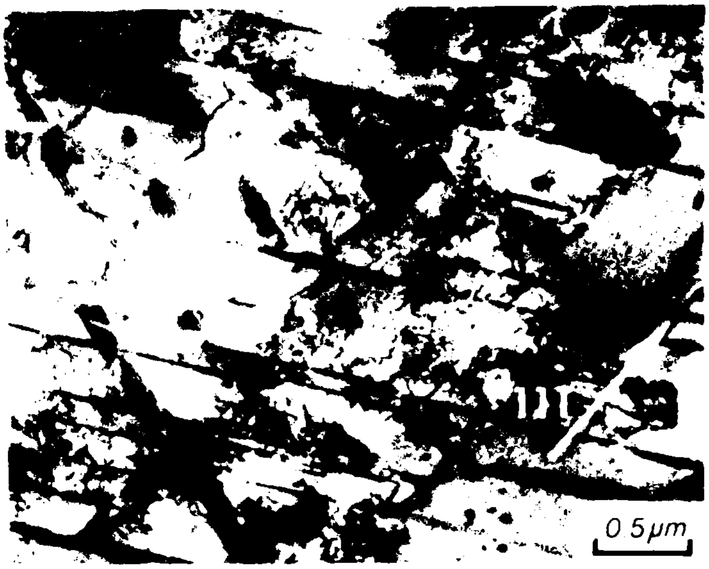

Figure 12 Stacking faults and dislocations in an AF115 specimen creep tested at 704°C/860 MPa to a strain of 0.002 in the secondary creep stage.

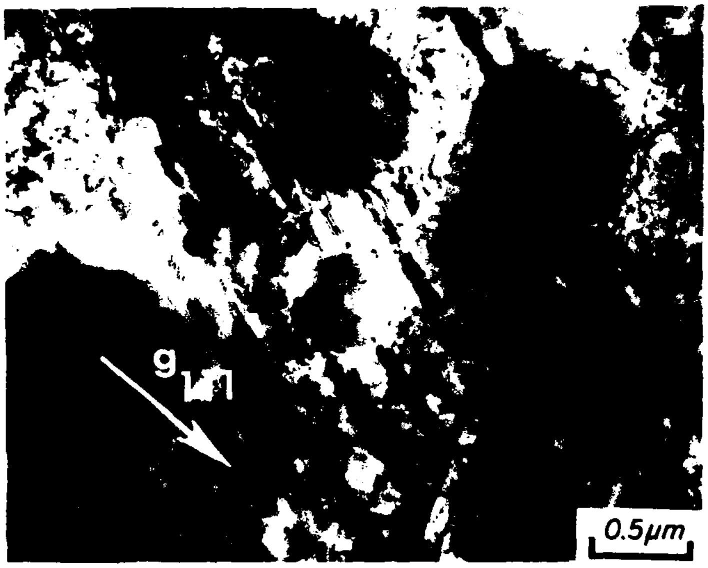

Figure 13 Stacking faults and dislocations in a B6 specimen creep-rupture tested at 704°C/690 MPa to a strain of 0.038 (fracture).

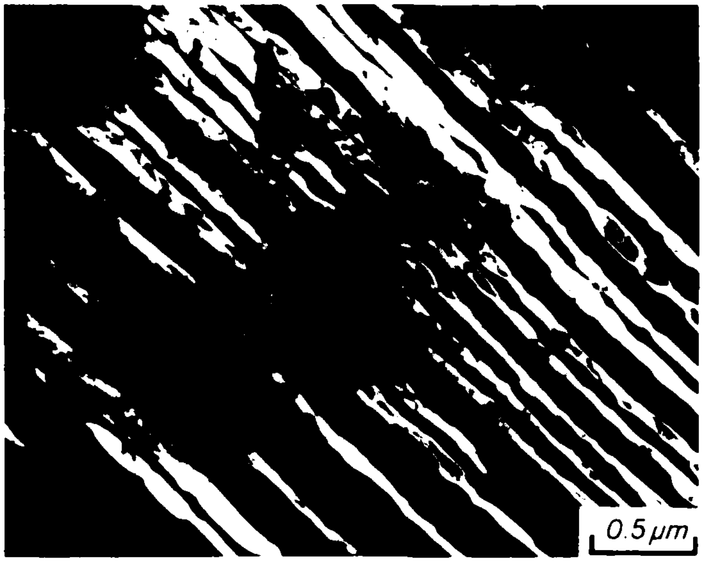

Figure 14 Microtwins in a MERL 76 specimen creep-rupture tested to fracture at 704°C/690 MPa. Dark field using a (020) twin spot.

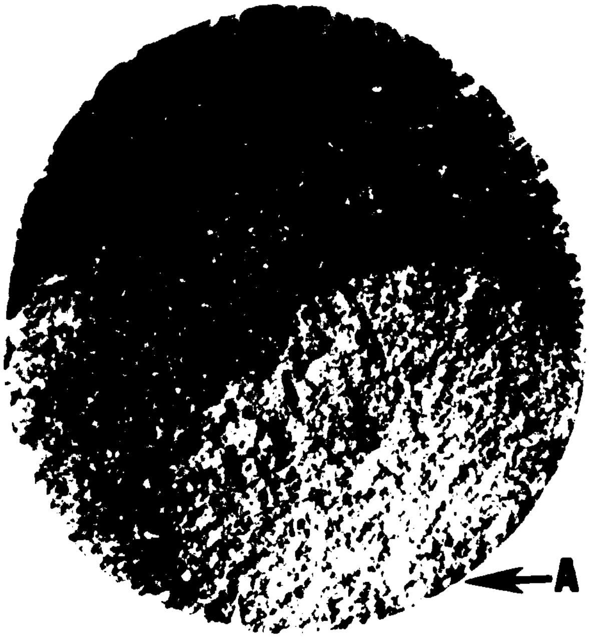

Figure 15 A typical appearance of the fracture surface of a stress-rupture tested specimen at 704°C. The dominant crack originated at surface A and propagated across region B before fast separation occurred across region C.

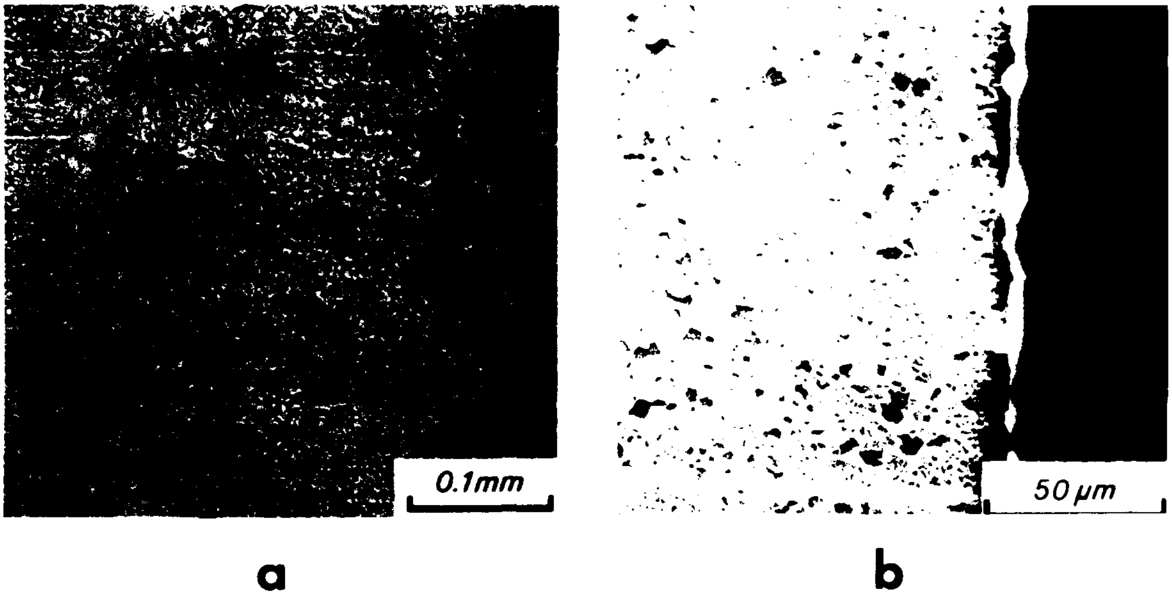

Figure 16 Cracks in an AF115 specimen creep-rupture tested to failure at 704°C/760 MPa (a) specimen surface, after a 12 μm layer was removed by polishing (b) longitudinal section.

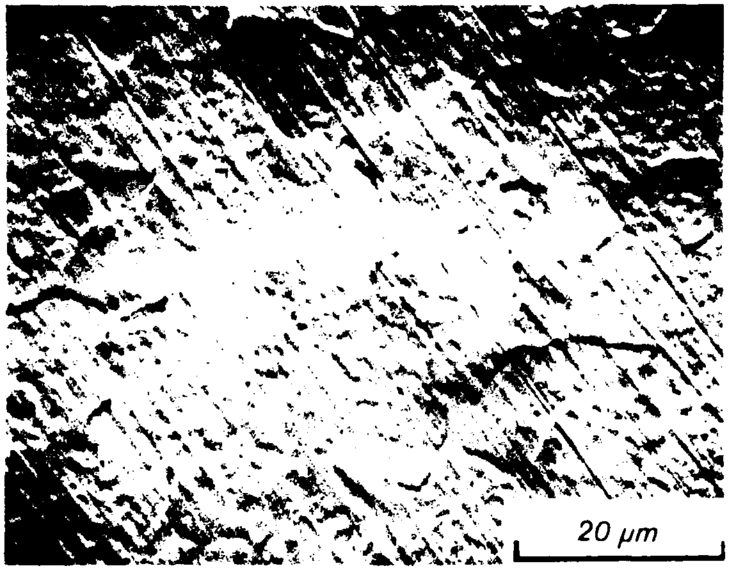

Figure 17 Surface appearance of a MERL 76 specimen creep-rupture tested in vacuum at 704°C/655 MPa to a strain of 0.008 in the secondary creep stage.

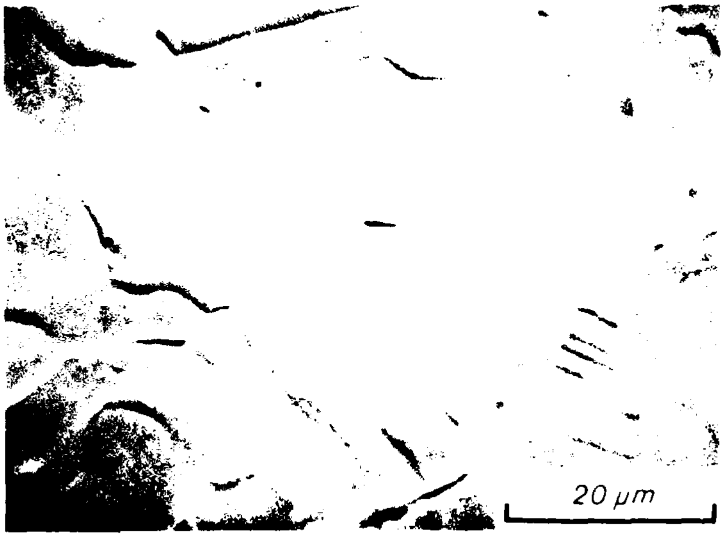

Figure 18 Slip bands and cracks at grain boundary triple junctions on the surface of a MERL 76 specimen creep-rupture tested in vacuum at 704°C/655 MPa to a strain of 0.04 in the tertiary creep stage.

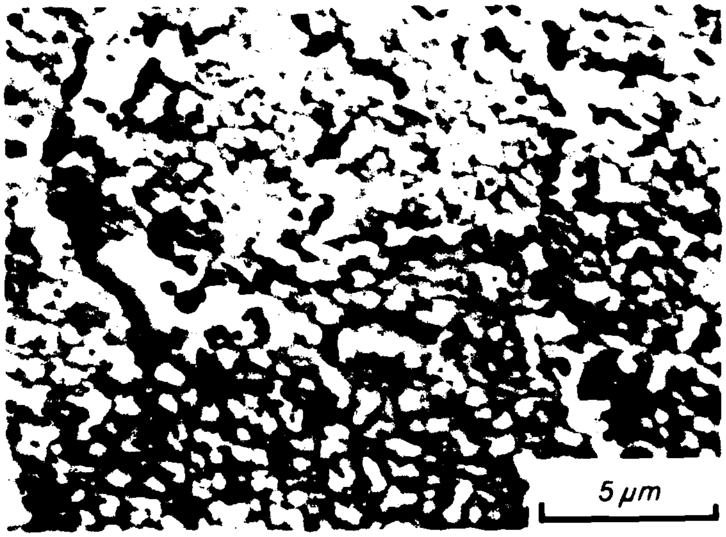

Figure 19 A longitudinal section of an AF115 specimen creep-rupture tested to failure at 704°C/860 MPa, showing the formation of cavities (white spots indicated by an arrow) adjacent to carbide particles and the coalescence of cavities to form microcracks. (Note: The contrast in this micrograph is inverted, cracks appear white and carbide particles appear black).

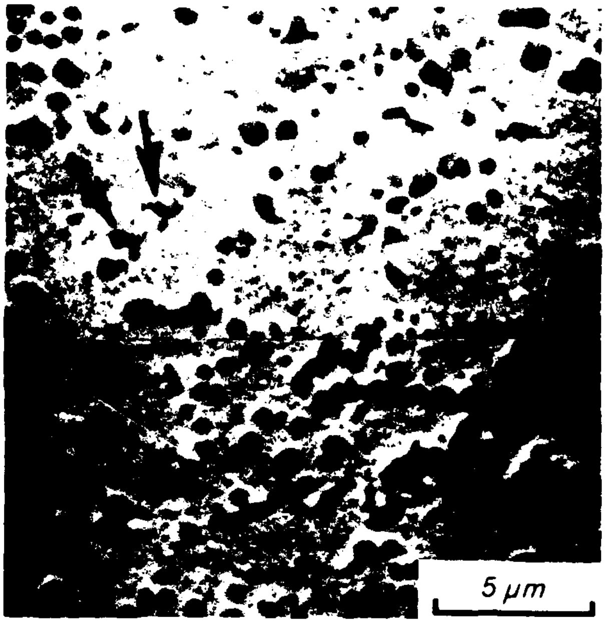

Figure 20 Cavities (arrow) and microcracks in a longitudinal section of a B6 specimen creep-rupture tested to failure at 704°C/690 MPa.

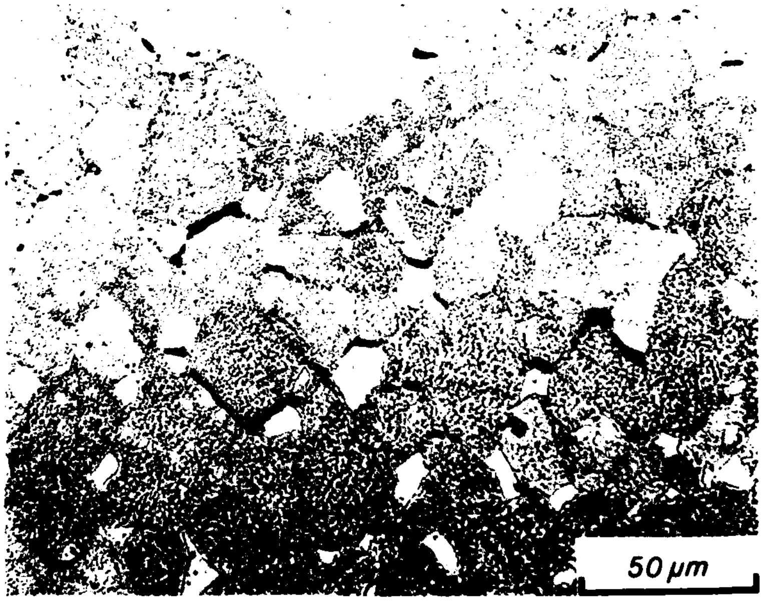

Figure 21 Internal cracks in a longitudinal section of a MERL 76 specimen creep-rupture tested to failure at 704°C/655 MPa.

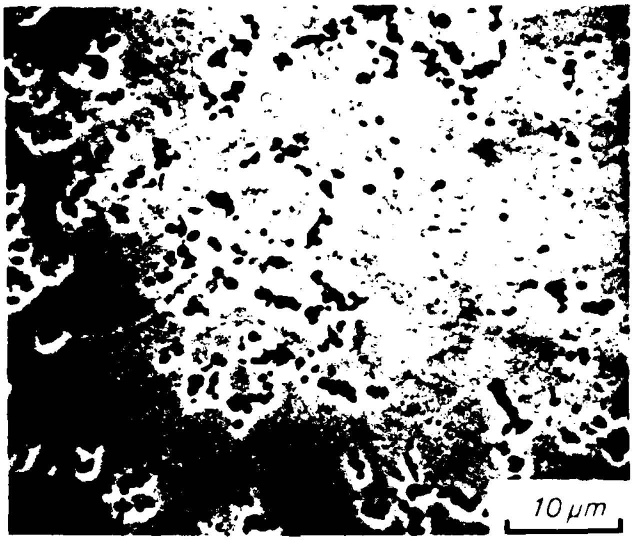

Figure 22 Cavities in a longitudinal section of a [illegible] specimen creep-rupture tested to failure at 704°C/448 MPa.

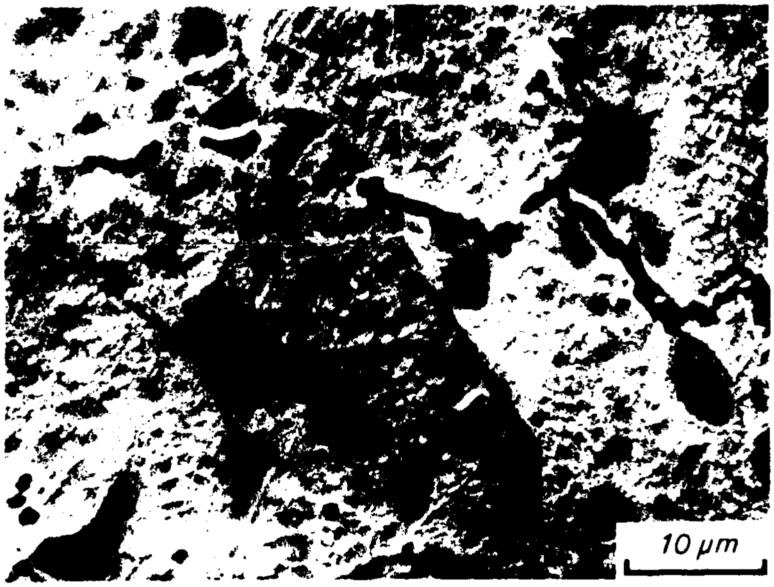

Figure 23 Intragranular cavities and cracks in a longitudinal section of a MERL 76 specimen creep-rupture tested to failure at 704°C/860 MPa.

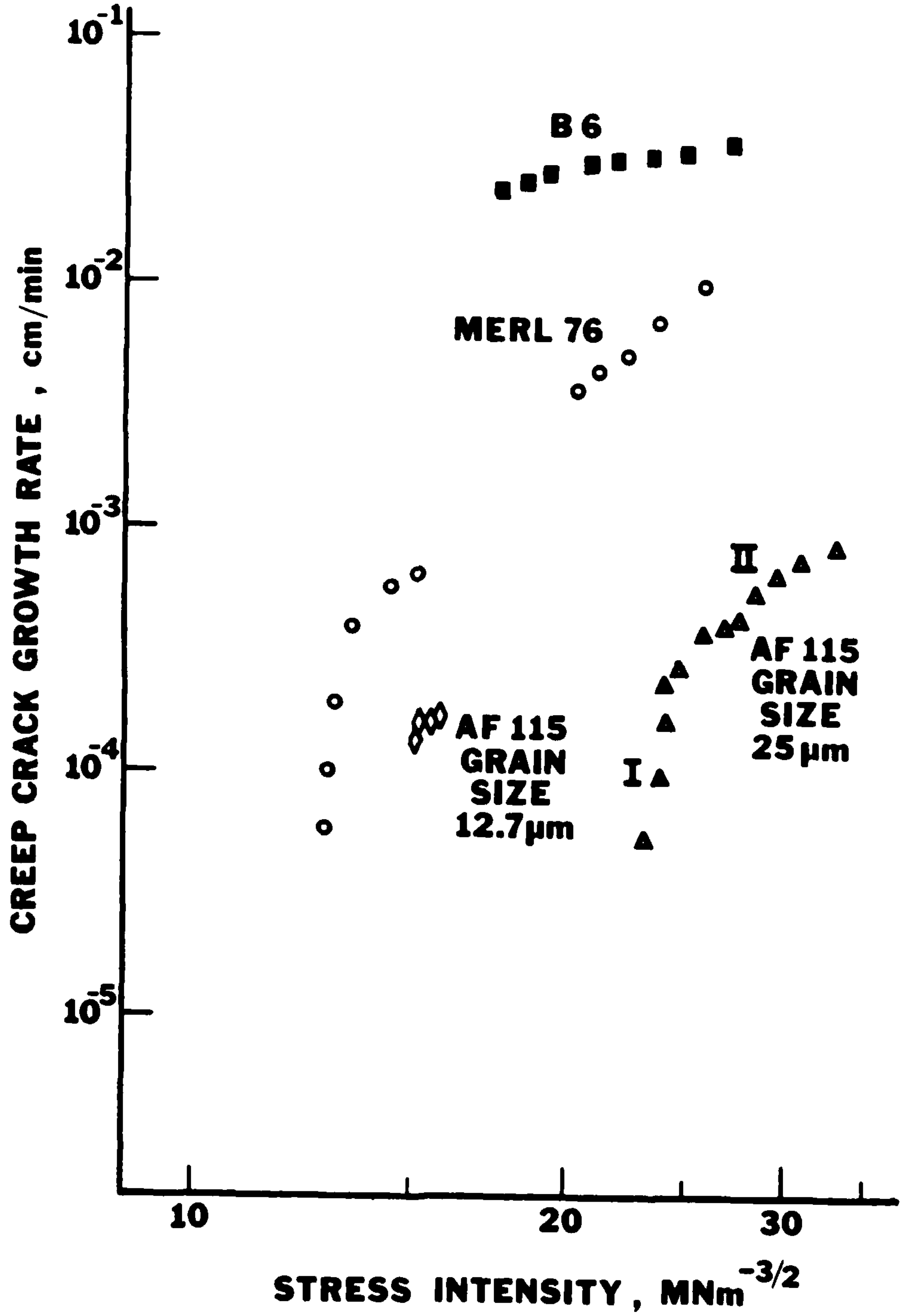

Figure 24 Creep crack growth rate at 704°C versus stress intensity.

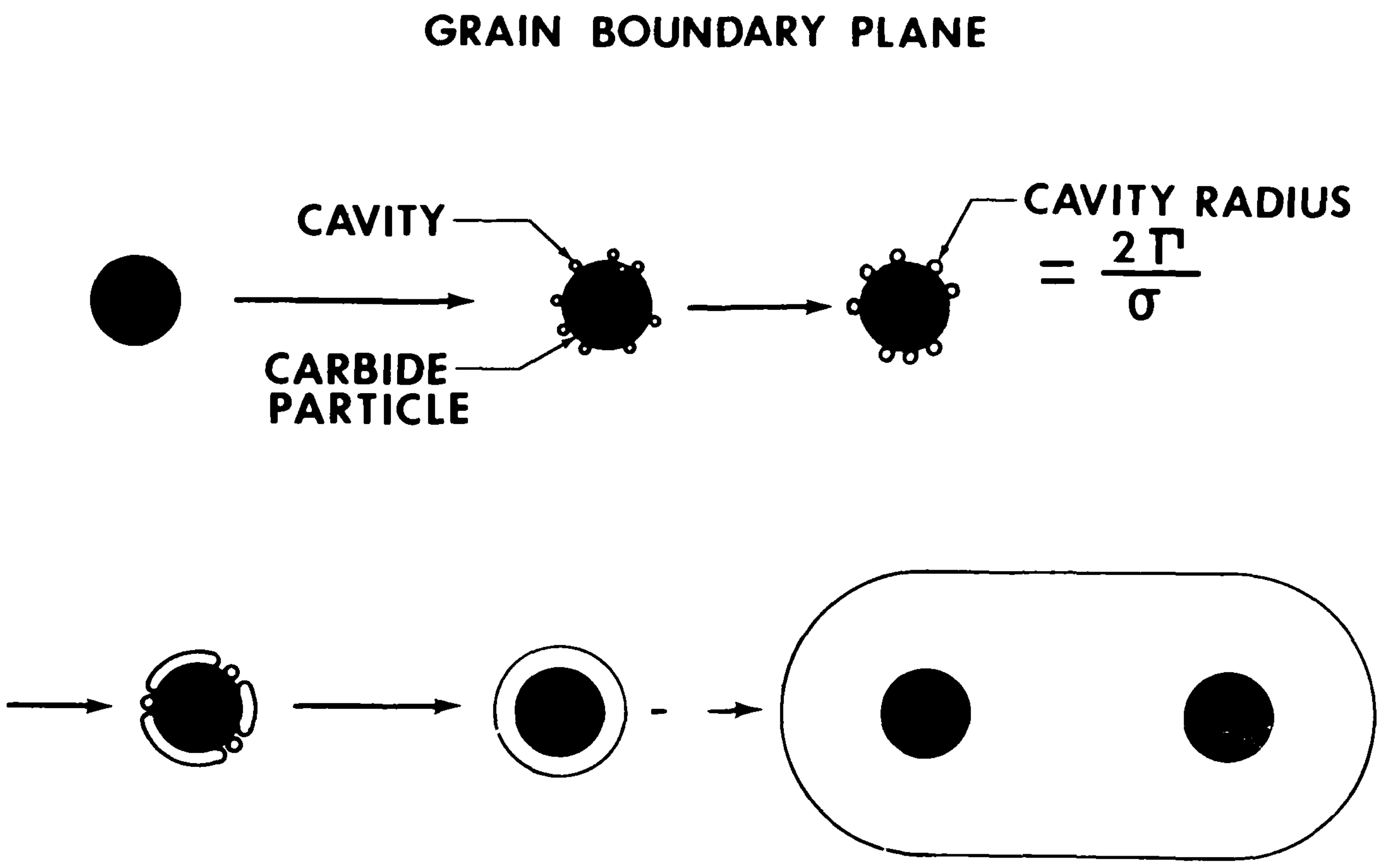
GRAIN BOUNDARY PLANE
CAVITY
CARBIDE PARTICLE
CAVITY RADIUS
$= \frac{2\Gamma}{\sigma}$

Figure [illegible] Schematic illustration of the development of a micro-crack in alloys [illegible] and [illegible].

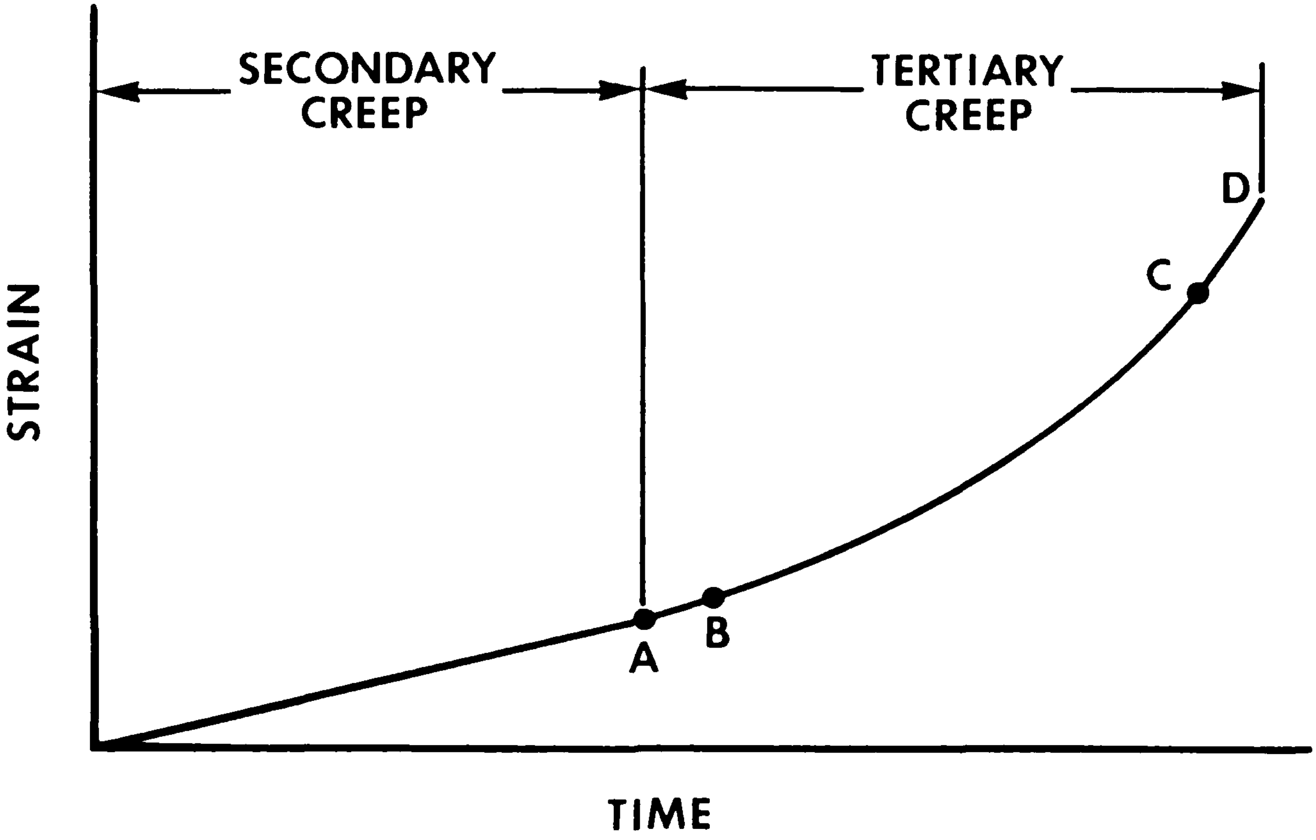

Figure 26 Proposed sequence of events for creep-rupture of a specimen. A: Growth of cavity to stable size in the bulk, B: Formation of surface cracks (10-100 μm), C: Visually detectable crack ([illegible]50 μm) and D: Failure ([illegible] μm). Note that internal cracks are about 10 μm.

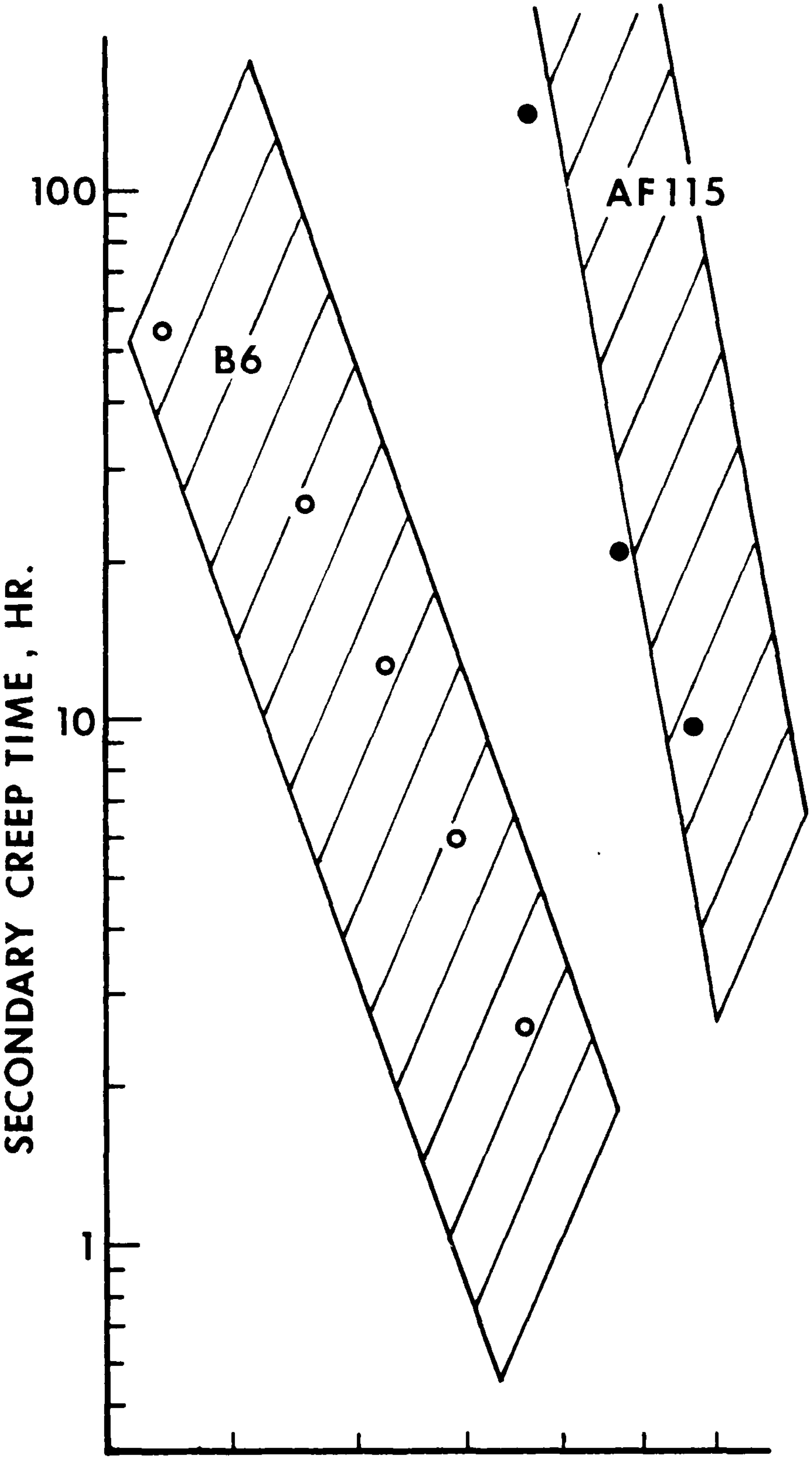

Figure 27 A comparison of the calculated secondary creep time (shadow bands) with the experimental data for alloys AF115 and B6.

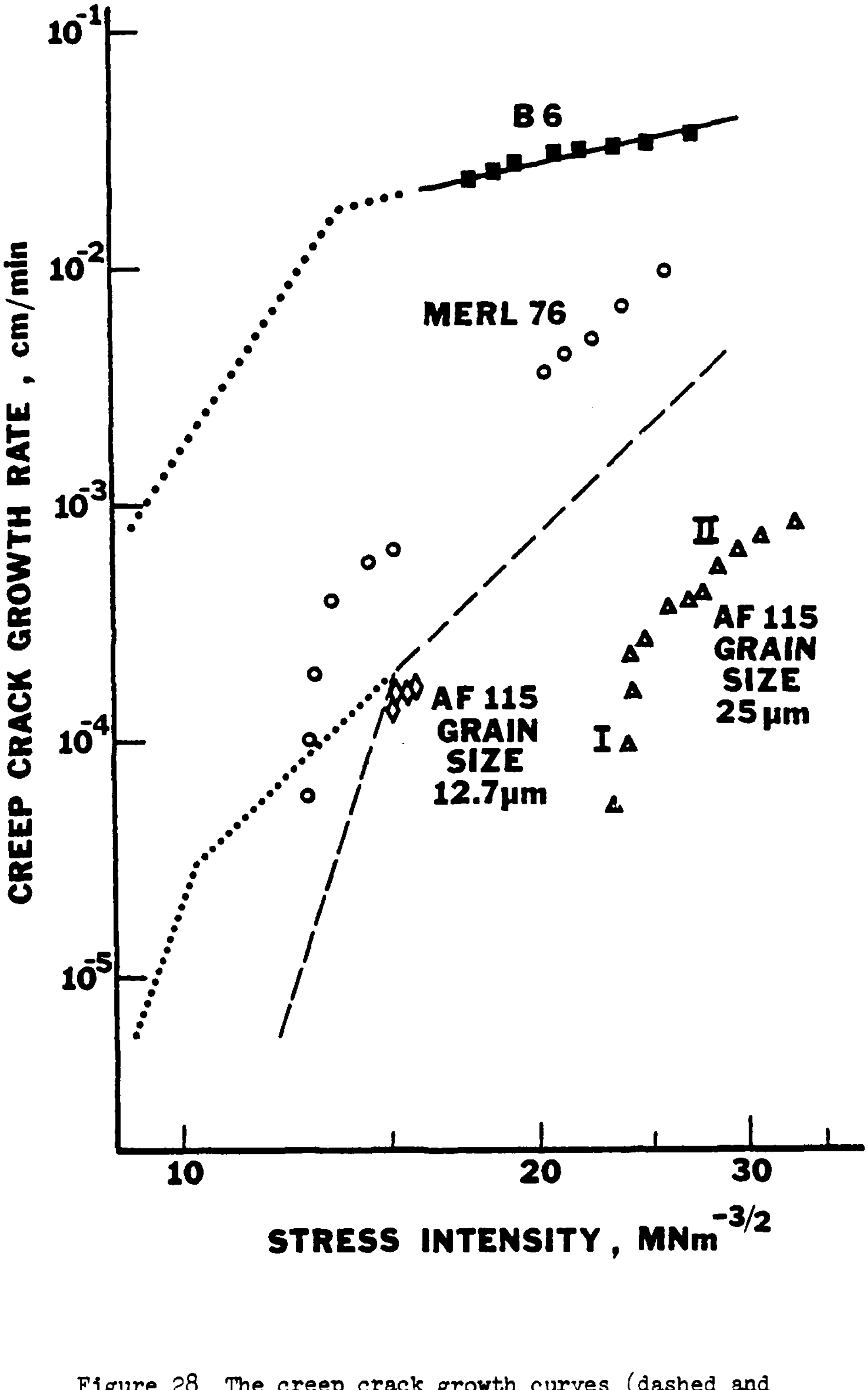

Figure 28 The creep crack growth curves (dashed and dotted) used for the calculation of the crack propagation lives of AF115 and B6.

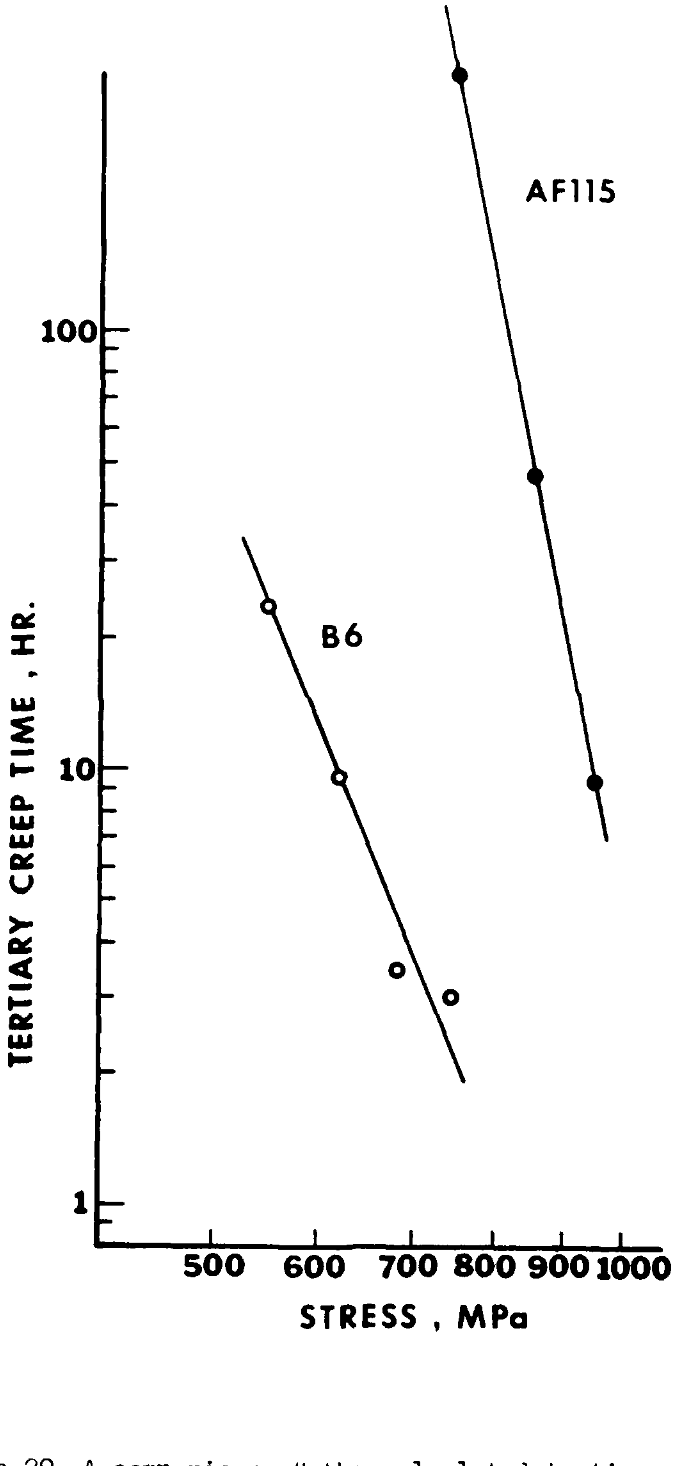

Figure 29 A comparison of the calculated tertiary creep time (solid lines) with the experimental data for alloys AF115 and B6.

SECTION 3.0 SECOND-YEAR PROGRAM

MESH SIZE EFFECTS AND NOTCH STRESS-RUPTURE PROPERTIES OF MERL 76

3.1 INTRODUCTION

The first-year program studied stress-rupture characteristics of a series of powder metallurgical nickel-base alloys. Structural features were identified which controlled the creep rates and rupture lives in smooth sections of the selected alloys. Although some preliminary results on the behavior of notched sections were obtained, it was clear that much remained to be done. Therefore, this study was continued into the second year of the program. The importance of notch behavior is clear from the configuration of engineering structures, the majority of which contain holes, slots, grooves, etc. for attachment of subassemblies and coupling of other components. Such features locally perturb the applied or working loads and these regions of stress concentration are often the life-limiting location in a part. At elevated temperatures, stress-rupture is a potential fracture mode and thus rupture properties in notched details are an important design consideration.

The second- and third-year programs were also structured in response to another major thrust that had developed in P/M metallurgy. The remarkable homogeneity of P/M materials had led to generally very uniform properties, but small discontinuities have been found to perturb this behavior pattern. Specifically, small non-metallic inclusions have been shown to set the minimum fatigue capability of these alloys. A comprehensive treatment of this subject will be found in the next section of this report detailing the third-year program. A method that has been suggested to reduce the size, and therefore the effect of inclusions, is to decrease the mesh size of the powder selected to make a consolidation. However, such a reduced mesh size could lead to changes in the properties of consolidated material; increased surface area, for example, could lead to higher interstitial element levels and poor bonding characteristics. The second-year program, therefore, studied the characteristics of fine mesh powder and properties obtained from such material.

Both topic areas selected for study in the second year will be described in the following sections. Experimental procedures common to both program elements will be described in Section 3.2, the Fine Mesh Powder results in Section 3.3, and the Notch Stress Rupture study and analysis in Section 3.4.

3.2 EXPERIMENTAL

Preparation of Materials. The alloy MERL 76 used in the present study was vacuum induction melted and argon atomized. The -80 and -325 mesh powder fractions were separated by screening and small samples taken for characterization. Additional material was outgassed at room temperature prior to filling a pre-evacuated container, the container was sealed and consolidated by hot isostatic pressing (HIP). Heat treatments of the consolidated materials were performed in a muffle furnace with temperature control of ±10°C.

Specimens and Mechanical Testing. The dimensions of the tensile and creep specimens and notch-rupture specimens ($K_t = 3.8$) are given in Figure 1a and 1b, respectively. The dimensions of the tensile specimens were similar to those of the creep-rupture specimens. Much of the early creep- and notch-rupture testing was performed under constant loads. Creep strains were continuously recorded from LVDT affixed to the test specimens; the accuracy of the strain measurement was 0.01%. More recently some of the testing, together with tensile and stress relaxation tests, have been performed on a computer controlled MTS machine. The specimen used for stress relaxation studies is the same as that for the creep test.

Analytical Methods. Standard metallographic techniques were used throughout the study to monitor structure and fracture appearance of the material. Scanning microscopy was employed not only to examine powder and fracture surfaces, but also to study nucleation behavior in notched specimens. A sufficiently large stage was available to hold a notched specimen so that the notched region could be examined directly at various stages of a test. A specially developed extraction method was also used to characterize powder particle surfaces. The method, illustrated in Figure 2, consists of dispersing the particles to be studied on a support medium. Carbon is then deposited on these particles. A carbon extraction replica of the surface region is obtained by breaking the carbon film around selected particles and immersing the assembly in a bromine/tartaric acid/methanol solution. The etchant penetrates under the film dissolving the metal but leaving the secondary particles attached to the replica surface. Morphological and structural analysis can be performed in a transmission electron microscope. Additional information on the chemical constitution of powder particle surfaces was obtained by Auger electron spectroscopy. Sputtering of surface layers allowed concentration/depth profiles to be obtained for several elements.

3.3 THE EFFECT OF MESH SIZE ON THE MICRO-STRUCTURE AND PROPERTIES OF MERL 76

3.3.1 Introduction

The objective of this part of the program was to determine any effect of the mesh fraction selected to fabricate consolidation on microstructure and properties. Consolidation of -325 mesh MERL 76 powder was performed at temperatures of 1177°C and 1200°C which are below and above the γ' solvus of MERL 76 (1190°C). Two different heat treatments were used, a simple solution and age treatment: 1120°C/2 hr/AC + 760°C/8 hr/AC, and a multi-stage solution and age treatment: 1163°C/2 hr/furnace cooled to 1130°C/OQ + 870°C/40 min/AC + 980°C/45 min/AC + 650°C/24 hr/AC + 760°C/8 hr/AC.

The former heat treatment was also used for the -80 mesh material during the first-year program, the data of which will be compared with those generated from the -325 mesh powder. The latter heat treatment, which is currently used for MERL 76 in other programs, will be used in the present study to evaluate the effect of grain size on creep-rupture behavior of MERL 76.

3.3.2 Results

Powder Characterization. The particle size distribution of the -325 mesh powder and -80 mesh powder can be approximated by the Weibull equation

$$W = \exp - (d/d_0)^B$$

where W is the weight fraction of powder particles with diameters larger than a specific particle diameter d; d_0 and B are constants which have values of 22.5 m and 1.21 for the -325 mesh powder and 60 m and 1.52 for the -80 mesh powder. From the particle size distribution, it can be calculated that for a given weight, the -325 mesh powder particles have about four times as much surface area as the -80 mesh powder particles.

The powder particle surface appearance of the -325 mesh powder and -80 mesh powder are similar. In both cases, three different morphologies have been observed: the "typical" dendritic morphology (Figure 3a) which is associated with a broad range of powder particle sizes, except the smallest; a granular morphology (Figure 3b) which is usually observed in powder particles of intermediate sizes; and the powder particles with featureless surfaces (Figure 3c). The latter type is only found in small powder particles. As might be expected from these different surface morphologies, three different microstructures of the powder particles have been observed and are shown in Figure 4. Figure 4a shows the dendritic microstructure and the granular microstructure in the bottom particle in Figure 4b. This figure also includes a particle with a mixed granular and dendritic microstructure, from this it appears that both microstructures are closely related. Another type of unusual microstructure is shown in Figure 4c which illustrates a powder particle with a segregation-free surface layer and a core which shows a mixed granular and dendritic microstructure. Both the segregation-free layer and the granular microstructure are thought to be produced with conditions of undercooling at the growing solid-liquid interface during powder solidification. In particular, it is envisaged that the segregation-free layer solidified initially under a high degree of undercooling until the release of heat of fusion raised the temperature of the interface to the near-equilibrium value and normal, segregated dendritic growth in the core ensued.

The surface structure of the -325 mesh powder particles has been studied by extraction replica techniques. A typical result is illustrated in Figure 5 which reveals only a small number of equiaxed particles (500°A diameter) on the powder particle surfaces. These particles have not been identified as yet, for no electron diffraction pattern has been obtained. The morphology, based on previous studies, suggests that they are MC-type carbides. Auger electron spectroscopy of two powder samples, one containing particles with diameters less than 10 μm and the other containing particles with diameters 130-180 μm, reveals little difference in the segregation of alloying elements to the surface. The only discernible difference between the two mesh sizes is in the oxygen and carbon contents, which decreased at a slower rate with surface removal by sputtering in the case of the fine powder sample. The oxygen and nitrogen contents of the -325 mesh and -80 mesh powders, as determined by chromatography before and after consolidation,are given in Table I. This table shows that the oxygen contents of the finer powder particles are higher than the -80 mesh powder both before and after consolidation. This increased oxygen content in the finer powder particles is attributed to the larger amount of surface adsorbed oxygen.

Microstructure. The compositions of the consolidated -80 mesh and the -325 mesh MERL 76 are given in Table II from which two differences should be noted. The -80 mesh composition has a slightly higher hafnium content and a lower oxygen content. As a result of the former difference, primary gamma prime particles are larger in the -80 mesh consolidation than those in the -325 mesh consolidation (Figure 6). As shown in the previous section, the increased oxygen content in the -325 mesh consolidation is related to the larger amount of surface adsorbed oxygen associated with the finer powder particles. The grain sizes of the -80 mesh and the -325 mesh consolidations are 21 μm and 12.4 μm, respectively. It is likely that this difference is attributable to a higher HIP temperature in the case of the coarse powder (although the nominal HIP temperature for both was 1177°C) rather than to the initial powder particle sizes. No such differences have been found in other programs in which consolidation of the two mesh sizes were produced in the same HIP run.

Mechanical Properties. The 704°C tensile properties of the -80 mesh and the -325 mesh MERL 76 consolidations are given in Table III which shows that the -80 mesh consolidation has lower yield strength but higher ductility than the fine-powder consolidation. These differences can be correlated with the variations in grain sizes between the two consolidations rather than with an effect of the initial powder particle sizes.

The 704°C stress-rupture properties of the smooth specimens and notched specimens ($K_t = 3.8$) from the two consolidations are given in Table IV and plotted graphically in Figure 7. Both the smooth-rupture lives and the ductility of the -80 mesh material are somewhat better than the -325 mesh consolidation. These differences again stem from a difference in grain size rather than to a difference in the initial powder particle size. At lower stresses, the notch-rupture lives of the -325 mesh are inferior to those of the -80 mesh consolidation. However, the notch-rupture lives of the -325 mesh consolidation appear to be better than those of the -80 mesh consolidation at stresses higher than 655 MPa.

We may note that there is some scatter in the notch-rupture lives, a characteristic that we shall return to in following sections.

Effect of Grain Size. The range of grain sizes which one can obtain in HIP-consolidated MERL 76 is rather limited. HIP at temperatures of practical interest below the gamma prime solvus produces grain size of about 12 μm. HIP at temperatures above the gamma prime solvus (1190°C) results in rapid grain growth; however, the maximum useful temperature is limited by the onset of incipient melting (1200°C). The grain size produced by HIP at 1195°C is about 24 μm.

The tensile properties of the fine-grain (12 μm grain diameter) and the coarse-grain (24 μm grain diameter) MERL 76 were quite similar. An important effect of grain size is on stress-rupture life; smooth (K_t = 1) specimens results are given in Table V and plotted in Figure 8. These results show that the stress-rupture lives of the coarse-grain material are longer than those of the fine-grain material at all stresses. However, the difference becomes small as the stress increases. The stress-rupture ductility of both materials appears to be similar at most test conditions, increasing at higher stresses. At 550 MPa the coarse-grain material exhibits a rather low ductility (less than 2 percent). The notch-rupture lives again show large variations (one to two orders of magnitude) at high stresses for both material conditions.

The recurring scatter in notch-rupture properties resulted in a major effort aimed at elucidating controlling factors in notch location, a topic considered in some detail below.

3.3.3 Conclusions

Although certain chemical and structural differences between -325 and -80 mesh fraction powders were found, these did not appear to have any influence on the properties of consolidations. It may be concluded that, if processed correctly, parts made from -325 mesh powder will exhibit acceptable tensile and creep-rupture properties which will be coupled with an improved fatigue capability.

3.4 NOTCH-RUPTURE PROPERTIES OF MERL 76 - PHENOMENOLOGY AND ANALYSIS

3.4.1 Introduction

The objective of this part of the project was to identify the critical factors that control stress-rupture properties of notched sections. If possible, the behavior pattern would be modelled in order to establish a predictive capability. The material and processing sequences for MERL 76 used in this study were similar to those used in the first-year program (Section 2). A brief summary of the experimental details and smooth section properties is as follows. Material was consolidated from -80 mesh powder by hot isostatic pressing. Two heat treatments which produced extremes in notch behavior were selected for this study; both involved a solution treatment at 1120°C and an aging at 760°C.* The difference is in the cooling rate from the solution treatment temperature; one sample was quenched in oil and the other was cooled in air, hereafter referred to as OQ material and AC material, respectively. Microstructures, illustrated in Figure 9, showed two significant differences. Firstly, the secondary gamma prime particles are considerably finer in the OQ material. Secondly, except for the blocky primary gamma prime particles which are mainly at grain intersections, the grain boundaries in the OQ material are rather straight and featureless. In contrast, gamma prime particles have precipitated along the grain boundaries in the AC material during cooling from the solution treatment temperature. These microstructural variations caused relatively small differences in smooth-section properties and may be summarized as follows. The OQ material has a higher yield strength (1100 MPa versus 980 MPa) and a lower tensile ductility (18 percent versus 24 percent elongation) than the AC material. Under creep conditions, the OQ material has a lower minimum creep rate, slightly longer rupture life, and lower rupture ductility than the AC material. However, the stress dependence of the creep-rupture properties of the two materials is similar. Creep deformation in both materials is heterogeneous, involving concentrated shear on few slip planes and microtwins formation (2). In spite of these apparent similarities in smooth-section properties in these two materials, vast differences in notch behavior are observed which are described in the following section.

* Note that neither of these heat treatment sequences are used for MERL 76 components (1).

3.4.2 Notch-Rupture Behavior

The geometry of the bar specimen used in this study is illustrated in Figure 1b. The theoretical elastic stress concentration factor (K_t) at the notch root is 3.8. Standard notch tests were conducted at 704°C and at a net-section stress of 690 MPa, which resulted in notch lives of about 2 h for the OQ material and about 100 h in the case of the AC material. For comparison, the rupture lives of smooth specimens are slightly over 100 h for both materials. The notch-brittleness of the OQ material persists to stresses as low as 420 MPa where differences in notch lives between the two materials are over two orders of magnitude.

It is customary for metallurgists and material scientists to associate notch-brittleness with "unfavorable" microstructures, environment, and/or deformation mechanisms (3-5). Alternatively, analyses of local stresses and strains in the plastic zone at the notch root, using constitutive equations derived from smooth specimen data, have also been proved successful in understanding some aspects of notch behavior (6-8). A synthesis of both viewpoints is deemed essential for a basic understanding of the notch-rupture phenomenon. The experiments described below are designed to provide the basic framework for establishing such a synthesis. Some of the reasoning behind certain parts of the study is as follows.

Under a net-section stress which is smaller than the macroscopic yield stress, a notched section will deform in a rather complex manner. At sufficiently high stresses during loading and before the maximum load is reached, a small volume of material at the notch root deforms plastically, because of the stress concentration, while the bulk remains elastic. Upon reaching the maximum applied load, the plastic deformation at the notch root is constrained by an elastic core and subsequent plastic flow is, therefore, dominated by a strain-controlled creep relaxation phenomenon. Typically, the stress and the rate of deformation are the highest initially and decrease rapidly with time toward steady state values determined by elastic stresses in the bulk. These considerations indicate that a significant portion of the plastic strain in the notch is accumulated during the initial stages of the test. The nature of this deformation and the accompanying damage depend on the relative contribution of various deformation mechanisms and are determined by factors such as stress, deformation rate, temperature, and environment. At high temperatures, a slower rate of deformation results in a larger amount of grain-boundary sliding than a faster rate of deformation (9). Thus, if grain boundary sliding contributes to the notch-brittleness, a fast loading rate should be beneficial. Loading rate effect can also be interpreted from an entirely different point of view. For a given amount of notch deformation, a slow loading rate subjects the material at the notch root to high stresses for a longer period of time than a fast loading rate. Thus more material damage could be produced at the notch root when a slower loading rate is used. It, therefore, follows that, in addition to stress and temperature, the stress/temperature path along which a maximum load is applied should be an important notch-rupture test variable.

In general, the variables which govern the notch-rupture behavior of a material fall into four categories:

(1) Test parameters such as temperature, stress and, as considered above, stress/temperature path.

(2) Specimen parameters such as geometry and surface conditions.

(3) Microstructural parameters such as grain size and grain boundary microstructures.

(4) Environment.

Results presented below illustrate effects of some of the variables in each category.

Test Parameters. The effect of stress on the notch lives of the OQ and the AC material at 704°C is illustrated in Figure 10. For comparison, the rupture lives of smooth specimens, which are rather similar for these two materials, are also included in the figure. The notch lives of the OQ material show two distinctly different stress dependencies. At stresses over about 420 MPa, the OQ material has short notch lives which are relatively insensitive to stress. Further, a puzzling feature at this stress region is that large scatter (up to two orders of magnitude) in rupture lives is frequently encountered (see also Table V). At stresses slightly lower than 420 MPa, the notch lives increase abruptly by more than two orders of magnitude and approach the rupture lives of smooth specimens. In contrast, the notch lives of the AC material are considerably longer, equal to or slightly lower than the rupture lives of smooth specimens in the stress range studied, and are more stress dependent. No large scatter in notch lives was observed in the AC material.

The effect of temperature on the notch life of MERL 76 at 690 MPa is shown in Figure 11. The temperature dependence of notch lives for both the OQ and the AC materials appears to be similar. There is a rapid increase in notch lives below 704°C and notch-brittleness is absent at about 675°C.

The conventional procedure for creep-rupture or notch-rupture testing is to equilibrate the specimen at the test temperature before applying the load by placing standard weights on a load pan. This procedure precludes controlled variation of loading rates. Therefore, the effect of loading rate on notch life of the OQ material was studied using a servo-hydraulic testing machine. Notch specimens were equilibrated at 704°C before loading at various rates to a net-section stress of either 550 MPa or 690 MPa. Results are illustrated in Fig.12. At a net-section stress of 550 MPa, a very significant improvement of rupture lives was observed at loading rates 4135 MPa/minute or higher. However, no effect of loading rate was observed if the net-section stress was increased to 690 MPa.

To study the effect of loading temperature on notch-rupture life, specimens were first equilibrated at a selected temperature. The load was applied in a conventional manner until a net-section stress of 690 MPa was reached, maintained at 690 MPa for 0.5 h and during subsequent temperature increase to 704°C. Results illustrated in Figure 13, show that the notch-brittleness associated with isothermal testing at 704°C was eliminated when the loading temperatures were lower than about 480°C.

Specimen Parameters. Notch specimens with only one geometry, given in Figure 1b, were used in this study; the only specimen parameter that was studied in some detail was surface treatment. Five conditions were examined: as-machined, electropolished, electropolished plus nitrogen ion implanted, as-machined plus prestrained, and as-machined plus glass bead peened. Nitrogen ions were implanted at 100 Kev and at a dose of 10^{17} ions/cm^2. To prestrain a specimen it was first equilibrated at a temperature at which the OQ material is notch insensitive, loaded to the predetermined stress level and then the load was released. Prestraining and peening were anticipated to have similar effects on notch-rupture behavior through the worked surface layer and residual stress pattern which were introduced. These surface treatments were applied to the OQ material, and specimens were tested conventionally at a standard test condition of 704°C/690 MPa. Results, given in Table VI show that shot peening significantly increases notch lives while other surface treatments have no beneficial effect. Beneficial effects associated with shot peening are usually considered to be the deformation structure and the accompanying compressive residual surface stresses. Conversely, the poor response of the prestrained specimens may be attributed to a relatively smaller and less homogeneous deformation which could have resulted in a deformation structure and a residual stress pattern quite different from those in the peened specimens. Except for the alloying effect, ion implantation may be viewed simply as shot peening in atomic scale. The low notch lives of the nitrogen implanted specimens may be due to a high mobility of the nitrogen atoms at the test temperature used. If this is the case, implanting different atomic species may well produce different results.

Microstructural Parameters. Since details of crack nucleation in an air-tested specimen were obscured by oxidation, crack initiation behavior at the notch root was studied by testing electropolished specimens in a vacuum. The tests were interrupted periodically for crack inspection using a scanning electron microscope. Microcracks were detected on the notch surfaces of either the OQ of the AC materials after about 50 h of testing at 704°C/690 MPa. In the OQ material microcracks preferentially nucleated at and propagated along grain boundaries as shown in Figure 14a. The crack nucleation sites were smoewhat different for the AC material in which microcracks formed at several locations (Figure 14b): at gamma prime:gamma interface (arrow 1), within large gamma prime particles (arrow 2), at machining cracks normal to the stress axis (arrow 3) and at grain boundaries. The first three types of microcracks propagate transgranularly in a direction normal to the stress axis. Grain boundary microcracks were seldom observed in the AC material at test times less than 120 h. However, with increased test times, the development of grain boundary microcracks became increasingly evident and would eventually lead to intergranular fracture. These differences in crack nucleation behavior between the OQ and the AC materials may be attributed to a synergistic effect of two factors. Firstly, the grain boundaries in the OQ material are subjected to higher stresses because of the more creep-resistant grain matrix. Secondly, the grain boundaries in the OQ material are less resistant to shear deformation because of a lack of grain-boundary pinners (Figure 9).

Because of the intergranular fracture, grain size is expected to have an effect on notch-rupture life. Data given in Table V indeed show that the notch-rupture of MERL 76 increases with increasing grain size.

Environmental Parameters. The effect of testing in a vacuum was studied using the OQ material which was tested conventionally at a standard condition of 704°C/690 MPa. Results are given in Table VII which show that environment plays an important role. However, the magnitude of the rupture life improvement is surprising. More importantly, it has also been observed that testing 6 h in a vacuum followed by testing in air also dramatically increases the notch-rupture life. This observation is consistent with the expectation that the crucial part of a notch test is in the initial stages where most of the deformation takes place. Further, it also suggests that it is the interaction of air (or one of its constituents) during the plastic deformation, rather than oxidation per se, which causes the premature notch failure. It is also clear from results cited in this and the previous section that both the crack nucleation and crack growth characteristics are modified by the environment.

3.4.3 Ancillary Tests

Stress Relaxation. One of the puzzling aspects of the present study was the extreme contrast in smooth and notch behavior. The notch properties showed great differences whereas the smooth section tests showed rather similar characteristics for both material conditions (Figure 10). However, it should be realized that the notch deformation does not occur under a constant stress. As noted previously, the creep deformation at the notch after the full load has been applied, is dominated by a strain-controlled relaxation phenomenon. To gain insight into the notch-rupture behavior, therefore, stress relaxation in the OQ and the AC materials at 704°C was studied using smooth specimens. Relaxation data, shown in Table VIII, were obtained by applying a predetermined tensile strain or stress at which point the elongation of the specimen was kept constant and the decrease in stress with time was recorded. A most interesting finding of this study is that the OQ specimens fractured in less than 1 h during relaxation when the initial stresses exceeded 1226 MPa, which corresponds to a tensile strain of only about 0.04. Significantly, no fracture occurred in AC specimens even when tested to stresses as high as the tensile strength. Notches also experience high stresses initially so that there is an obvious correlation between the observed relaxation behavior and the notch-rupture behavior. Further, it has also been demonstrated that the fracture behavior of the OQ material during stress relaxation also depends on the tensile strain rate used. For a constant final tensile strain, a strain rate of 0.01 per minute resulted in fracture during stress relaxation, whereas no fracture occurred during stress relaxation when a strain rate of 0.10 per minute was used (10). This observation, again, is analogous to the loading rate effect on notch-rupture behavior. Thus, the simple stress relaxation experiments capture some of the basic features of the notch-rupture phenomenon and provide information that is not complicated by the multiaxial stress states in a notch, for which no complete analytical solution exists. It was considered that an understanding of the simple stress relaxation results is a prerequisite to any satisfactory notch analysis. To predict failure during either a smooth (relaxation) or a notch test, a fracture criterion is obviously needed which involves damage accumulation under varying stresses or strain rates. In an attempt to define a satisfactory criterion, decrement and increment creep tests were performed as described in the following section.

Creep Damage Accumulation. The final group of specimens were creep-tested at 704°C, the stress was changed in a stepwise manner after a holding period equal to about 0.25 of fracture life at a predetermined level. The results of these stress decrement and increment creep tests are given in Table IX. The sum of the ratios of hold time t at stress σ_i to rupture time t_F at the same stress, which is used as a measure of creep damage, is also shown in the table. The more damaging loading sequences are reflected in smaller life fraction sums. Table IX shows clearly a strong loading sequence effect and the importance of the initial stress on cumulative life fraction at fracture. For the same stress range, the total life fraction at failure under increasing stresses (Specimen 237) is significantly larger than that under decreasing stresses (Specimens 233 and 234). A comparison between specimens 233 and 240 shows that, for the same loading sequence, the higher initial stress resulted in a significantly smaller total life fraction at fracture than the lower one. It is also interesting to contrast the behavior of the OQ material (Specimen 233) with the AC material

(Specimen 238). Although the OQ material generally has a longer creep-rupture life than the AC material under constant stress, the AC specimen showed a slightly longer cumulative life in a decreasing stress situation where the initial stress is above the yield strength. These results will be discussed in terms of existing creep-rupture criteria later. Note that the variation of life-fractions at fracture cannot be attributed to microstructural changes during creep at 704°C since none were detected in the present study.

3.4.4 Discussion

This study, if nothing more, has demonstrated the complexity of the rupture characteristics of notched sections of a nickel-base alloy. The variety of factors that can change rupture life by orders of magnitude in the OQ MERL 76 is impressive but only serves to increase the difficulty of providing a satisfaction qualitative model of the rupture process. In the first part of this discussion, we shall concentrate on the mechanical parameters of the rupture process and rely heavily on the intriguing parallel between stress relaxation and notch fractures. A quantitative analysis of the notch data has not been attempted in the present study since several fundamental problems remain unresolved. Among these are the effect of the multiaxial stress states on rupture behavior and the lack of a fracture criterion under varying multiaxial stresses. We shall begin by examining the applicability of of several suggested theories for failure of smooth sections.

Johnson, et al., first studied the nature of the applied stress system on creep rupture times (11) in which two extremes in rupture behavior were distinguished, as examplified by copper and aluminum. The rupture time of copper was determined to depend on the maximum principal stress, while the rupture time of aluminum was determined by the octahedral shear stress. The behavior of other alloys, especially creep resistant alloys, falls between these two extremes. In these materials it may be possible that crack initiation is governed by the octahedral shear stress, and crack propagation by the maximum principal stress (12).

The problem of defining a creep-rupture criterion under seemingly simple unaxial stresses is not straightforward. Several empirical relationships have been proposed. The simplest is the life-fraction rule (Equation 1) first suggested by Robinson (13), where t is the time at stress σ_i and t_F is the fracture time at the same stress.

$$\sum_i (t/t_F) = 1 \tag{1}$$

Equation (1) predicts creep damage ω accumulated linearly with time, i.e.,

$$\omega = t/t_F \tag{2}$$

More general nonlinear damage rules, which take into consideration the current state of damage in the material, have been proposed by Kachanov (14) and Bui-Quoc (15), which are given in equations (3) and (4), respectively.

$$\frac{d\omega}{dt} = \left[\frac{\sigma}{(1-\omega)\sigma}\right]^{\nu} \tag{3}$$

$$\frac{d\omega}{dt} = B\sigma^{m}\omega^{c} \tag{4}$$

For a constant stress, the damage accumulated at time t are, according to equations (3) and (4).

$$\omega = 1 - (1 - t/t_F)^{\frac{1}{\nu + 1}} \tag{5}$$

$$\omega = (t/t_F)^{\frac{1}{1-c}} \tag{6}$$

All three empirical fracture criteria predict creep damage to be a function of t/t_F only, independent of the magnitude of the stress. Results on MERL 76, given in Table IX, are at variance with this prediction.

Since MERL 76 fractures by formation of wedge-type cracks at grain boundary triple junctions, a fracture criterion based on accumulation of a critical amount of grain boundary sliding strain, ϵ_{GB}^{c} could be considered more appropriate. A strain criterion for creep rupture can be written as

$$\sum_{i} k_i \Delta\epsilon = \epsilon_{GB}^{c} \tag{7}$$

where k_i is a grain boundary strain partition coefficient and $\Delta\epsilon$ is the plastic strain increment. According to Crossman and Ashby (9) the variation k_i with strain rate is illustrated in Figure 15 for materials which obey power-law creep and with stress exponents n of 4.4 (aluminum) and 16 (MERL 76). In Figure 15 $\dot{\gamma}$ is the applied shear strain rate and $\dot{\gamma}_T$ is the transition strain rate, which is a function of microstructural parameters and grain boundary diffusivity (9). For both materials, the contributions of grain boundary sliding decreases rapidly with increasing strain rate. The maximum grain boundary sliding contribution in MERL 76 is about 0.4 of the total plastic strain and occurs when the ratio of the deformation ratio to the transition strain rate is less than about 0.05. Under varying stresses or strain rates, equation (7) can be written as

$$\epsilon_{GB}^{c} = \int_{0}^{t_F} f(\dot{\epsilon}/\dot{\epsilon}_T)\dot{\epsilon}\,dt \tag{8}$$

where the partition coefficient k_i is expressed as a function of the deformation rate and the transition strain rate. Application of this strain criterion to the stress decrement and increment creep data from the present study has not been successful since no constant ϵ_{GB}^{c} was obtained over a range of $\dot{\epsilon}_T$ values*, 10^{-3} to 10^{-6} h^{-1}. The term $f\ (\dot{\epsilon}\ /\dot{\epsilon}_T\ )$ was approximated by 0.4 sech $(0.2\ \dot{\epsilon}\ /\dot{\epsilon}_T\ )$ in our calculations. Further, the calculations showed that greater damage should accumulate at lower stress which is contrary to our observations (Table IX). Again we conclude that our results are not consistent with this formulation.

The failure of both the stress and the strain fracture criteria are not entirely unexpected if one considers mechanistic aspects of fracture. The formation of wedge-type cracks during creep suggests that the fracture involves a combination of several processes including nucleation and growth of cavities at carbide particles in the grain boundaries, and grain boundary sliding. At high stresses (high deformation rates) when grain boundary sliding contribution is negligible, fracture may predominantly consist of nucleation of cavities at grain boundary carbide particles and growth of these cavities. Thus, the rupture is governed by the magnitude of the applied stress and time. At lower stresses (lower deformation rates) the onset of fracture may be determined by the accumulation of a critical amount of grain boundary sliding. The fracture criterion in this case involves both strain and strain rate. Therefore, the fracture criterion in general, should include stress, strain, and strain rate, not simply stress or strain. Such a general criterion has not yet been developed either empirically or mechanistically, although several fracture cases have been individually studied theoretically (16).

In the absence of an adequate fracture criterion, it is still of interest to examine the applicability of the simple life-fraction rule under restricted conditions: fixed temperature, fixed loading sequence, and narrow stress range as in our stress relaxation tests. An outline of the analysis is given in the Appendix. Table X shows results of this calculation. For Specimen 144, which had a smaller prior tensile strain, a smaller life-fraction at fracture (0.498) was used in order to obtain agreement between the calculated life and the actual life. However, use of this life fraction would predict Specimen 143 to have failed at a prior tensile strain of 0.04, which is contrary to our data. On the other hand, a considerably larger life fraction (1.104) was necessary to obtain agreement with actual fracture life for Specimen 143. In this case, the predicted life for Specimen 144 is larger than the actual life by 14 orders of magnitude (Note that the use of the nonlinear damage rules, equations (3) and (4), would give exactly the same results when the damage parameters are set equal to the life fractions). The basic reason for the failure of the life-fraction rule in this case is that it assumes implicitly that the same damage processes operate during the tensile straining and relaxation. In view of the preceding discussion this seems to be a gross oversimplification. It is likely that the damage introduced during tensile straining and relaxation are different. In fact, the strong loading sequence effect that we observed (Table IX) seems to confirm this suggestion. Therefore, to treat the relaxation rupture phenomenon realistically, different fracture criteria should be used for different segments of the test. For this reason, a damage partitioning concept is introduced, which is outlined below.

---

* Calculated value of $\dot{\epsilon}_T$ for the OQ material is of the order 10^{-5} h^{-1}

For simplicity, the life-fraction rule is used to illustrate the formulation of the damage partitioning concept. Let the life-fraction be given by J in "tensile fracture" at low strain rates, i.e.,

$$\sum_i (t/t_F)_i = J \tag{9}$$

The value of J can be calculated if the tensile flow stress versus time curve and the variations of creep rupture times at constant stresses, t_F, are known. Let the life fraction for relaxation fracture with negligible tensile damage be given by K, i.e.,

$$\sum_i (t/t_F)_i = K \tag{10}$$

In contrast to J, the value of K cannot be determined experimentally since the relaxation rupture time with negligible tensile damage (high tensile strain rate and small tensile strain) is unrealistically long. Thus, K may be regarded as an adjustable parameter. To calculate the relaxation fracture from stresses above the yield points, the interaction of the tensile damage with that produced during relaxation must be considered and may be the key to the success of this approach. Since this interaction results in a reduction of the relaxation rupture time, a simplistic way of treating this interaction is to reduce the value of K in equation (10) by an amount proportional to the prior tensile damage. Thus, equation (10) is modified to

$$\sum_i (t/t_F)_i = \left(\frac{J-l}{J}\right)^M K \tag{11}$$

where l is the tensile damage which can be calculated by the first integral of equation (A8); and M is a constant. Since (J-l)/J is less than unity, the magnitude of M is a measure of the severity of the interaction between the prior tensile damage and that produced during stress relaxation.

Results of the calculation using the preceding damage partitioning procedure are given in the last column of Table X. The values of J and K chosen for this calculation are 1.6 and 0.6, respectively, which are based on the results of the incremental and decremental creep tests (Table IX); M=5.0 was used. With these values of J, K, and M, the calculated values are about 1 order of magnitude different from the actual fracture lives. Better agreement can be obtained by choosing a different set of J, K, and M values, however good agreement does not necessarily indicate infallibility of the underlying concept because of the limited data available for comparison. Instead, the purpose of this calculation is to show that, possibly because of the nonadditivity of the damage accumulated during tensile straining and relaxation, use of a different fracture criterion for each stage of the test yields a far better prediction than that from a single criterion. Applying the calculation to the case where a faster tensile strain rate of 0.10 min^{-1} is used; no short relaxation rupture times (less than 5h) are predicted until a prior tensile strain of 0.19 is reached, which is in agreement with Hill's experimental data (10). Thus we conclude that our analysis of the relaxation fracture behavior is substantially more realistic. The calculated relaxation rupture times of the OQ material using the preceding set of values for J, K, and M, except as noted, are given in column 3 of Table XI. An interesting feature of the relaxation fracture behavior is the transition from short lives (less than 10h) to very long lives (10^3 h) which occurs at a prior tensile strain of about 0.04. Further, the stress dependence of relaxation rupture time is considerably lower at low lives compared with that at long lives. This relaxation fracture behavior is not changed by using different values of J, K, and M although the magnitude of the predicted fracture life is rather sensitive to variations of these parameters. For example, if one decreases the value of M to 4 i.e., reducing the detriment of the tensile damage to subsequent relaxation fracture, the rupture life at a prior tensile strain of 0.04 increases by a factor of 35 (Table XI, fourth column). Also, the life transition is shifted to a slightly higher stress. Increasing the value of J, i.e., increasing the tensile ductility has similar effects as reducing M (Table XI, last column). Further, since the relaxation fracture life is rather sensitive to values of J, K, and M, especially near the life transition, it is conceivable that a slight scatter in material properties between specimens could cause a large scatter in relaxation fracture lives.

In the following we shall attempt to use the analysis of relaxation fracture behavior to rationalize three interesting notch-rupture features in the OQ MERL 76 which are: (1) The occurrence of a threshold stress level below which notch lives are long and approach those of smooth specimens (Figure 10). Above the threshold level and at high net-section stresses the notch lives are low and decrease slowly with increasing stresses. Notch lives at these stresses can be approximated by a power law with a stress exponent of about 3. (3) At stresses near the threshold, large scatter in notch lives (up to two orders of magnitude) is frequently observed (see Table V) which cannot be attributed either to chemical and microstructural inhomogeneities which are nonexistent in the P/M product or to the presence of pre-existing flaws (although nonmetallic inclusions can reduce notch-rupture lives when present).

Turning to notch-rupture failure, we postulate that crack nucleation occurs in a small volume of material at the notch root in a similar manner to relaxation fracture. Thus at large stresses where the relaxation fracture times are short, the crack nucleation times at the notch are correspondingly short. In these cases the notch life is determined by crack propagation. The initial propagation of the notch crack under multiaxial stresses is quite complicated and has not been analyzed in any detail. From limited measurements made in the first-year program, it is believed that the stress dependence of the notch crack propagation rates is similar to that from creep crack growth specimens. These rates over a range of stress intensities, can be approximated by a power law with a stress exponent of about 4 (2), and we note the very similar stress dependence of the notch lives at high net-section stresses. At stresses around the transition point, the relaxation fracture lives are predicted to vary be several orders of magnitude by small changes in the parameters M and J (Table XI). Similarly, the crack nucleation lives at notches may be expected to show the same trend due to slight variation of material properties between specimens, which could account for the observed scatter in notch lives near the threshold stress. At stresses below the threshold, the damage accumulated at the notch root during loading and subsequent relaxation is too small to result in rapid crack nucleation. In this case, the notch-rupture processes are thought to be similar to those in smooth rupture, as evidenced by similar rupture lives and stress dependence, resulting in an abrupt increase in notch lives. As the external stress increases on a notched specimen, the notch root will deform elastically until local plasticity occurs. We could anticipate that the transition stress would correspond to a notch strain of about 0.04. Finite element analysis conducted by Hill (10) has shown that the calculated strain is lower (0.01) at the transition although the local stress level (≈1220 MPa) is very close to those measured in relaxation tests.

From the above discussion, it becomes obvious that one basic cause for the relaxation fracture under uniaxial stress and, by association, the notch brittleness of the OQ material, is the high tensile strength. This, according to phenomenological cumulative damage fracture criteria, will result in more damage for a constant amount of strain than the AC material, which has a lower tensile strength. Important assumptions implicit in this phenomenological approach are:(1) the rates of damage formation are independent of microstructural parameters of the materials and (2) the damage tolerances of the materials are the same, i.e., the same fracture criterion can be applied to both the AC and the OQ materials. The use of these assumptions can be justified only as an analytical convenience. In fact, experimental evidence (Table IX) has shown that the fracture criteria for the AC and the OQ materials under varying stresses are not the same. At high stresses the AC material exhibited a slightly larger life sum than the OQ material, implying a slower rate of damage accumulation and/or a higher damage tolerance in the AC material.

The above discussion has ignored at least two other critical factors in notch sensitivity. Another contributing factor to the relaxation-fracture and notch-rupture behavior differences between the AC and the OQ materials is probably of microstructural origin. Differences in grain boundary microstructures which are obvious in Figure 9 control the detailed mechanics of grain boundary fractures and displacements which will control fracture behavior.

The observation that the notch life of the OQ material significantly increased when the initial stage of the test was conducted in a vacuum or when the notch was shot-peened shows the critical nature of the specimen's environment interface. These results show that the metallurgical conditions and the test conditions are intimately related to the damage accumulation processes.

Finally, it is suggested that an experimental approach to define the local fracture conditions at grain boundaries should be established. In polycrystalline material such local conditions cannot be investigated, and therefore, more anisotopic structures are needed. A directionally recrystallized structure would seem ideal, for with but one (general) grain boundary orientation, local conditions (stresses, displacements, etc.) could be monitored. Various structural conditions could be produced by heat treatment, and the effect of test environment could also be studied. Such experiments were beyond the scope of the present study but would appear to be one of the few methods of gaining more detailed insight into the fracture processes.

In summary, the second-year program established systematically the influence of a large number of variables on the notch-rupture behavior of MERL 76. Some ancillary tests on smooth section showed that short rupture lives under relaxation conditions paralleled notch-rupture sensitivity. Based on this commonality, several failure criteria were tested to see if the results could be rationalized, but all were found inadequate. A preliminary partitioning method was proposed which simulated the results more closely. However, we conclude that much remains to be learned about structural and environmental influences before any satisfactory model can be attempted.

3.4.5 Conclusions

The major conclusions that can be drawn from the work performed in the second year of this program are as follows:

1. Characterization of -325 mesh MERL 76 powder revealed several structural features typical of rather rapid cooling. Higher concentrations of interstitial elements were measured for the fine powder compared with the more typically used -80 mesh fraction. These higher levels did not alter the consolidation or grain growth behavior of the material.

2. Mechanical properties determined on HIP consolidated -325 and -80 mesh material revealed no significant differences. HIP above the γ' solvus resulted in a coarser grain size and superior stress rupture capability. In all stress-rupture testing, some scatter in notch properties was found at high stress levels.

3. The notch stress-rupture properties of two conditions of MERL 76 were shown to be a function of microstructure. Quenching from a low solution treatment temperature gave straight grain boundaries, containing a low concentration of precipitates, and resulted in a notch brittle condition. Air cooling gave more heavily decorated boundaries and a structure that exhibits much less notch sensitivity.

4. A large number of factors were shown to influence rupture behavior in the notch-brittle material. The life could be increased at one test temperature by the following methods:

   o Elimination of the air environment during test. Performing only the first part of a test in a vacuum produced a similar life improvement.

   o Shot peening the notch surface

   o Preloading at lower temperatures before increasing to the test temperature.

   o Rapid loading rates

5. Stress relaxation tests on smooth specimens, at initial stresses above the yield, duplicated the notch life differences between the two materials. Thus, "notch-brittle" MERL 76 failed after short times with low ductility; the more 'notch-ductile' material did not fail.

6. Analysis of fractures in stress relaxation tests based on accumulation, either linearly or nonlinearly, of a critical amount of damage failed to predict the experimental results. A partitioning concept which takes into consideration dissimilar types of damage and allows for their interaction was proposed and shown to better describe fractures in stress relaxation. Results of this analysis were also used to rationalize several notch-rupture features of MERL 76 observed in the present studies.

APPENDIX

Procedure for Calculation of Rupture Time During Uniaxial Stress Relaxation

Over a limited stress range, the stress dependence of creep-rupture time t_F can be expressed as (see Figure 10).

$$t_f = D\sigma^{-m} \tag{A1}$$

Where D and m are constants. Substituting (A1) into equation (1) results in

$$\frac{1}{D}\sum_i t_i \sigma_i^{m} = 1 \tag{A2}$$

For continuously varying stresses (A2) can be written as

$$\frac{1}{D}\int_0^{t_R} \sigma^{m}(t)\,dt = 1 \tag{A3}$$

For MERL 76 the variation of tensile flow stress with time can be expressed as (see Figure A1)

$$\sigma = a + bt \tag{A4}$$

Where a and b are constants. Stress relaxation at constant total strain is described by the differential equation

$$\dot{\epsilon}_p = -\dot{\sigma}/E \tag{A5}$$

Where E is the elastic modulus and $\dot{\epsilon}_p$ is the rate of plastic deformation during stress relaxation. At 704°C the stress dependence of $\dot{\epsilon}_p$ can be approximated by that of the secondary creep rate $\dot{\epsilon}_s$ (see footnote) which can be expressed as a power law

$$\dot{\epsilon}_p \sim \dot{\epsilon}_s = C\sigma^{n} \tag{A6}$$

Where C and n are constants. Substituting (A6) into (A5) and after integrating, find

$$\sigma = \left[\sigma_0^{1-n} + CE(n-1)t\right]^{\frac{1}{1-n}} \tag{A7}$$

Where σ_0 is the initial stress. Equation (A7) is plotted against the experimental data in Figure A-2 and the agreement is seen to be good.

Substituting equations (A4) and (A7) into equation (A3), the rupture time t_R during stress relaxation can be calculated by solving the equation

$$\frac{1}{D}\int_{0}^{t_0}(a+bt)^{m}dt + \frac{1}{D}\int_{0}^{t_R}\left[\sigma_0^{1-n}+CE(n-1)t\right]^{\frac{m}{1-n}}dt = 1 \qquad \text{(A8)}$$

Footnote:

One would have expected that $\dot{\epsilon}_p$ would be considerably larger than $\dot{\epsilon}_s$ because of the tertiary creep contribution; however, this is found not to be the case. The reason is that prior tensile deformation hardens the material resulting in a lower secondary creep rate compared with the virgin material. Apparently the reduced secondary creep rate is compensated by the accelerating tertiary creep and results in an overall creep rate which can be approximated by the secondary creep rate of the virgin material.

REFERENCES

1. R. D. Eng and D. J. Evans: Proceedings of the Fourth International Conference on Superalloys, Seven Springs, Pennsylvania, in press, 1980.

2. C. C. Law and M. J. Blackburn: Mat. Trans A, 1980, Vol. 11A, pp 495 - 507.

3. G. B. Heydt: Trans. ASM, Vol. 54, 1961, p. 220.

4. P. R. Swann, F. P. Ford, and A.R.C. Westwood, Ed., "Mechanisms of Environment Sensitive Cracking of Materials," Proc. Int. Conf., Univ. of Surrey, Guildford, April, 1977.

5. D. J. Wilson: Trans. ASME, J. Eng. Mater. Techn., 1975, Vol. 97, p. 223.

6. M. Ohnami and K. Umeda: Bulletin of the JSME, 1976, Vol. 19, No. 136, p. 1100.

7. D. R. Hayhurst, F. A. Leckie, and C. J. Morrison: Proc. R. Soc. Lond. A., 1978, Vol. 360, p. 243.

8. B. L. Freeman and G. J. Neate: J. Mater. Sci. Eng., 1978, Vol. 36, p.241.

9. F. W. Crossman and M. F. Ashby, Acta Met., 1975, Vol. 23, p425.

10. J. T. Hill, "Creep-Rupture Damage Accumulation in MERL 76 - Correlation of Smooth Creep-Rupture Data" P&WA report EII 80-639-9014, March 1980.

11. A. E. Johnson, J. Henderson and V. D. Mathur: Aircraft Engineering, 1960, Vol. 32, p. 161.

12. M. M. Abo El Ata, and I. Finnie in "Creep in Structures", Ed J. Hult, pp. 80 - 95, Springer-Verlag, 1972.

13. E. L. Robinson: Trans. ASME, 1952, Vol. 74, pp. 777 - 781.

14. L. M. Kachanov: Izv. Akad. Nauk S.S.S.R. Otd. Tech. Nauk, 1958, No. 8, pp. 26 - 31.

15. T. Bui-Quoc: J. Eng. Mater. & Tech., 1979, Vol. 101, pp. 337 - 343.

16. R. Raj and M. F. Ashby: Acta Met., 1975, Vol. 23, pp. 653 - 666.

TABLE I

OXYGEN AND NITROGEN CONTENTS (ppm) IN -80 MESH AND -325 MESH MERL 76

Material	-80 Mesh		-325 Mesh	
	O	N	O	N
Loose Powder	123	*	175	13
Consolidation	99	13	151	21

* No Data

TABLE II

COMPOSITIONS OF MERL 76 (WEIGHT %)

	-80 Mesh	-325 Mesh
Ni	Bal.	Bal.
Cr	12.3	12.1
Co	17.9	18.1
Mo	3.3	3.2
Al	5.0	5.1
Ti	4.3	4.3
Nb	1.7	1.6
Hf	0.74	0.58
B	0.018	0.020
Zr	0.06	0.07
C	0.025	0.026
O	94 ppm	151 ppm
N	30 ppm	21 ppm

TABLE III

704°C TENSILE PROPERTIES OF -80 MESH AND -325 MESH MERL 76*

Mesh	0.2%YS MPa	UTS MPA	El %	RA %
-80	983.2	1247.1	29.3	40.1
-325	1033.5	1227.1	19.0	22.1

* 1120°C/2 Hr./AC + 760°C/8 Hr./AC.

TABLE IV

704°C STRESS-RUPTURE PROPERTIES OF -80 MESH AND -325 MESH MERL 76*

	-80 Mesh				-325 Mesh			
Stress MPa	Life Hr.	El %	RA %	Notch Life Hr.	Life Hr.	El %	RA %	Notch Life Hr.
550	488.7	13.0	14.1	375.0	390.6	4.1	5.8	175.3
					523.8	4.1	5.6	198.3
655	253.3	9.7	12.3	120.0	208.2	2.9	5.0	110.0
					206.9	4.6	6.1	129.3
758	115.0	11.0	15.8	23.5	86.7	7.2	10.3	4.9
	100.9	10.2	12.0		82.7	6.7	11.6	73.5
860	24.8	16.1	20.9	4.9	25.1	8.7	13.9	50.5
				9.0	24.3	7.6	13.0	22.7

* HT: 1120°C/2 Hr./AC + 760°C/8 Hr./AC

TABLE V

EFFECT OF GRAIN SIZE ON 704°C STRESS-RUPTURE PROPERTIES OF -325 MESH MERL 76

	Grain Size 12µm				Grain Size 24µm			
Stress MPa	Life Hr.	El %	RA %	Notch Life Hr.	Life Hr.	El %	RA %	Notch Life Hr.
550	450.6	3.9	5.2	213.9	1030.0	1.7	1.9	842.4
	498.4	4.7	7.0	192.3	1130.6	1.2	-	1000.5 +
655	184.9 +	*	*	120.0	547.9	7.3	10.8	598.6
	229.3	8.7	9.4	110.0	537.6	7.6	12.4	518.0
758	64.8	4.7	6.2	69.5	161.5	8.9	17.0	345.2
	83.8	8.7	9.9	6.3	198.7	9.1	10.6	6.2
860	26.0	9.0	13.5	0.3	33.9	11.5	14.7	3.1
				4.2	41.2	7.8	11.7	152.1

HT: 1163°C/2 Hr./Furnace Cool To 1130°C/OQ
+ 870°C/0.7 Hr./AC + 980°C/0.8 Hr./AC
+ 650°C/24 Hr./AC + 760°C/8 Hr./AC

+ Test terminated with no failure

* Thread failure

TABLE VI

EFFECT OF SURFACE TREATMENT ON NOTCH-RUPTURE LIFE

Surface Treatment	Life, h
As-machined	2.3
As-machined	2.1
Electropolished	0.5
Electropolished + N_2^+ Implanted	0.6
Electropolished + N_2^+ Implanted	1.5
As-machined + Prestrained	
827 MPa at 20°C	0.5
690 MPa at 370°C	1.7
As-machined + Peened (6.5N)	113.0*
As-machined + Peened (11.5N)	95.0*

*Test terminated with no failure

TABLE VII

EFFECT OF TEST ENVIRONMENT ON NOTCH-RUPTURE LIFE

Environment	Life, h
Air	2.3
Air	2.1
Vacuum, 10^{-5} Torr	178.5*
Vacuum, 10^{-5} Torr	559.0*
Tested 6 h in vacuum followed by air test	104.5*

*Test terminated with no failure

TABLE VIII

STRESS RELAXATION RUPTURE TIME AT 704°C, TENSILE STRAIN RATE = 0.01 MIN^{-1}

Specimen No.	Initial Stress, MPa	Prior Tensile Strain	Rupture Time h
153	861.3	0.000	50.0 +
141	1096.4	0.0012	60.0 +
144	1226.5	0.038	0.263
148	1231.4	0.061	0.077

TABLE IX

CREEP RUPTURE OF MERL 76 UNDER VARYING STRESSES AT 704°C

Stress MPa	Life Fraction, t/t_F				
	Spec. 238+	Spec. 233	Spec. 234	Spec. 237	Spec. 240
1102	(1)* 0.29	(1) 0.30	(1) 0.30	(4) 0.76	-
1034	-	-	-	(3) 0.25	(1) 0.25
999	(2) 0.28	(2) 0.30	(2) 0.30	-	-
965	-	-	-	(2) 0.25	(2) 0.25
896	(3) 0.24	(3) 0.06	(3) 0.25	(1) 0.25	(3) 0.89
$\sum_i (t/t_F)i$	0.71	0.66	0.66	1.51	1.39

* Numbers in parentheses indicate sequence of stress application.

+ All specimens, except No. 238, were machined from the OQ material. Specimen 238 was machined from the AC material.

TABLE X

CALCULATED RELAXATION FRACTURE TIME

Specimen No.	Prior Tensile Strain	Obsv. Fracture Time, h	Calculated Fracture Time, h		
			$\Sigma(t/t_F)$ = 0.498	$\Sigma(t/t_F)$ = 1.104	Damage Partitioning
144	0.038	0.263	0.263	2.98 x 10^{13}	5.102
143	0.061	0.077	*	0.078	0.003

*Fracture during tensile straining

TABLE XI

CALCULATED STRESS RELAXATION RUPTURE TIME OF THE SQ MERL 76 AT 704°C, TENSILE STRAIN RATE = 0.01 MIN^{-1}

Initial Stress, MPa	Prior Tensile Strain	Rupture Time, h		
		M = 5	M = 4	J = 1.9
1223.4	0.02	1.02×10^{6}	1.63×10^{7}	1.08×10^{7}
1225.4	0.03	8.04×10^{2}	2.74×10^{4}	1.89×10^{4}
1227.3	0.04	2.25	7.85×10^{1}	6.53×10^{1}
1229.3	0.05	3.45×10^{-2}	6.07×10^{-1}	6.59×10^{-1}
1231.3	0.06	2.45×10^{-3}	1.76×10^{-2}	2.38×10^{-2}

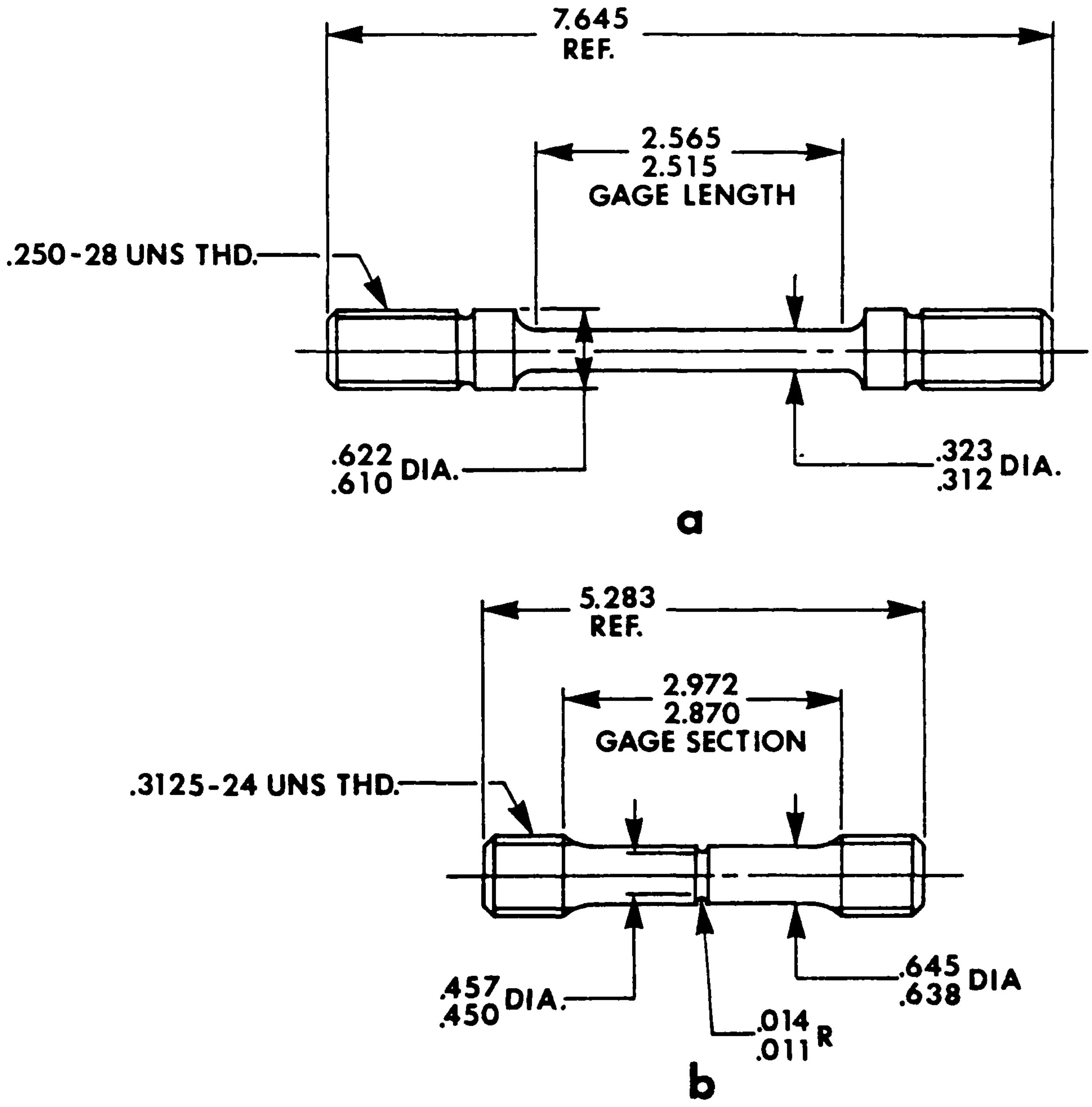
7.645
REF.
2.565
2.515
GAGE LENGTH
.250-28 UNS THD.
.622
.610 DIA.
.323
.312 DIA.
a
5.283
REF.
2.972
2.870
GAGE SECTION
.3125-24 UNS THD.
.457
.450 DIA.
.645
.638 DIA
.014
.011 R
b

Figure 1. Dimensions of (a) creep-rupture specimen
(b) notch-rupture specimen, in cm.

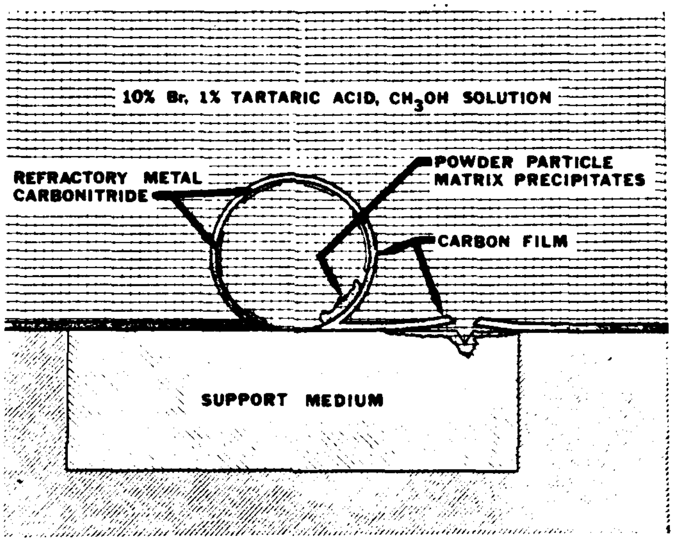
10% Br, 1% TARTARIC ACID, CH_3OH SOLUTION
REFRACTORY METAL CARBONITRIDE
POWDER PARTICLE MATRIX PRECIPITATES
CARBON FILM
SUPPORT MEDIUM

Figure 2. Schematic illustration of a powder particle extraction replica technique (courtesy of P. Genereux).

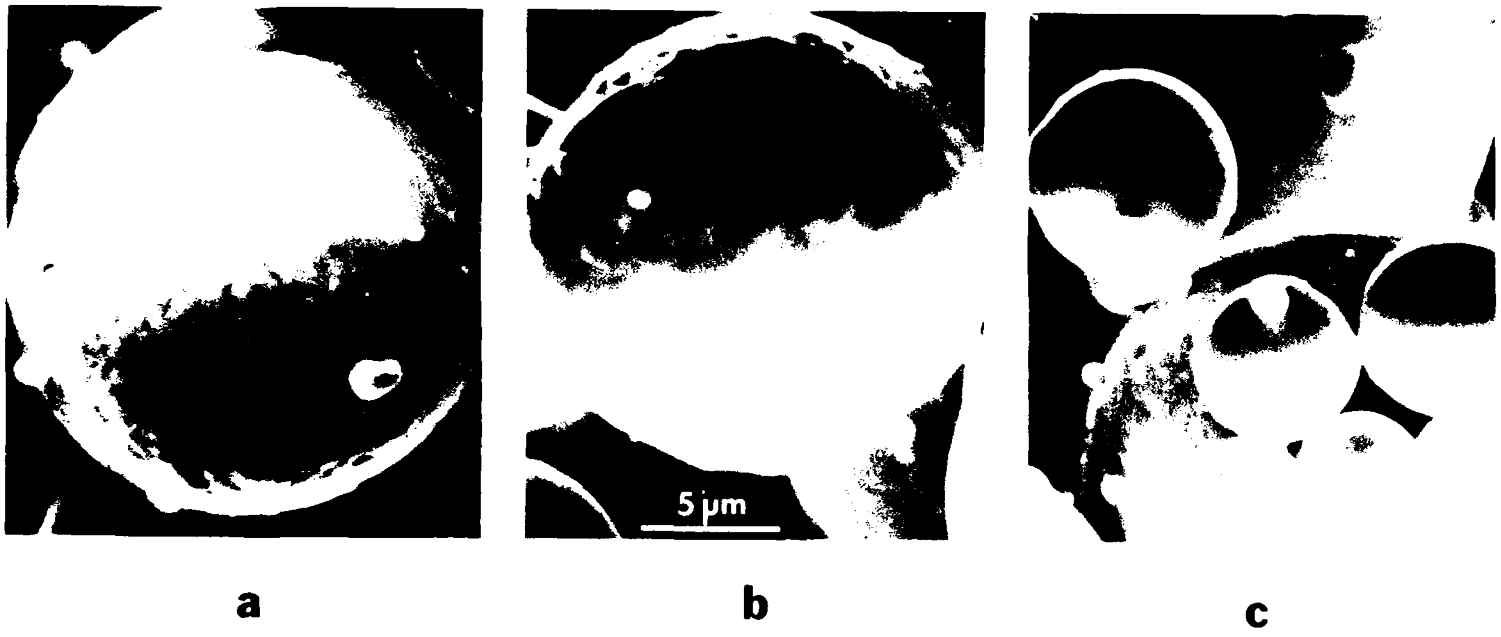

Figure 3. Surface morphologies of the -325 mesh MERL 76 powder particles (a) dendritic (b) granular (c) featureless.

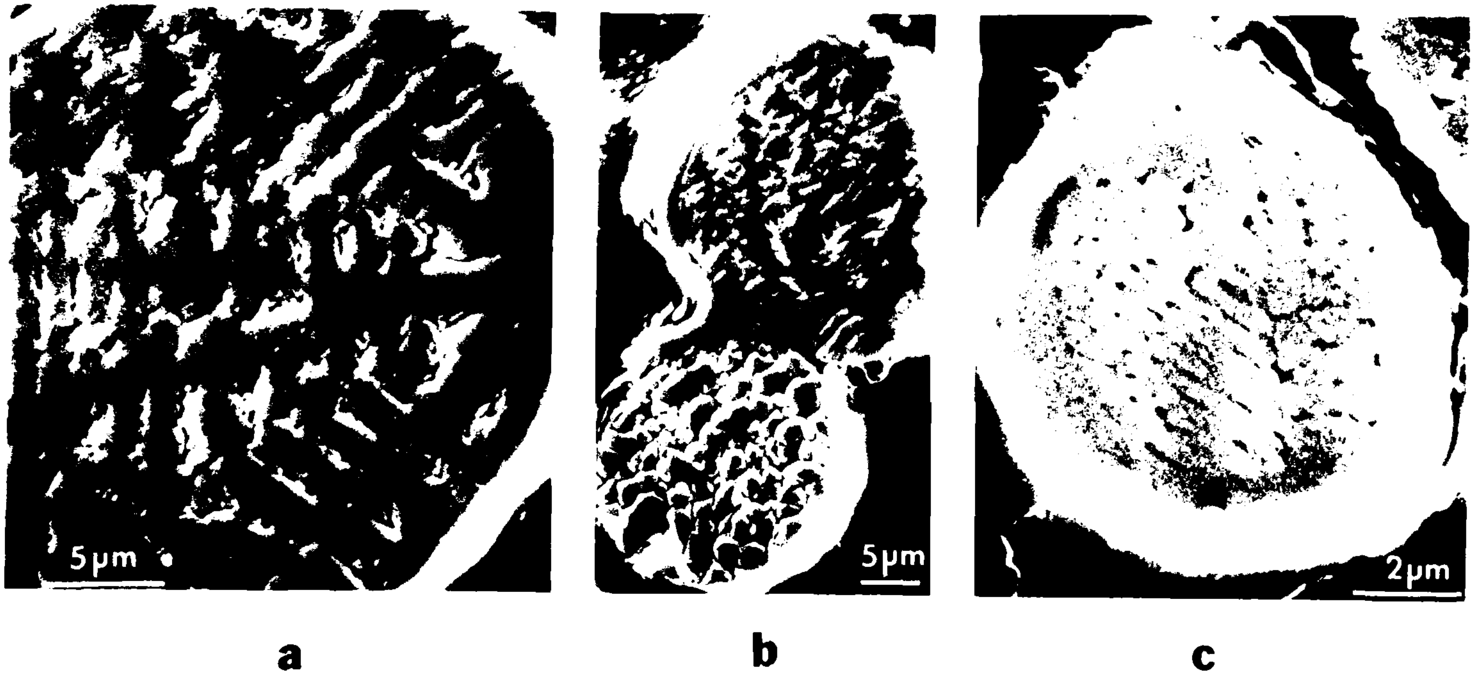

Figure 4. Microstructures of the -325 mesh MERL 76 powder particles (a) dendritic (b) bottom particle - granular, top particle - a mixed granular and dendritic (c) a mixed granular and dendritic core surrounded by a segregation-free surface layer.

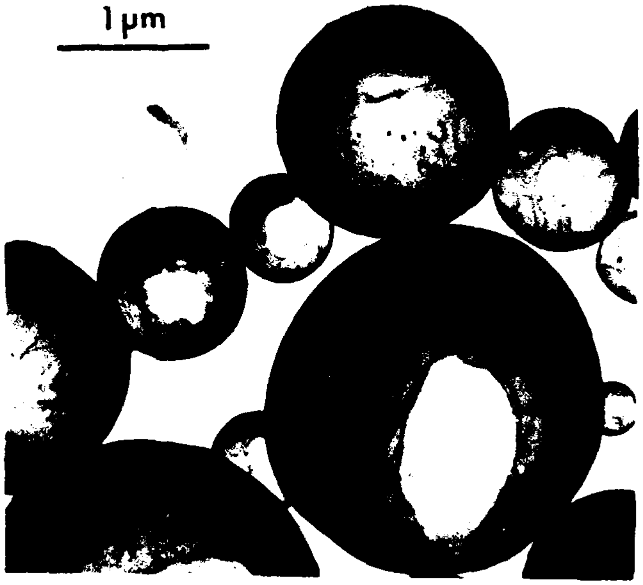

Figure 5. Extraction replica from the -325 mesh MERL 76 powder particles showing a small number of equiaxed particles extracted from the surfaces of the powder particles. The light regions within the spheres are areas where the replica are in contact with the substrate.

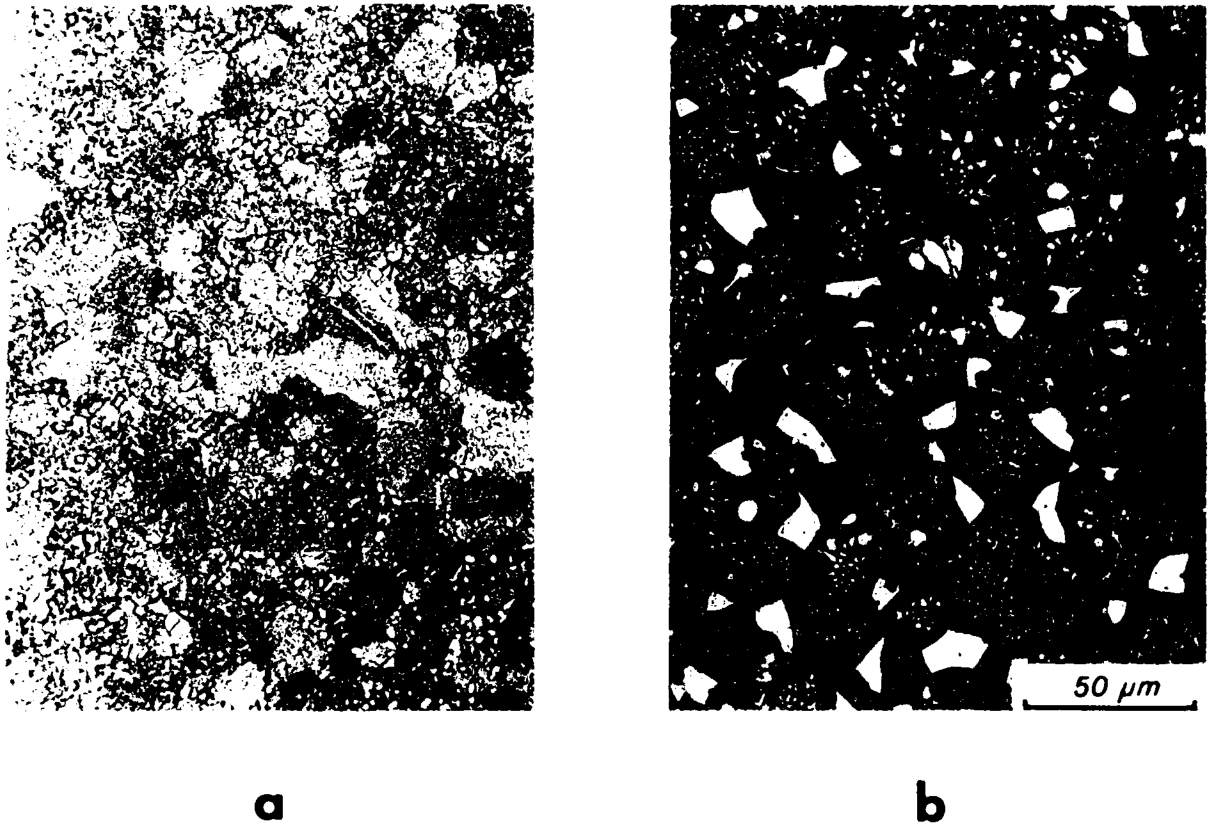

Figure 6. Microstructures of MERL 76 consolidated from (a) -325 mesh powder (b) -80 mesh powder.

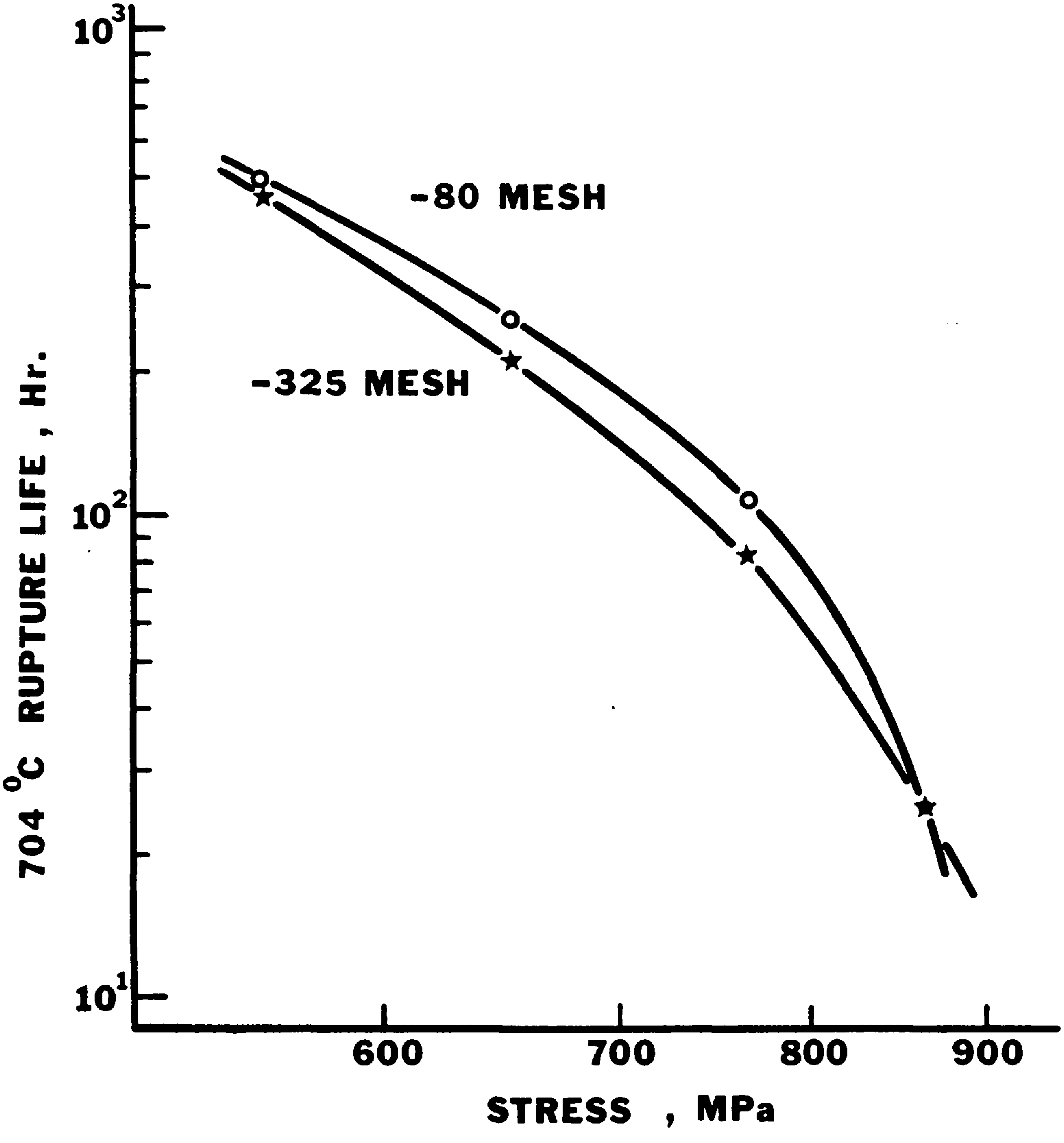

Figure 7. Stress-rupture lives of smooth (K_t=1) MERL 76 specimens at 704°C. The materials were HIP-consolidated from -80 mesh and -325 mesh powders at 1177°C. Heat treatment: 1120°C/2 Hr./AC + 760°C/8 Hr./AC.

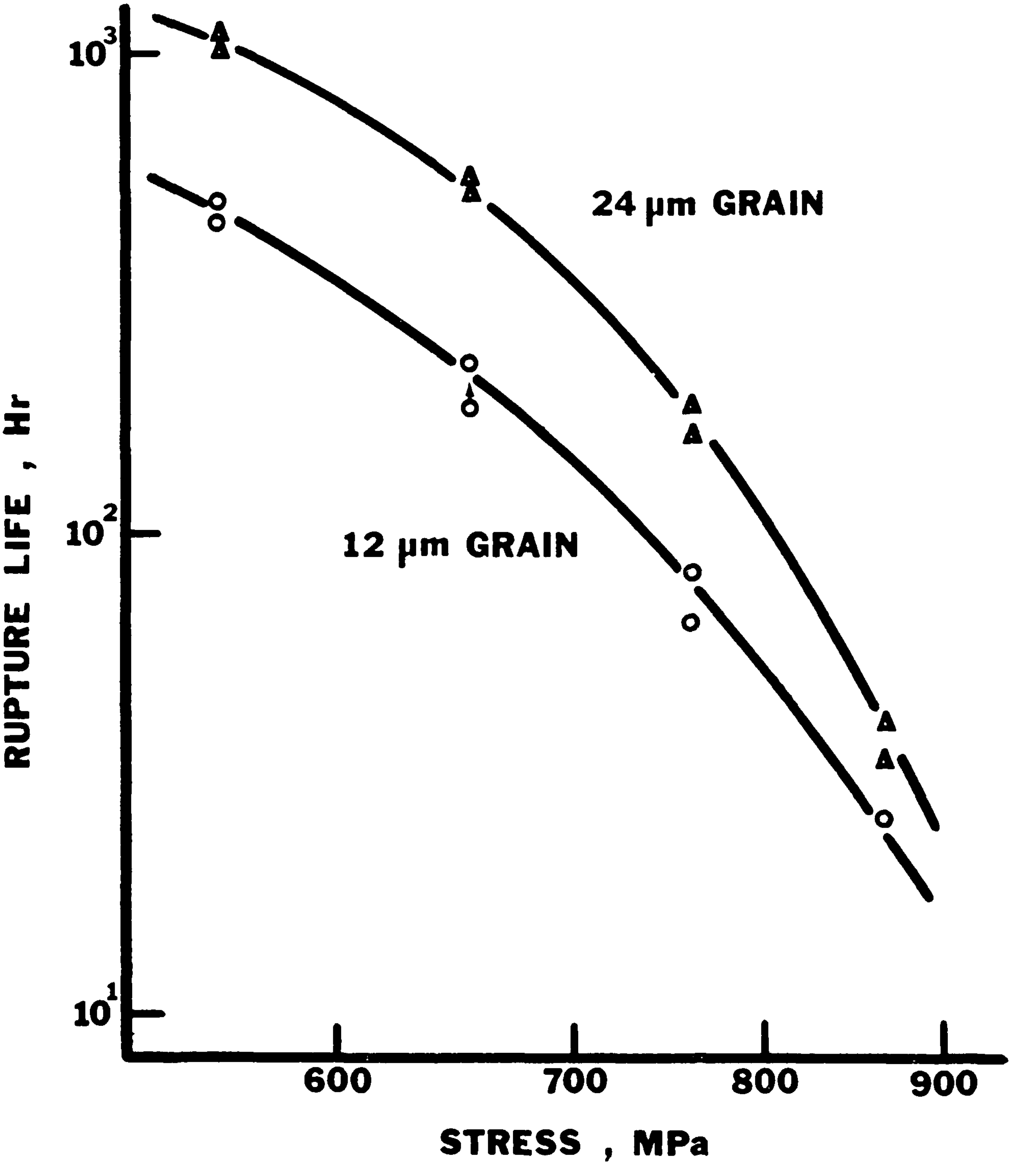

Figure 8. Stress-rupture lives of smooth (K_t=1) MERL 76 specimens at 704°C. The materials were HIP-consolidated from -325 mesh powder at 1177°C and at 1195°C which resulted in grain sizes of 12 μm and 24 μm, respectively. Heat treatment: 1163°C/2 Hr./Furnace Cooled to 1130°C/OQ + 870°C/40 min./AC + 980°C/45 min./AC + 650°C/24 Hr./AC + 760°C/8 Hr./AC.

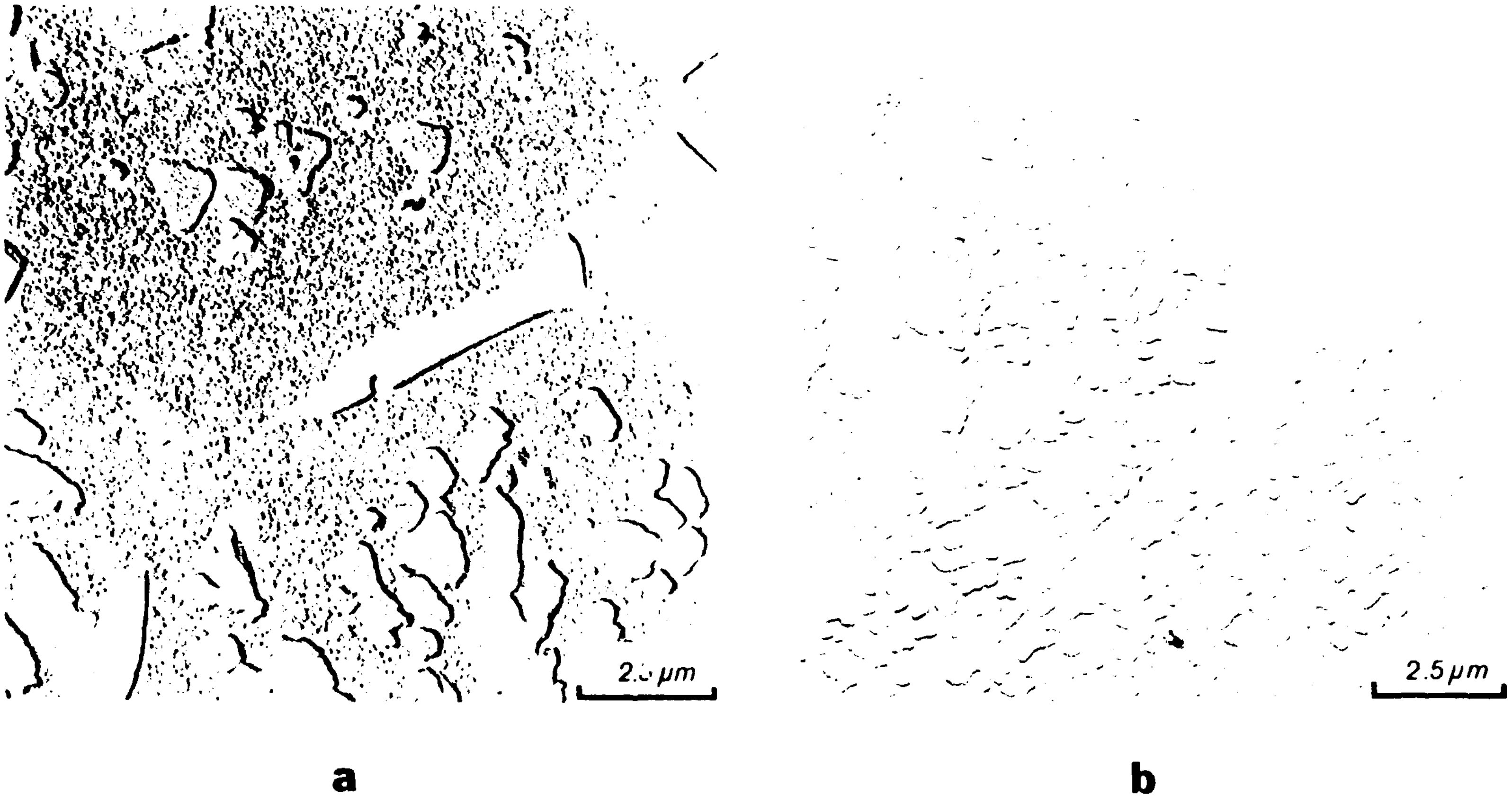
2.5 μm
2.5 μm
a
b

Figure 9 Microstructure of MERL 76 after (a) the OQ (b) AC heat treatments.

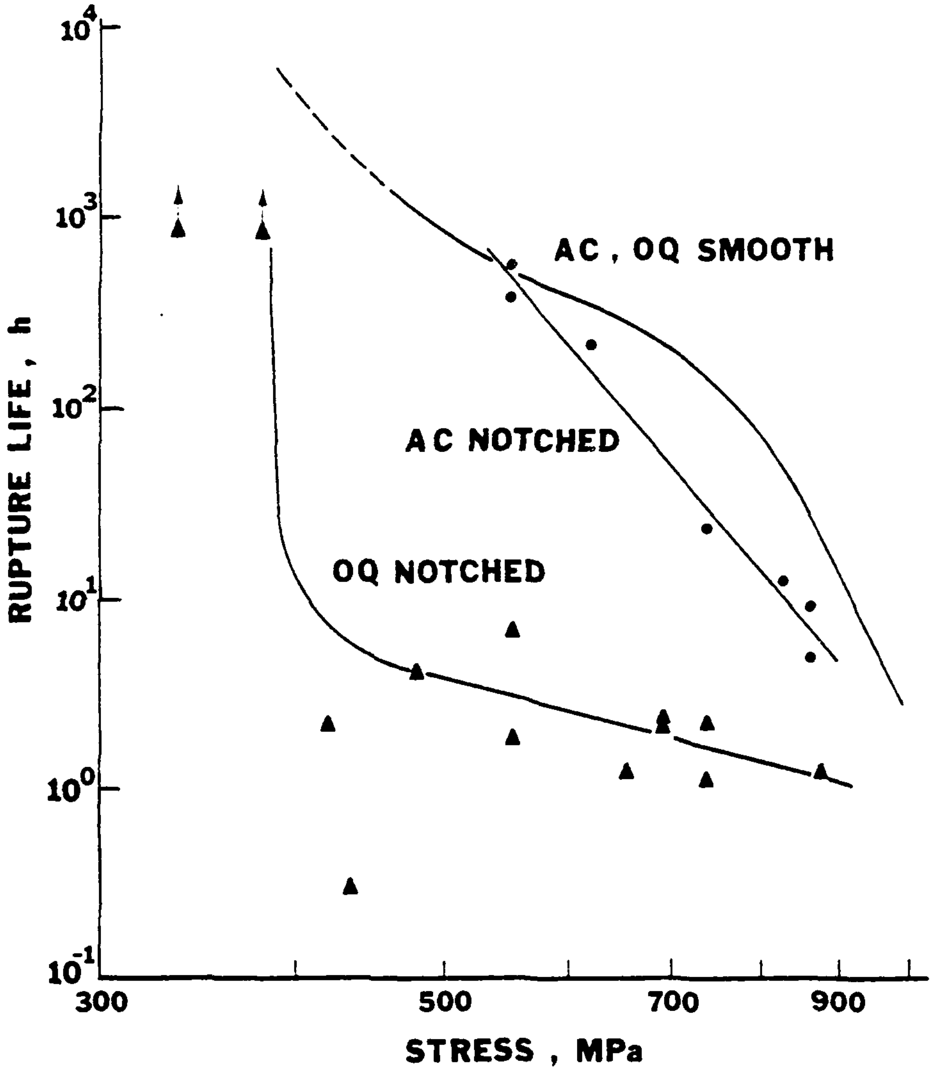

Figure 10 Effect of stress on 704°C rupture lives of smooth (K_t=1) and notched specimens with the OQ and the AC heat treatments.

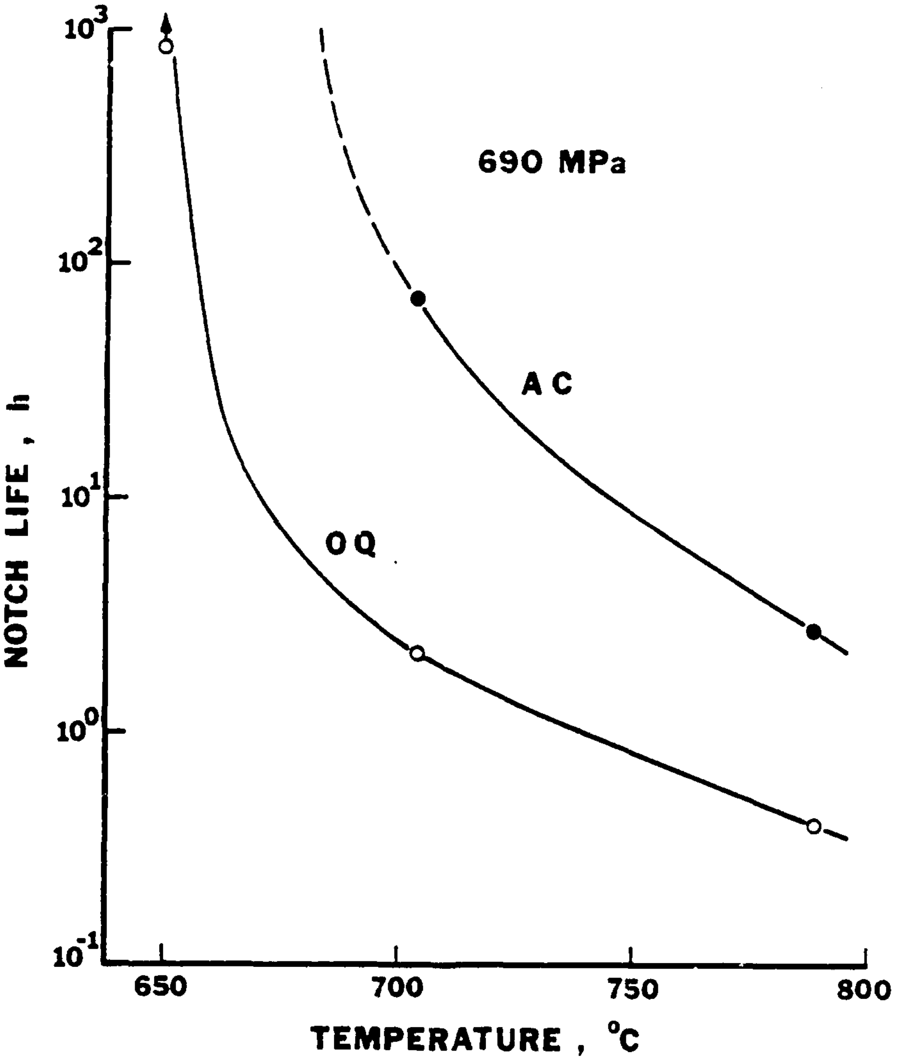

Figure 11 Effect of temperature on rupture lives of notched specimens with the OQ and the AC heat treatments at a net-section stress of 690 MPa.

AD-A086 697 PRATT AND WHITNEY AIRCRAFT GROUP WEST PALM BEACH FL G--ETC F/G 11/6
PLASTIC FLOW AND FRACTURE PROCESSES IN POWDER METALLURGICAL NIC--ETC(U)
FEB 80 C C LAW, M J BLACKBURN F49620-77-C-0083
UNCLASSIFIED PWA-FR-13317 AFOSR-TR-80-0468 NL

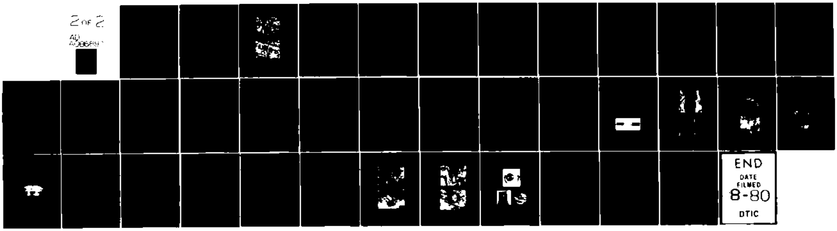

2 OF 2
AD
A086697

END
DATE
FILMED
8-80
DTIC

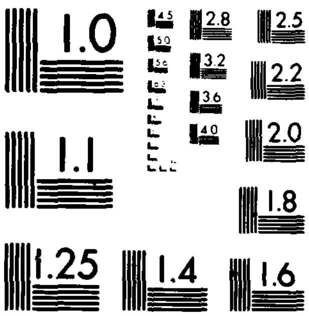
1.0
4.5
5.0
5.6
6.3
2.8
3.2
3.6
4.0
2.5
2.2
2.0
1.1
1.8
1.25
1.4
1.6

MICROCOPY RESOLUTION TEST CHART
NATIONAL BUREAU OF STANDARDS-1963-A

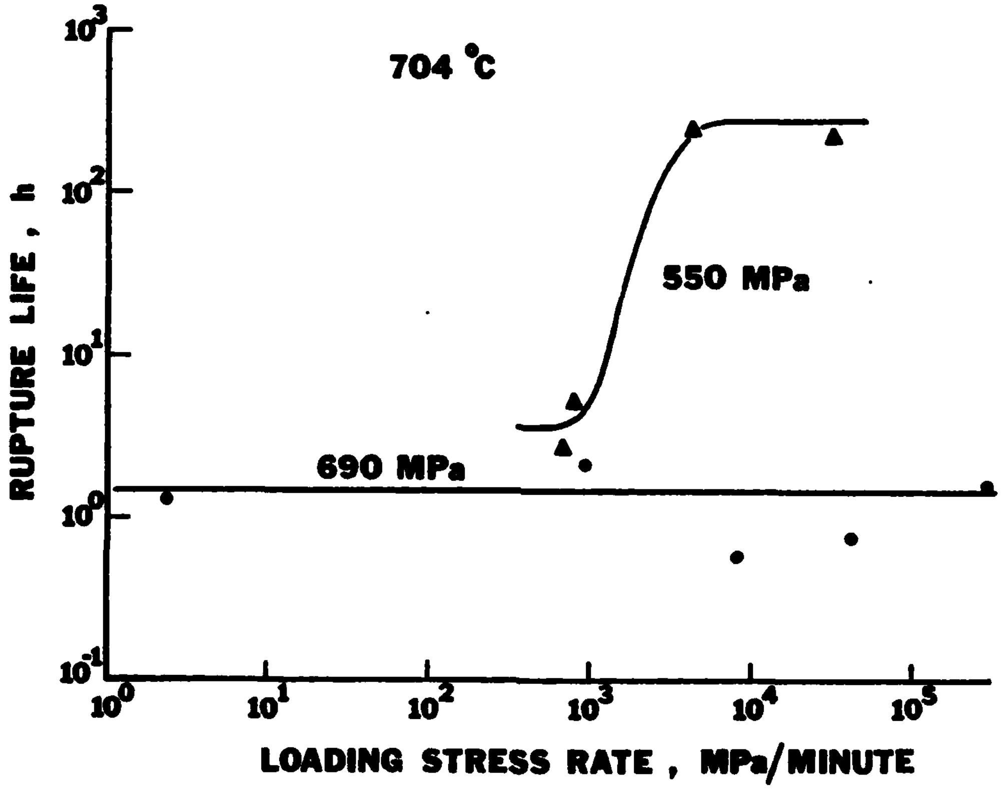

Figure 12 Effect of loading rate on 704°C rupture lives of notched specimens with the OQ heat treatment at net-section stresses of 550 MPa and 690 MPa.

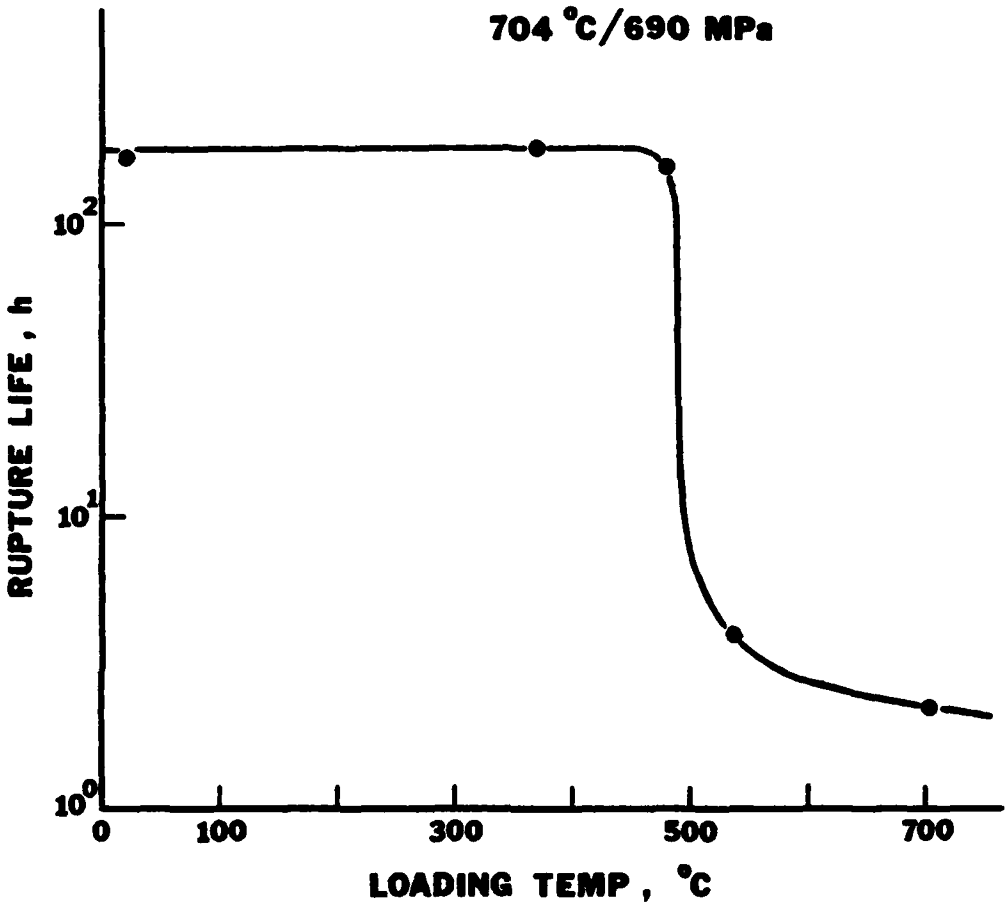

Figure 13 Effect of loading temperature on 704°C rupture lives of notched specimens with the OQ heat treatment at a net-section stress of 690 MPa.

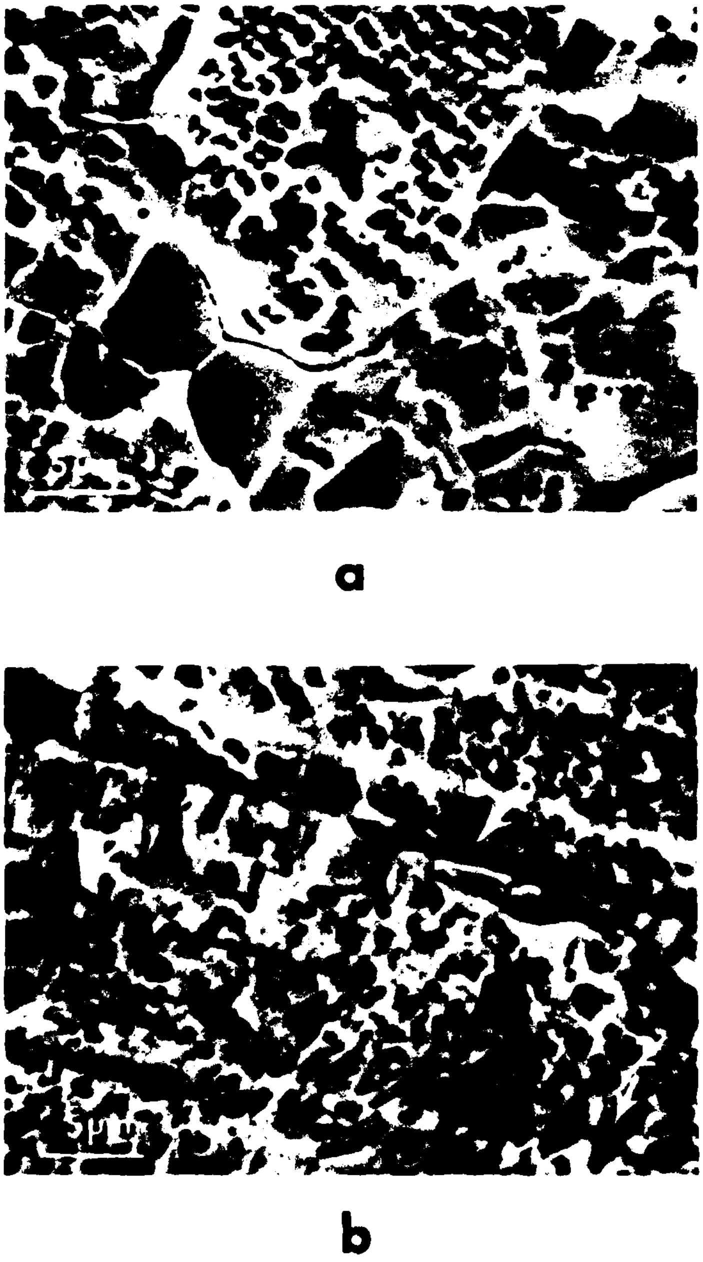

Figure 14 Microcracks observed in the notch root during tests at 704°C/690 MPa in a vacuum (a) the OQ specimen after 65.5h (b) the AC specimen after 111h.

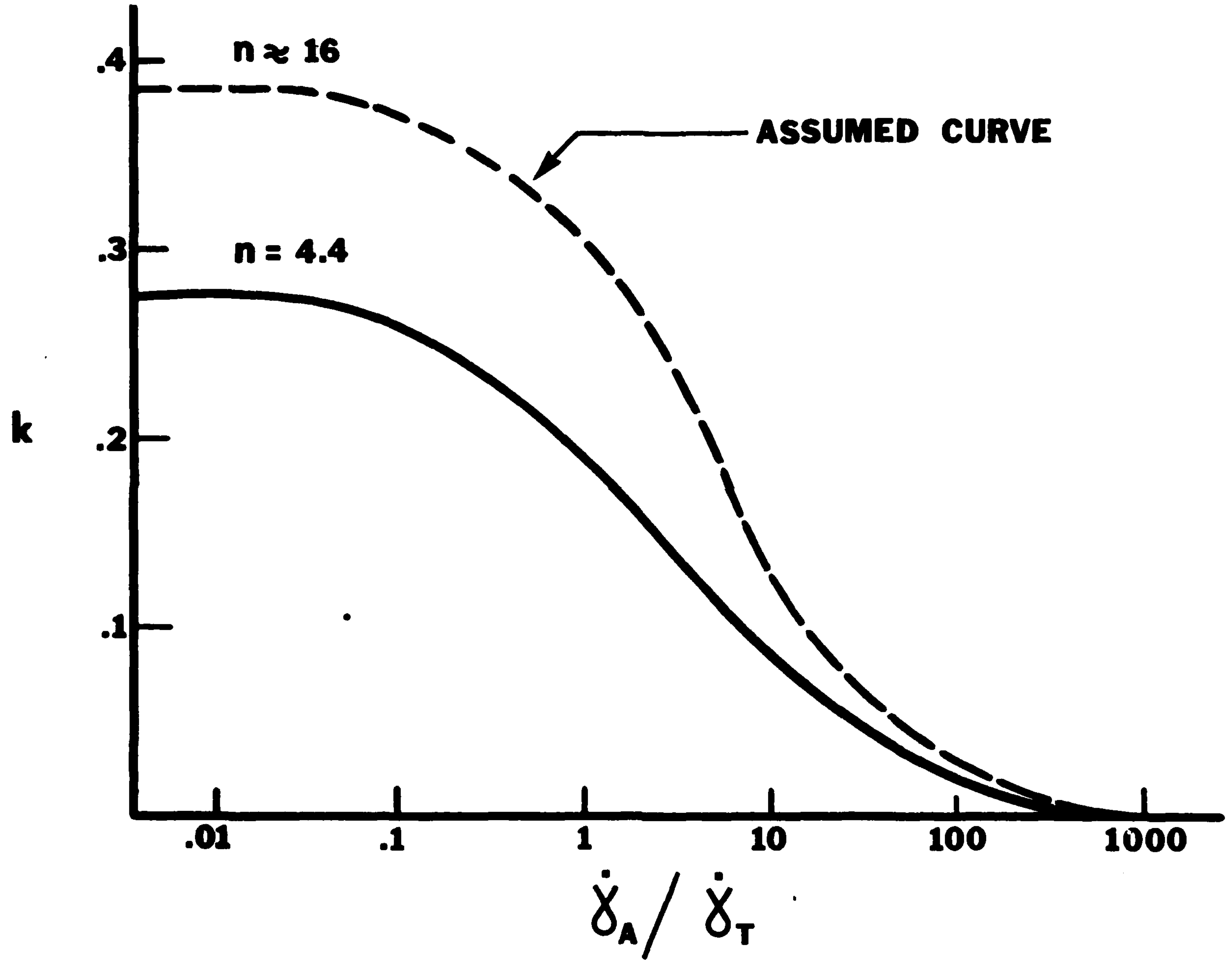

Figure 15 The contribution of grain boundary sliding as a function of deformation strain rate, $\dot{v}_A$ and the transition strain rate, $\dot{v}_T$, Ref. 9. The assumed behavior for MERL 76 which has a stress exponent of about 16 is illustrated by the dashed line.

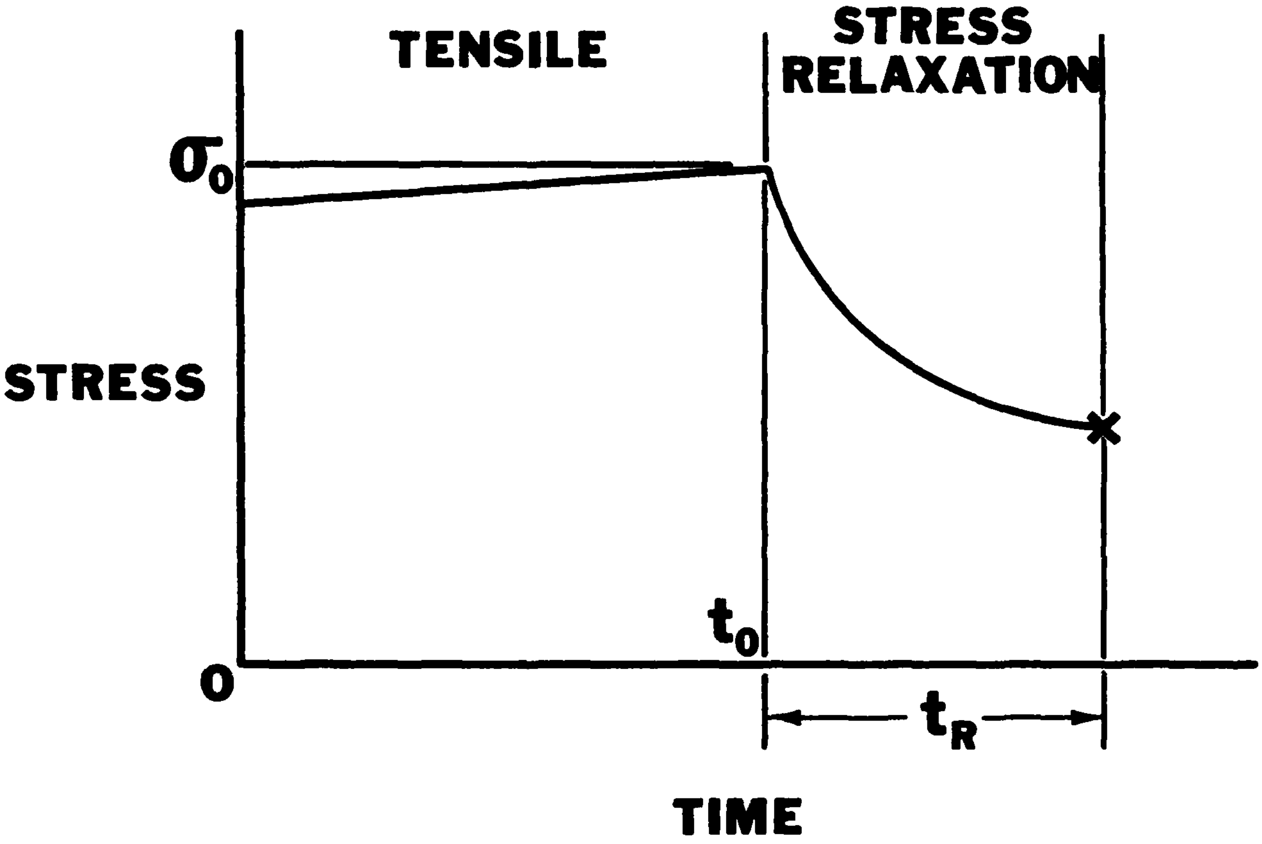

Figure A-1 Schematic illustration of stress relaxation.

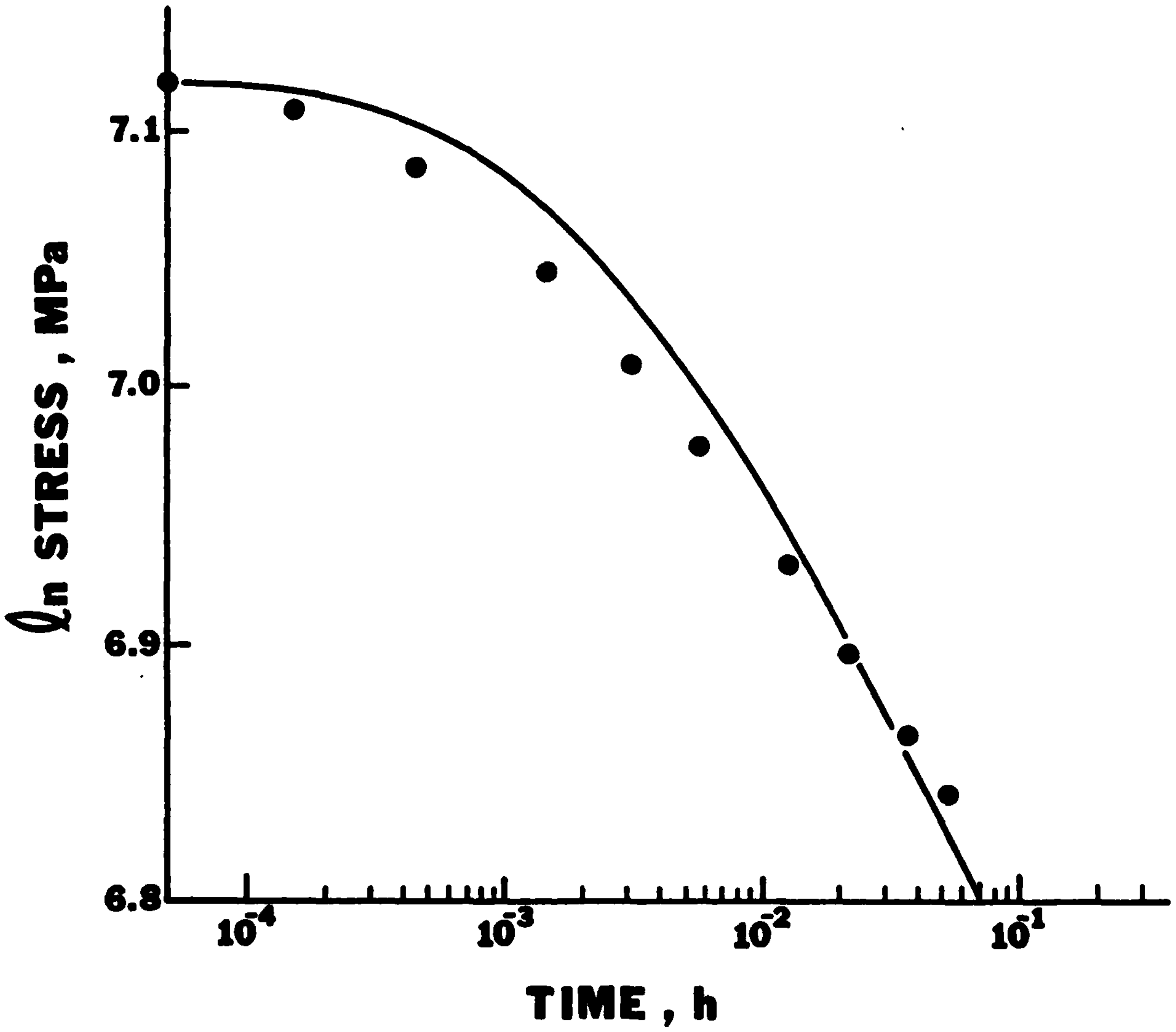

Figure A-2 Calculated (●) and actual stress relaxation data.

SECTION 4.0 THIRD-YEAR PROGRAM

EFFECT OF NONMETALLIC INCLUSIONS ON FATIGUE PROPERTIES OF A NICKEL-BASE SUPERALLOY

4.1 INTRODUCTION

Fatigue capability of conventional (cast and wrought) superalloys is generally limited by defects resulting from casting, forging, and finishing operations. Large carbide and boride particles present in these materials can also have an adverse effect on fatigue properties. The use of powder metallurgical (P/M) alloys have largely eliminated the problems associated with alloys fabricated by conventional techniques. The predominant type of defect in P/M alloys, which may potentially limit fatigue capability, has been found to be small nonmetallic inclusions formed during the melting and powder-atomization processes. Specifically, inclusions are erosion and reaction products from ceramic materials used in crucibles and other parts of the atomization equipment which come in contact with molten metal. The most common types are simple or mixed oxides of Al, Si, Mg, Cr, and Hf. Dimensions of inclusions in the final product can be restricted by the size of the opening in the sieve through which the powder particles are screened after atomization. For example, an 80 mesh screen has an opening of 177 μm, and thus for a minus 80 mesh powder the maximum inclusion sizes are about the same. With current melting and atomization practices, the density of inclusions in a superalloy powder is rather low, typically less than 5×10^{-4} weight percent. The relatively low numbers also mean that the detrimental effect of inclusions is on the crack initiation stage rather than for the propagation stage.

Fatigue problems associated with inclusions are not new. Occurrences in steels has been studied extensively for the past 45 years, and a recent review of the inclusion effect on fatigue has been given by Lankford(1). Some of the important observations may be summarized as follows. The crack nucleating propensity of an inclusion depends on the nature of the tesselated stresses in and around the inclusion, arising from differential thermal properties. These stresses depend on the difference of thermal expansion coefficients between the matrix and the inclusions, and the heat treatment sequence used. The criticality of an inclusion as a crack initiator also depends on the stress concentration effect (mechanical stresses) of the inclusion. This, in turn, depends on the location, shape, size, and orientation with respect to the applied stress. For example, a partially embedded (surface) inclusion is more detrimental than a completely embedded (sub-surface) inclusion. Cracks are more likely to nucleate at sharp corners rather than at a smooth surface of the inclusion.

In view of the large variety of inclusion parameters (chemistry, size, shape, etc.) and the statistical nature of the inclusion distribution (location, orientation, etc.) in any test sample, as many as one thousand tests in one case (2) are required to provide a reliable qualitative assessment of the inclusion effect in an alloy. The large number of variables present in the test results makes quantitative analysis of inclusion effects by a fracture mechanics approach complex, although notable efforts have been made(3,4).

To better understand the inclusion effects, the inclusion parameters must be carefully controlled, and the powder precursor of nickel-base superalloy is especially well suited for this purpose. In the present study, two types of oxides, alumina and magnesia, were seeded into a modified IN100 powder alloy designated MERL 76. These ceramics were selected based on their thermal expansion coefficients ; also both materials are used as refractories in superalloy processing. The thermal expansion coefficients of magnesia and alumina are about 94 and 54 percent that of the base metal, respectively (Table I). Inclusions of symmetrical shapes, primarily disks, were used in this study. An inclusion was so positioned in the loose powder that after consolidation and machining, half of the inclusion remained and intersected the surface near the center of the gage length of a fatigue specimen. Thus, a disk inclusion was reduced to a semicircular surface crack initiator under fatigue conditions. The primary purposes of this study were to evaluate the effect of inclusion compositions and size on fatigue crack nucleation and propagation. Most of the observations were made at 20°C; a limited number of tests were conducted at 482°C.

4.2 EXPERIMENTAL

Fabrication of Inclusions. The inclusions were fabricated from nominally 99.9 percent pure alumina and magnesia rods which had measured densities 0.95 and 0.86 of theoretical, respectively. Thin wafers of thicknesses about 0.13 mm for alumina and 0.23 mm for magnesia were cut from these ceramic rods. Disks of diameters 0.51, 0.76, and 1.02 mm were prepared from the wafers using an ultrasonic cutting machine. Several small inclusions, 0.25 mm diameter and 0.08 mm thick, were also made from the alumina wafers. A number of sapphire inclusions with spherical and cuboidal shapes were procured for this study. Prior to seeding, the inclusions were ultrasonically cleaned for 10 minutes in an equivolume mixture of methyl ethyl ketone and trichloroethylene, followed by drying in air.

Seeded Specimen Preparation. The alloy selected for this study was MERL 76 in the form of -325 mesh powder. The alloy composition, in weight percent except the oxygen and nitrogen contents, was determined to be:

Ni	Cr	Co	Mo	Al	Ti	Nb	Hf	B	Zr	C	O	N
Bal.	12.1	18.0	3.2	5.1	4.2	1.5	0.6	0.022	0.08	0.03	129ppm	16ppm

Seeding was accomplished as follows. The cleaned inclusions were placed individually at predetermined locations on the powder surface in a container half filled with loose powder. The locations of the defects were positioned accurately through the use of a template in which small holes were located at predetermined sites. After the placement of the defects, the top half of the container was filled and the powder was vacuum sintered at 1182°C for 2 hr. The sintered compacts were further consolidated by hot isostatic pressing at 1182°C, 103 MPa for 3 h, followed by heat treatments of 1166°C for 2 h, air cooled and 760°C for 8 hr, air cooled. Fatigue specimens with nominal gage dimensions 6.4 mm diameter and 12.7 mm long were machined from the heat treated material. The gage diameters were surface ground and about 25 μm diameter was removed in the last several passes. To study surface effects, one specimen was glass-bead peened (6N) after machining, and a second specimen underwent a large surface cut, 200 μm, in the final operation to simulate more abusive machining. To facilitate crack observation, the machining marks on the gage surface were removed by polishing with 600 grit paper initially and finally with 0.3 μm diamond paste in a direction parallel to the specimen axis.

Fatigue Testing. The fatigue specimens were cycled at stresses of either 930.2 MPa or 1068.0 MPa at an R ratio (minimum stress to maximum stress) of 0.03 and at a frequency of 2 Hz. The test temperature was either 20°C or 483°C. Tests were periodically interrupted for crack inspection using a plastic replica technique.

4.3 RESULTS

Specimen Characterization. The microstructure of the seeded MERL 76 specimens is shown in Figure 1. The microstructure is similar to that of the conventionally processed MERL 76, which consists of blocky gamma prime particles at grain boundaries and smaller secondary gamma prime particles distributed intragranularly. The fine gamma prime particles which precipitated during cooling and the 760°C aging treatment are not resolved at this magnification. The average grain diameter is about 37 μm. The oxygen and nitrogen contents in the seeded specimens are 221 and 16 ppm respectively. The former is slightly higher than that of the conventional consolidations, which is attributable to air exposure of the powder during the seeding procedure.

The configuration of the fatigue specimen used in the present study is shown in Figure 2 in which the exposed diametral section of a semicircular inclusion on the gage surface may be seen. Typical appearances of the magnesia inclusions in the test specimens are shown in greater detail in Figures 3a and 3b; those for alumina are shown in Figures 3c and 3d. The integrity of all the inclusions after machining was excellent, as no cracks were observed in the inclusions even in the specimen which had a more severe machining operation. The bonding between the base metal and the inclusions also appeared to be good. Occasionally shallow gaps at the magnesia:MERL 76 interfaces were observed which apparently formed during specimen machining; no such gap was found at the alumina:MERL 76 interface. However, modification of the interface did occur during consolidation by the formation of hafnia particles which may be seen in Figure 3d as white particles. The reduction of magnesia and alumina by hafnium in MERL 76 is favored since the free energy of formation of hafnia (HfO_2) is the lowest, -838 KJ/mol versus -429 KJ/mol for magnesia and -275 KJ/mol for alumina, at the powder consolidation temperature(7).

The appearance of the inclusion (0.51 mm diameter, semicircular alumina) after glass-bead peening (6N) is illustrated in Figure 4, which shows several interesting features. First, no cracks formed in the inclusion as the result of peening, instead small (cleavage) facets were produced at the inclusion surface. Secondly, the surface layer of the base metal was so severely deformed that it smeared over the inclusion:matrix interface at several locations.

Fatigue Crack Nucleation From Semicircular Inclusions. Crack nucleation in the base metal is preceded invariably by damage to the seeded inclusion, which occurs readily. Cracks were found in both the alumina and the magnesia inclusions when stressed to only 340 MPa. Further damage to the inclusions occurred during the first several stress cycles. Three types of damage have been observed:

1. Cracking within the inclusion

2. Cracking at the inclusion: matrix interface

3. Debonding which, as will be illustrated later, results in complete interfacial separation with a gap considerably wider than a crack

The types of inclusion damage seem to be determined by the inclusion size and composition. The smallest alumina inclusions (0.25 mm diameter) cracked internally (Fig. 5a), while the largest alumina inclusions (1.02 mm diameter) cracked at the interface (Fig. 5c). With intermediate inclusion sizes, both interfacial and intraparticle cracking were observed (Fig. 5b). Similar trends were observed for the magnesia inclusions except that the fatigue damage to the largest inclusions (1.02 mm) occurred predominantly by debonding (Fig. 6) instead of by cracking at the interface. The fracture behavior of inclusions at 482°C was similar to that found at room temperature.

Nucleation of cracks in the base metal from discontinuities in the inclusions also occurred very rapidly and it was observed that several cracks often nucleated from one inclusion. However, not all the cracks formed in the initial stages of the test propagated. Under all test conditions, the nucleation of propagating cracks occurred during the first 5 percent of the life. It is therefore concluded that the fracture behavior of the inclusions does not have an important effect on crack nucleation behavior under the conditions evaluated in this program.

Crack Propagation From Inclusions. For a given type of inclusion and a given nominal inclusion diameter considerable scatter in crack propagation rates between specimens was measured. This scatter was also reflected in the fracture lives, and differences by factors of two to three have been observed (see Table II and IV). These variations complicated comparison of propagation rates of cracks from various inclusion sizes, types, and shapes. However, if we divide the specimens into two groups based on fracture lives, several interesting trends emerge. For example, Figure 7 shows the propagation rates of cracks emanating from semicircular alumina disks of several sizes. These data are from specimens in the long-life group which were tested at 1068 MPa, R = 0.03, 20°C. In Figure 7 the crack lengths were measured from the ends of an inclusion and the averages of both are shown. The most interesting feature illustrated in Figure 7 is that the initial propagation rates of a crack emanating from the 0.76 mm diameter inclusion are almost identical to that from the 0.25 mm diameter inclusion. Similarity of initial propagation rates of cracks emanating from the 0.51 mm diameter and the 1.02 mm diameter inclusions are also evident. After the cracks had extended 0.10 to 0.15 mm from the interface, the influence of inclusion size became important; as anticipated, a crack propagates at faster rates from a larger inclusion. Figure 8 illustrates crack propagation behavior of specimens in the short-life group. The crack propagation rates in these specimens are, not unexpectedly, faster than those in the long-life group (Figure 7). There are also some similarities in initial propagation rates of cracks emanating from inclusions of different diameters. However, the similarities are less striking and confined to shorter crack lengths.

The propagation behavior of cracks emanating from semicircular magnesia inclusions of various diameters is illustrated in Figure 9. The similarity between these results and those shown in Figure 8 is obvious and indicates that no discernible difference in the propagation behavior between cracks emanating from alumina and magnesia inclusions.

The influence of inclusion shape on crack propagation behavior is illustrated in Figure 10 where data from 0.25 mm and 0.51 mm diameter semicircular alumina inclusions is compared with that from a cuboidal alumina inclusion of an intermediate size. Again, little discernible effect of inclusion shape on crack propagation behavior can be seen from Figure 10.

Temperature and stress have the expected effect on crack propagation rates as shown in Figure 11. A test temperature of 482°C increases significantly the crack propagation rates. Increasing stress also increases the crack growth rate; however, the effect is smaller than for the temperature increase.

Fracture Behavior. The fatigue fracture lives of MERL 76 specimens containing semicircular alumina and magnesia inclusions, and tested at 1068 MPa, R = 0.03 at 20°C, are given in Table II, which shows clearly that the fracture life is not a strong function of either inclusion size or inclusion composition. A fourfold increase in inclusion size resulted in a reduction of fracture life by a factor of about four. Life differences between alumina and magnesia, if any, are certainly less than the scatter in fracture lives. Specimen No. 241 was glass-bead peened, and Specimen No. 245 had a more severe surface machining operation than all others. The life differences among these specimens and Specimen No. 288 are again not discernible from the data scatter.

As indicated above, longer fracture lives can be attributed directly to slower initial propagation of cracks emanating from inclusions. In the search for factors which governed the initial crack growth behavior, detailed measurements were made on the inclusion dimensions and orientations. The mode of crack propagation, as recorded on the fracture surface, was also examined.

Table III shows the rather detailed inclusion measurements made. The length of the exposed inclusion on the gage surface is denoted by ℓ, and the depth of the inclusion below the gage surface is given by d. The angle between the normal to the line of intersection and the stress axis is designated α. The inclusion areas projected onto the plane of fracture were calculated from the inclusion dimensions and the specimen diameters. Examination of Table III and data for other specimens shows that the variation on fracture lives for a given nominal inclusion size cannot be accounted for by any one of the inclusion parameters shown in the Table. The fractographic features of a specimen with a long life (Specimen No. 232, Table IV) and one with a short life (Specimen No. 229, Table IV) are given in Figure 12. In both cases the fracture is faceted in an area adjacent to the inclusion and becomes featureless away from the inclusion. The fractography is shown in greater detail in Figure 13. The widths of the bands of faceted fracture are nonuniform and appear to be larger on the left of the inclusion in both cases. No discernible difference in fractographic features between the long-life and the short-life specimens can be observed in Figure 12. Thus the reasons for the variation in initial crack growth behavior are not obvious from these measurements. Part of the variation may be attributable to normal scatter in material properties and a combination of various inclusion orientation and size parameters. It is thought that the exact manner that the inclusion was fractured may also be important. However, no good correlation between the inclusion fracture modes, as observed on the surface, and the specimen fracture lives is obtained for inclusions of same nominal diameters. An unambiguous correlation would be difficult since the crack path beneath the inclusion surface is unknown.

Returning to the test results, Table IV shows the fracture lives of MERL 76 specimens seeded with 0.51 mm diameter semicircular inclusions under various test conditions. Reducing the maximum stress from 1068 MPa to 980 MPa resulted in a life improvement by a factor of about 2 at room temperature and at 482°C. Fatigue testing at the elevated temperature lowers the average fatigue lives by a factor of about 6. At all the conditions studied, fatigue life is determined by propagation as crack nucleation occurred in the first cycles of a test. The fracture lives of MERL 76 specimens seeded with alumina inclusions of various shapes are given in Table V. As can be anticipated from the crack propagation results shown in Figure 10, no significant effect of inclusion shape on fracture life can be observed in Table V.

4.4 DISCUSSION

Previous studies of effects of inclusion composition on fracture of steels has focused attention on the importance of the tesselated stresses due to differential thermal properties of the metal and the inclusions(6). An inclusion which has a larger thermal expansion coefficient than the metal would develop tensile stresses across the inclusion:metal interface and tends to produce voids at the interface. Conversely, an inclusion with a smaller thermal expansion coefficient develops tensile stresses in the surrounding metal, facilitating crack nucleation under fatigue conditions. It is also believed that the presence of tesselated stresses could modify the initial propagation behavior of cracks emanating from inclusions. Thus, the overall fatigue behavior of an alloy could be significantly influenced by the type of inclusions it contains. Alumina and magnesia which have significantly different expansion coefficients (see Table I) were chosen to test this hypothesis. In the present study, tesselated stresses were introduced during cooling from the aging treatment temperature (760°C). It was anticipated that effects of these stresses on fatigue behavior would be the smallest for magnesia, which has a thermal expansion coefficient similar to MERL 76, and largest for alumina whose thermal expansion coefficient is about half that of MERL 76. The results of the present study indicate that cracking of the inclusion and/or interfacial debonding occurred in the first few stress cycles for both types of inclusions. In fact, cracks were found in both types of inclusions when stressed to only 340 MPa. The only difference that was noted, which might possibly be associated with the dissimilar thermal expansion coefficients, is that for the 1.02 mm diameter inclusions debonding occurred for the magnesia and interfacial cracking for the alumina inclusion. Nucleation of cracks in the matrix from the discontinuities in the inclusions followed very rapidly under all test conditions. No doubt, the ease of crack nucleation in the matrix is due to the high stresses at the extremities of cracks in the inclusions. Thus, the use of large inclusions, which resulted in large inclusion cracks, and fatigue testing at high stresses collectively nullified the effects of tesselated stresses on matrix crack nucleation. Further, the development of large plastic zones at the inclusions during fatigue (see, for example, Figure 6) tends to obscure or eliminate these stresses. From the above considerations, it is concluded that tesselated stresses could be important only in situations involving very small inclusions and/or fatigue testing at low stresses.

The lack of influence of inclusion shapes can be explained similarily, but several additional factors must also be examined. Previous work by the present authors have shown significant effect of inclusion shapes on subsurface crack nucleation(8). In particular, it was demonstrated that a spherical alumina inclusion as large as 1.6 mm failed to nucleate fatigue cracks in the surrounding material even though the sphere itself developed numerous fatigue cracks. In contrast, a disk-shaped alumina inclusion, as small as 0.25 mm diameter, nucleated cracks in the surrounding material. The appearances of these subsurface inclusions after fracture are shown in

Figure 14. The reasons for the difference is not clear. One factor that may contribute to the ease of crack nucleation from surface is that a hemispherical rather than spherical inclusion was tested. Another contributing factor may be the larger crack opening displacement associated with a surface crack due to a higher degree of relaxation on the surface.

An important finding in the present study is that the initial propagation rates of cracks emanating from an inclusion are independent of inclusion size. This observation suggests that the inclusions behaved like a notch rather than a crack, and the initial crack propagation rates are determined by the geometrical shape rather than the length of the notch. This point becomes clearer if the methodology of linear elastic fracture mechanics (LEFM) is used to describe the stress dependence of cracking rates found in the present study. A convenient way to represent the crack growth data in the LEFM approach is by means of a parameter ΔK, the cyclic stress intensity factor. In the calculation of ΔK the traditional assumption that the initial crack length is simply equal to the inclusion diameter is used. The resulting LEFM representation of the crack growth data for various inclusion diameters at 20°C is illustrated in Figure 15, in which crack growth rate da/dN was obtained by numerical differentiation of a-N data. This calculation involved a FORTRAN computer program to fit a second-degree Lagrangian interpolation polynomial to each three consecutive data points; da/dN was then computed as a derivative of each polynomial at the central data point. The calculation of ΔK was according to the procedures described by Irwin(9). With this approach, all the crack growth data at 20°C lie in a narrow band at large values of ΔK irrespective of inclusion size, shape, and type, and lie close to the crack growth data of a similar alloy determined by standard techniques at 20°C (10) as given by the dashed line in Figure 15. Separations of curves occur at smaller ΔK values and appear to depend on inclusion size. However, the separations are a direct consequence of the simplifying assumption used for the calculation of ΔK at small crack lengths, for we assign a higher value of ΔK to a crack from a larger inclusion. As we have shown, the initial propagation rates are almost independent of inclusion size.

If the fracture lives of specimens containing inclusions of various diameters are calculated from the average crack growth behavior (the dotted line in Figure 15) using the preceding simplifying assumption, large discrepancies between the actual fracture lives and the calculations (lower curve, Figure 16) are obtained. In particular, the calculations show a considerably larger dependence of fracture life on inclusion size than that observed. However, if the fracture lives are calculated by assuming that the inclusion behaves as a notch, somewhat better agreement is obtained as illustrated by the upper curve in Figure 16. The notch life was calculated using the formulation of Dowling (10) who divided notch fatigue life, L, into two parts. The initial crack growth is controlled by the stress concentration factor k_t, independent of the notch length. The effect of notch length, c, only enters in the second part of the calculation after the crack has propagated a specific distance l_m. Values of k_t and l_m have been calculated for some simple notch shapes by Dowling. The expression for notch life is:

$$L = \frac{l_m^{1-n/2} - l_i^{1-n/2}}{A(1-n/2)\,(.715\,k_t\sqrt{\pi}\Delta\sigma)^n} + \frac{(c + l_f)^{1-n/2} - (c + l_m)^{1-n/2}}{A(1-n/2)\,(.715\sqrt{\pi}\Delta\sigma)^n} \qquad (1)$$

where l_i and l_f are the initial crack length and the final crack length, $\Delta\sigma$ is the stress range and A & n are parameters in the crack growth law:

$$da/dN = A\Delta K^n \qquad (2)$$

Equation (1) is a slight modification of Dowling's original expression to account for the difference in notch shapes considered. For our calculation, a crack of length $l_i = 1.25 \times 10^{-6}$m is assumed to be present initially i.e., no nucleation life which is in accord with our experimental observation. l_m is assumed to be 5×10^{-5}m which is of the order of the crack length beyond which differences in crack growth rates between various inclusion sizes are observed (Figures 7, 8 and 9). The stress concentration factor k_t of a semi-circular notch is assumed to be 4.5, which is between that for circular and elliptical notches.

The observed initial crack propagation behavior and the better agreement between the notch life calculations and the fracture lives lead us to conclude that the inclusions in the present studies behaved more like notches than cracks. However, this is not a general conclusion since good correlation between the actual fracture lives and the calculations based on the equivalence of initial crack size and inclusion size has also been demonstrated(12). It should, however, be pointed out that there are substantial differences between the inclusions in these two cases. In particular, the inclusions in the second case are flake-like. The fatigue lives associated with inclusion initiated fractures can be bounded by these two approaches. The lower-bound life is obtained by assuming that the initial crack size is equal to the inclusion size, and the upper-bound life can be calculated by treating an inclusion as a notch. Actual behavior lies between these two extremes. We note that at small inclusion sizes the difference between the two life calculations is not large and it may be difficult to differentiate between the two approximations. However there is an implication that large inclusions, not found in P/M alloys but possibly present in wrought alloys, may be less damaging than would be anticipated from current fracture mechanics life prediction methodology.

4.5 CONCLUSIONS

The major conclusions that can be drawn from the results of the investigation are as follows:

1. Cracking of alumina and magnesia inclusions occurs in the first several stress cycles, and fatigue cracks are formed in the metal within the first 5% of life.
2. No effect of tesselated stresses and inclusion shape on either crack nucleation or propagation behavior was found. However, these factors could be important in situations involving very small inclusions and/or tests at low stresses.
3. Both the initial propagation behavior of cracks extending from the inclusions and the analysis of fracture lives suggest that the effect of inclusions in the present study is similar to that of notches, which provides an upper-bound fatigue life for inclusion-initiated fracture.
4. The results suggest that large equiaxed inclusions may not reduce fatigue life to the extent predicted by the current fracture mechanics model. However, the approach provides a useful lower bound for the behavior.

REFERENCES

1. J. Lankford: International Metals Reviews, 1977, Vol. 22, pp. 221-228
2. H. N. Cummings, F. B. Stulen, and W. C. Schulte: Trans. ASM, 1957, Vol. 49, pp. 482-516
3. J. Lankford: Engr. Fract. Mech., 1977, Vol. 9, pp. 617-624
4. G. Harkegard: Engr. Fract. Mech., 1974, Vol. 6, pp. 795-805
5. Coors Porcelain Co., Golden, Colorado, Bulletin No. 953
6. D. Brooksbank and K. W. Andrews: J. Iron Steel Inst., 1972, pp. 246-255
7. J. P. Coughlin "Heats and Free Energies of Formation of Inorganic Oxides," Bulletin 542, Bureau of Mines, 1954.
8. C. C. Law and M. J. Blackburn: Unpublished work at Pratt & Whitney Aircraft, 1978
9. G. R. Irwin in "The Surface Crack - Physical Problems and Computational Solutions," Ed. J. L. Swedlow, p. 1, ASME publication, November 1972
10. C. G. Annis, Jr., R. M. Wallace, and D. L. Sims: "An Interpolative Model for Elevated Temperature Fatigue Crack Propagation,: AFML-TR-76-176, November 1976
11. N. E. Dowling in "Fracture Mechanics - Proc. of the 11th National Symp. on Fracture Mechanics: Part 1" Ed. C. W. Smith, pp. 247-273, ASTM STP677, 1978
12. Y. O. Chen: Unpublished work at Pratt & Whitney Aircraft, 1979

TABLE I

THERMAL EXPANSION COEFFICIENTS AND ELASTIC MODULI OF SEEDED INCLUSIONS IN MERL 76

Material	Mean Expansion Coefficient (20°-800°C) 10^{-6}/°C	Young's Modulus GPa	Poisson's Ratio
Alumina (99.9%) (Ref. 5)	7.8	393	0.22
Magnesia (Ref. 6)	13.5	306	0.18
MERL 76	14.4	207	0.30

TABLE II

FATIGUE LIVES OF MERL 76 SPECIMENS CONTAINING SEMICIRCULAR ALUMINA AND MAGNESIA INCLUSIONS AT 20 °C, 1068 MPa, R=0.03, 2Hz

Nominal Inclusion Dia. mm	Alumina		Magnesia	
	Specimen No.	Life Cycles	Specimen No.	Life Cycles
0.25	247	28,443	-	-
	256	36,549	-	-
0.51	241	17,655	251	20,306
	228	13,943	259	22,245
	245	29,032		
0.76	249	28,237	244	11,941
	262	11,174		
1.02	242	13,239	258	9,311
	261	9,458	260	6,066

TABLE III

DIMENSIONS AND ORIENTATIONS OF THE ALUMINA INCLUSIONS IN TABLE II

Nominal Inclusion Diameter mm	Specimen No.	Actual Inclusion Dimensions			Projected Inclusion Area mm^2	Fracture Life Cycles
		ℓ mm	d mm	α degree		
0.25	247	0.2401	0.1470	4.6	4.258×10^{-2}	28,443
	256	0.2401	0.1225	22.0	1.787×10^{-2}	36,549
0.51	228	0.5709	0.2940	14.0	1.465×10^{-1}	13,943
	241	0.5390	0.2940	3.0	1.619×10^{-1}	17,655
	245	0.4900	0.2940	0.0	1.716×10^{-1}	29,032
0.76	249	0.6811	0.2940	1.0	1.297×10^{-1}	28,237
	262	0.6787	0.441	2.5	3.987×10^{-1}	11,174
1.02	242	0.9604	0.4165	0.0	3.194×10^{-1}	13,239
	261	0.9261	0.3675	3.8	2.561×10^{-1}	9,458

TABLE IV

FATIGUE LIVES OF MERL 76 SPECIMENS CONTAINING 0.51 mm DIAMETER SEMICIRCULAR ALUMINA INCLUSIONS AT 20°C AND 482°C, R=0.03, 2Hz

Stress MPa	20°C		482°C	
	Specimen No.	Life Cycle	Specimen No.	Life Cycle
930	229 232 257	23,768 69,573 52,240	231	8267
1068	245 228 241	29,032 13,943 17,655	230	3325

TABLE V

FATIGUE LIVES OF MERL 76 SPECIMENS CONTAINING SEMICIRCULAR, CUBOIDAL, AND HEMISPHERICAL ALUMINA INCLUSIONS AT 20°C, 1068 MPa, R=0.03, 2Hz

Inclusion		Specimen No.	Life Cycle
Shape	Size, mm		
Semi-circular Disk	0.25	247 256	28,443 36,549
Cube	0.38	223	25,383
Semi-circular	0.51	225 228 241	29,032 13,943 17,655
Cube	0.64	221	16,060
Semi-circular Disk	0.76	249	28,237
Hemisphere	0.80	224	13,812
Semi-circular Disk	1.02	242	13,239

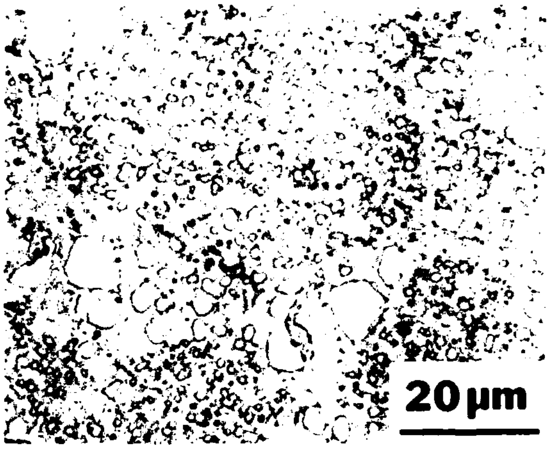

Figure 1 Microstructure of the seeded MERL 76 specimens.

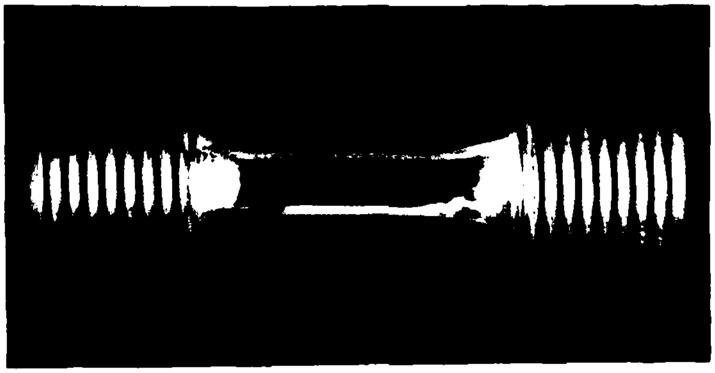

Figure 2 Typical appearance of a fatigue specimen, illustrating the exposed diametral section (~ 1.02mm) of a semi-circular inclusion.

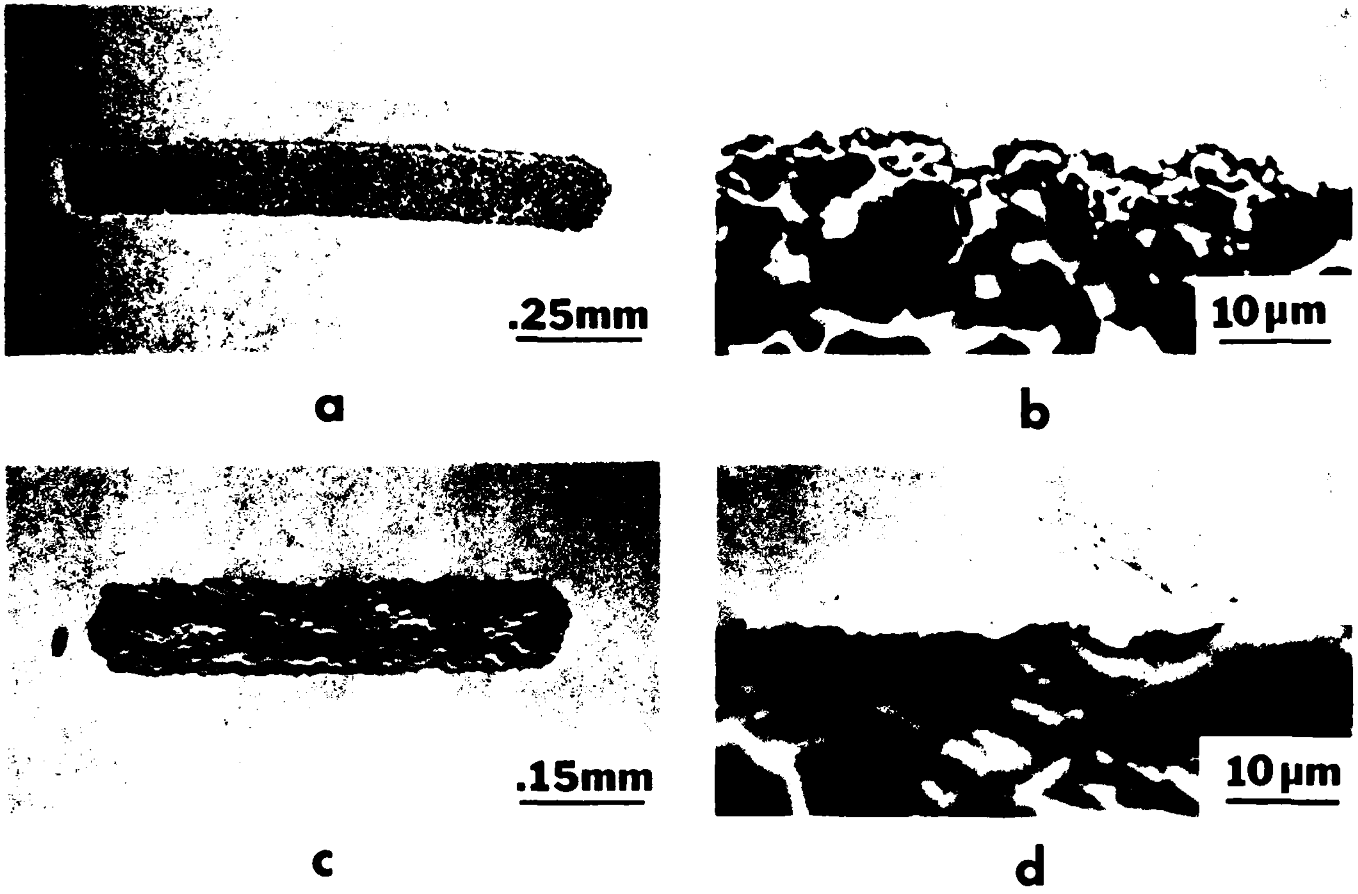

Figure 3 Typical appearances of the seeded inclusions in the gage surfaces of fatigue specimens. (a) magnesia (b) the magnesia: MERL 76 interface (c) alumina (d) the alumina: MERL 76 interface. (Note the formation of hafnia particles which appear in white in the MERL 76).

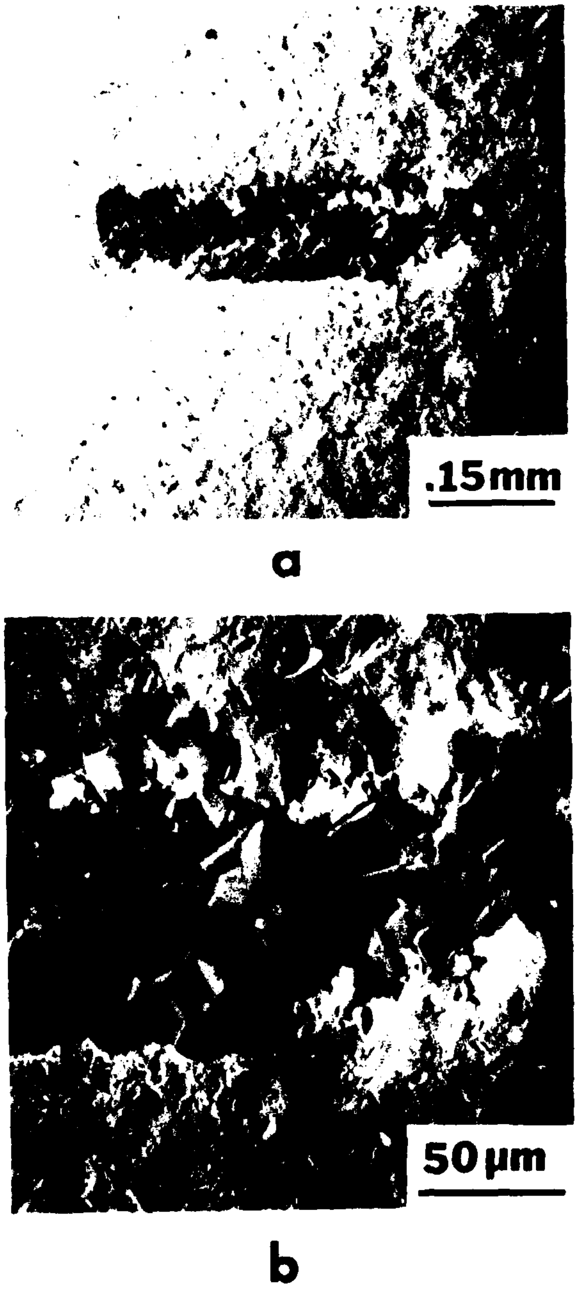

Figure 4 (a) General appearance of an inclusion (0.51 mm diameter, semicircular alumina) after glass-bead peening (6N)
(b) detailed view, illustrating formation of small cleavage facets in the alumina and deformation of the base metal resulting from glass-bead peening.

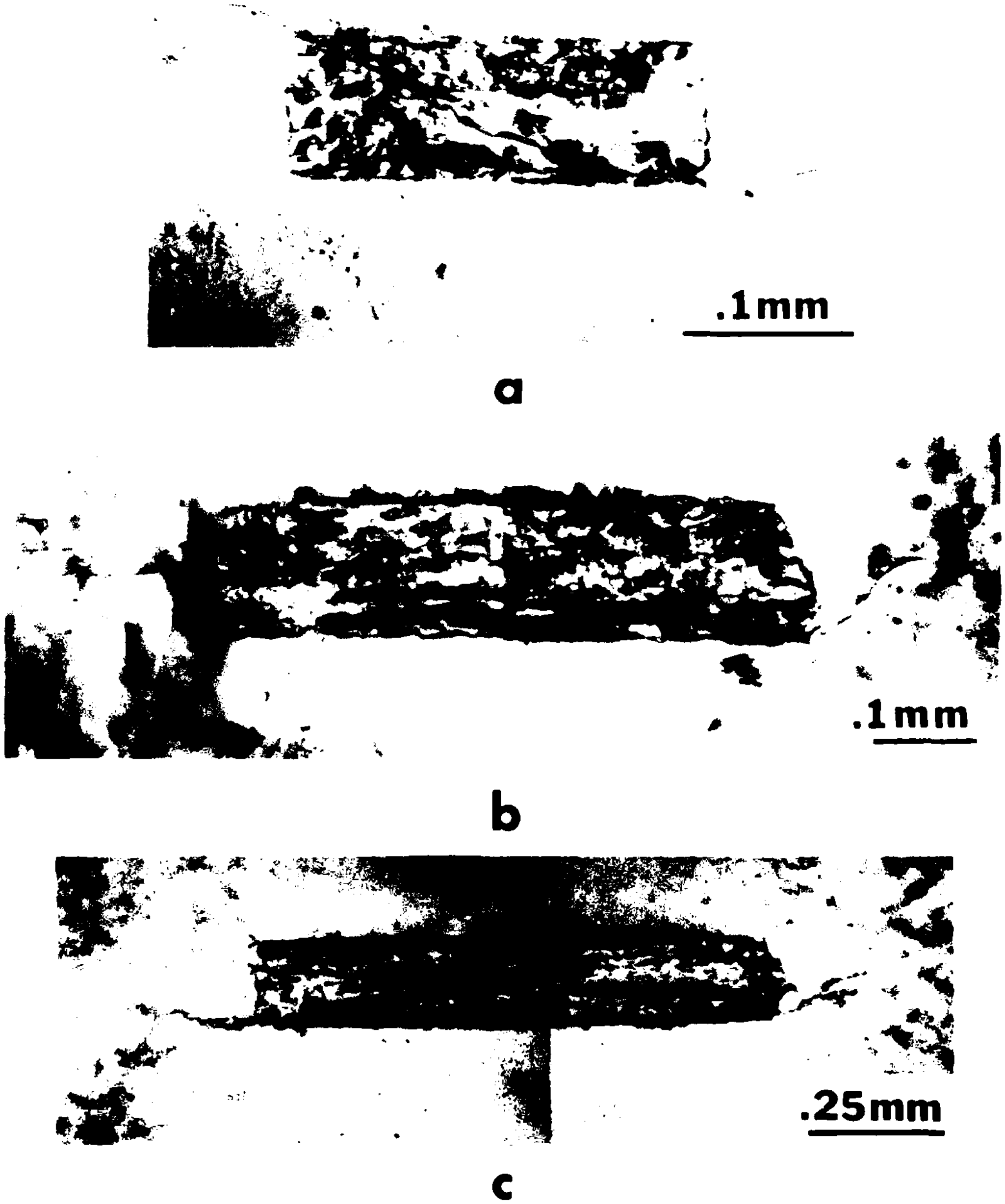

Figure 5 Fatigue cracking in MERL 76 specimens seeded with semi-circular alumina inclusions and tested at 20°C, 1068 MPa, R = 0.03, 2 Hz (a) 0.25 mm diameter inclusion after 16000 cycles (b) 0.51 mm diameter inclusion after 19000 cycles (c) 1.02 mm diameter inclusion after 8000 cycles.

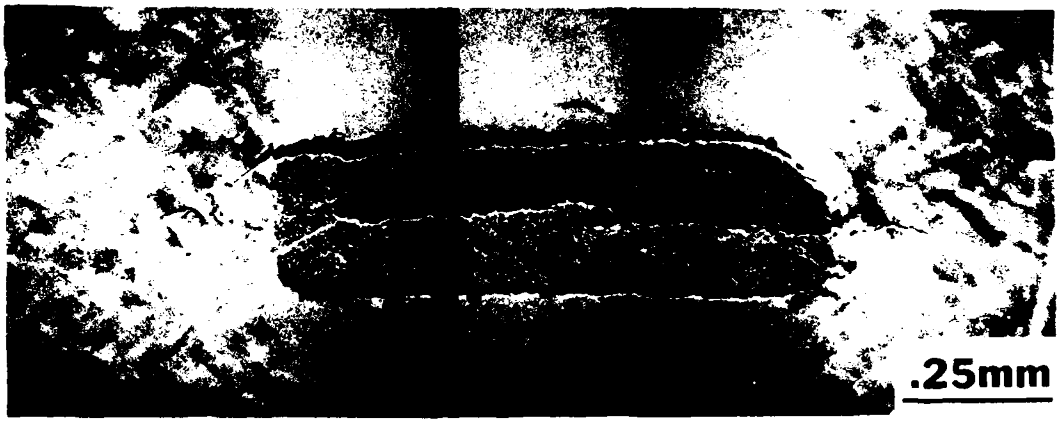

Figure 6 Fatigue cracking in a MERL 76 specimen seeded with a semi-circular magnesia inclusion (1.02 mm diameter) after 5000 cycles at 20°C, 1068 MPa, R = 0.03, 2 Hz.

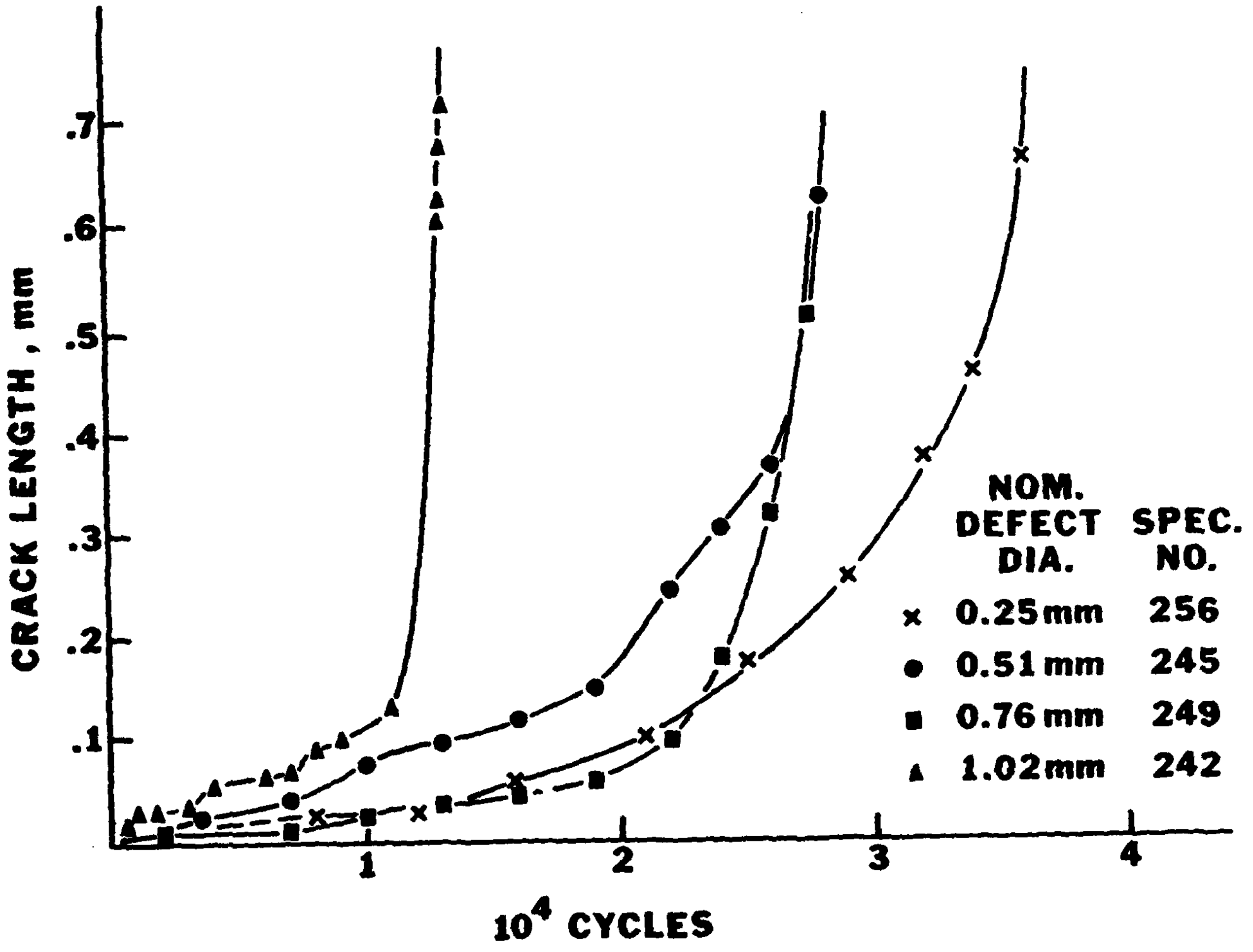

Fatigue 7 Propagation rates of fatigue cracks extending from semi-circular alumina inclusions of various sizes at 1068 MPa, 20°C. Data from specimens in the long-life group.

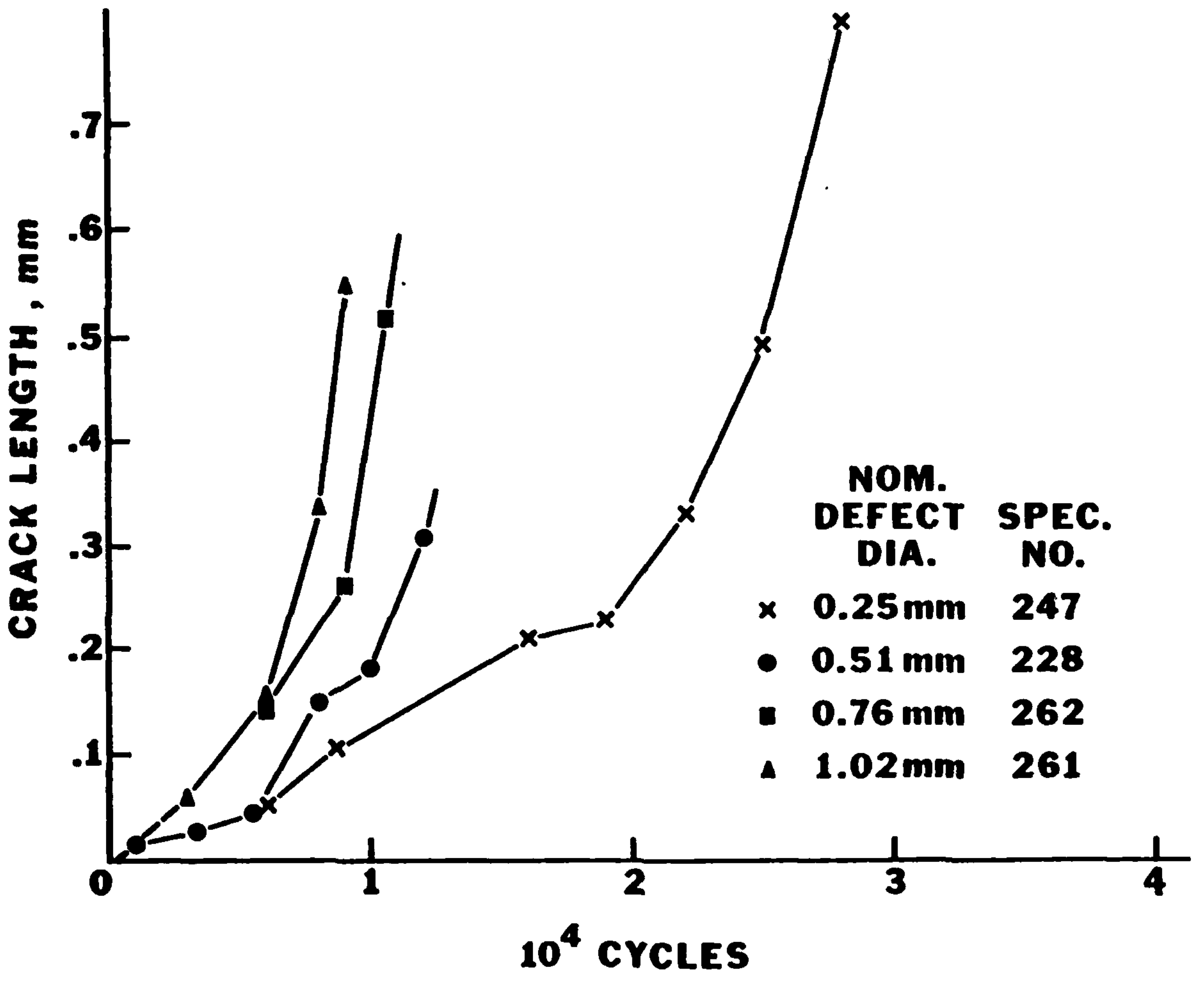

Figure 8 Propagation rates of fatigue cracks extending from semi-circular alumina inclusions of various sizes at 1068 MPa, 20°C. Data from specimens in the short-life group.

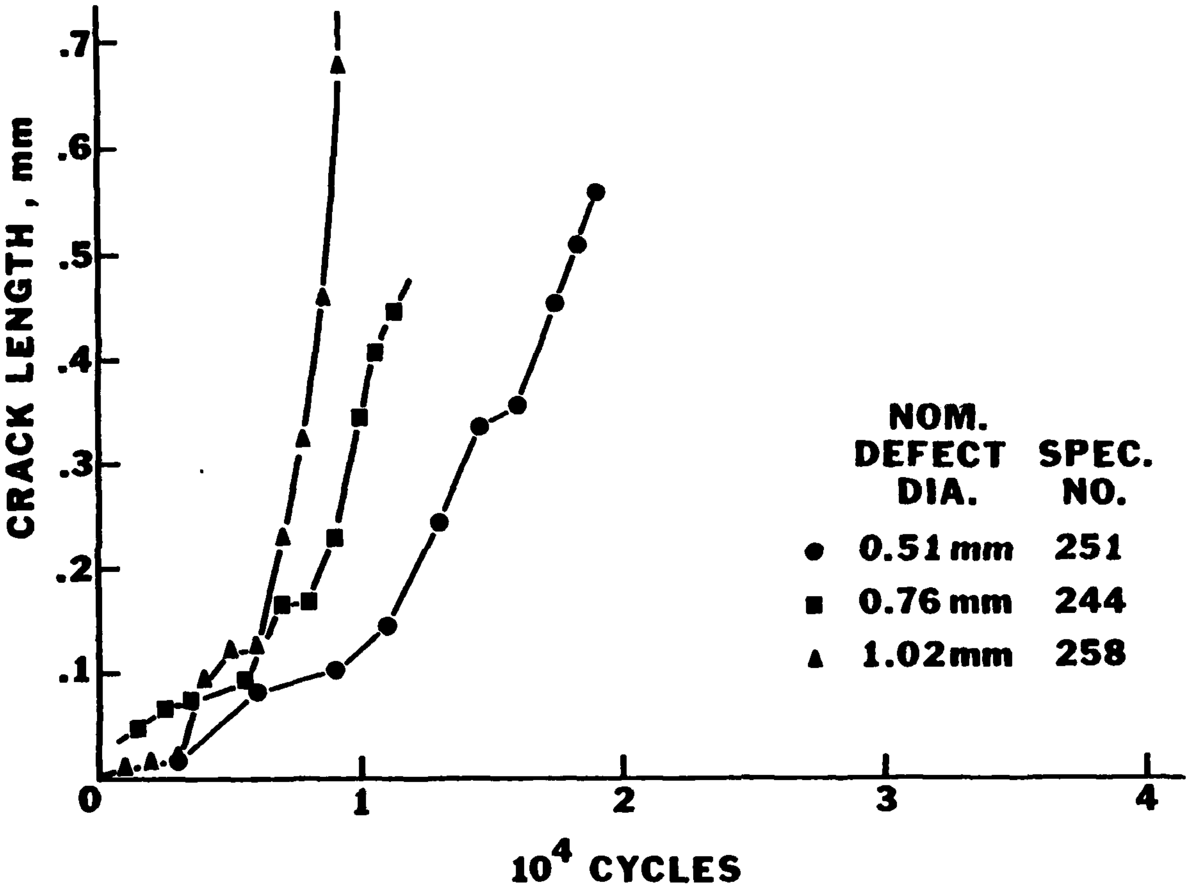

Figure 9 Propagation rates of fatigue cracks extending from semi-circular magnesia inclusions of various sizes at 1068 MPa, 20°C.

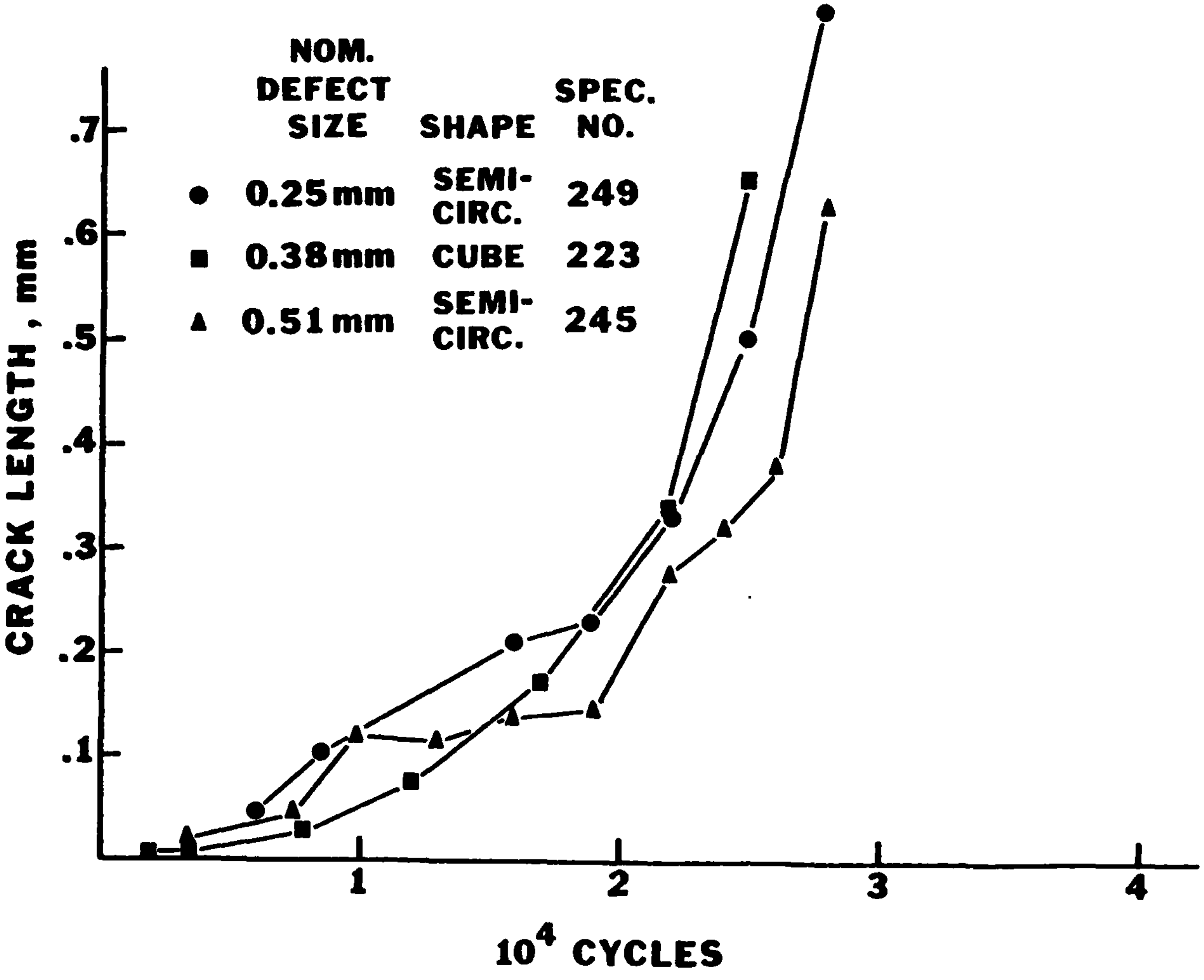

Figure 10 Propagation rates of fatigue cracks extending from semi-circular disk and cuboidal inclusions at 1068 MPa, 20°C.

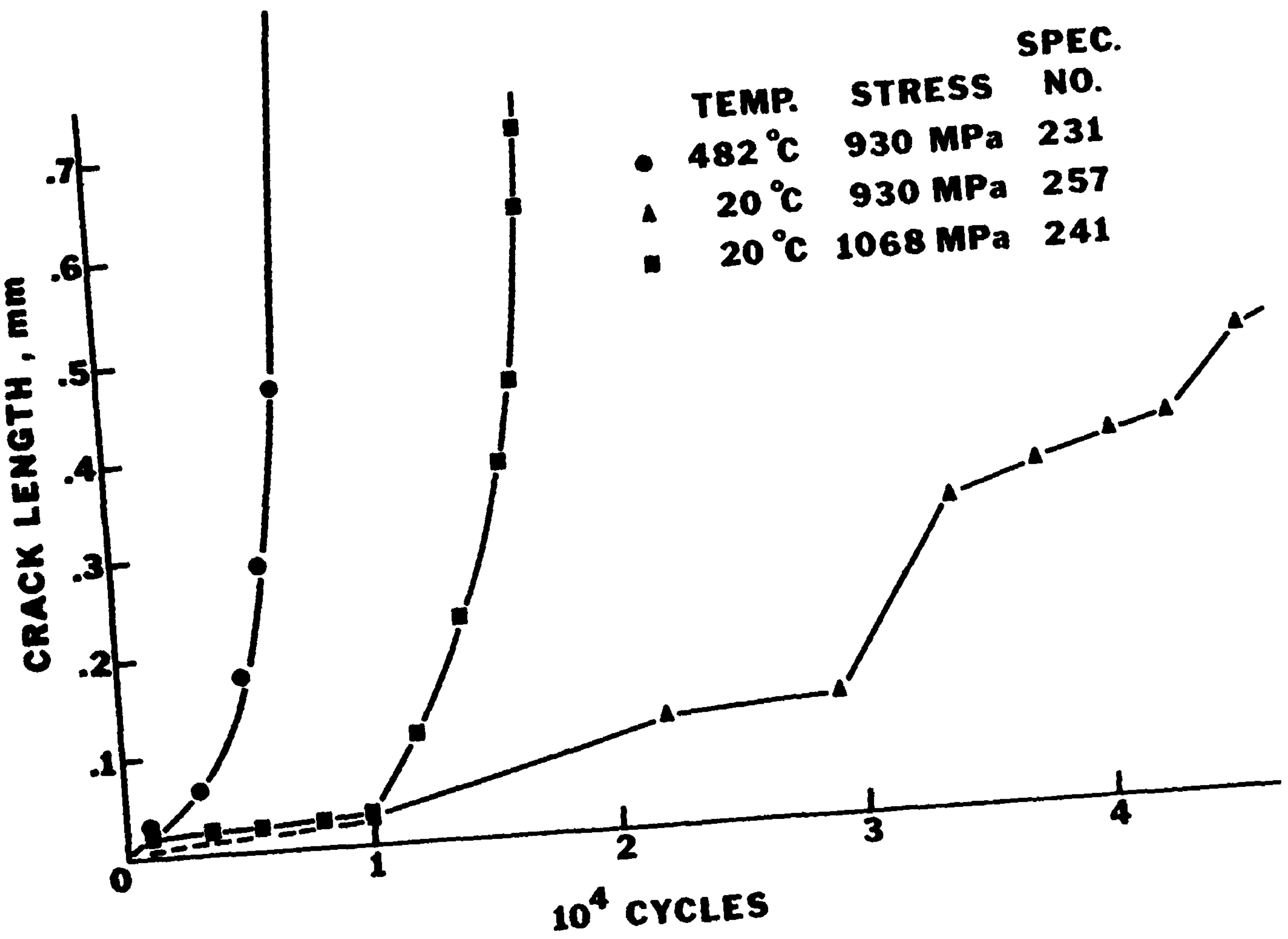

Figure 11 Propagation rates of fatigue cracks extending from 0.51 mm semi-circular alumina inclusions at 482°C/930 MPa, 20°C/930 MPa and 20°C/1068 MPa.

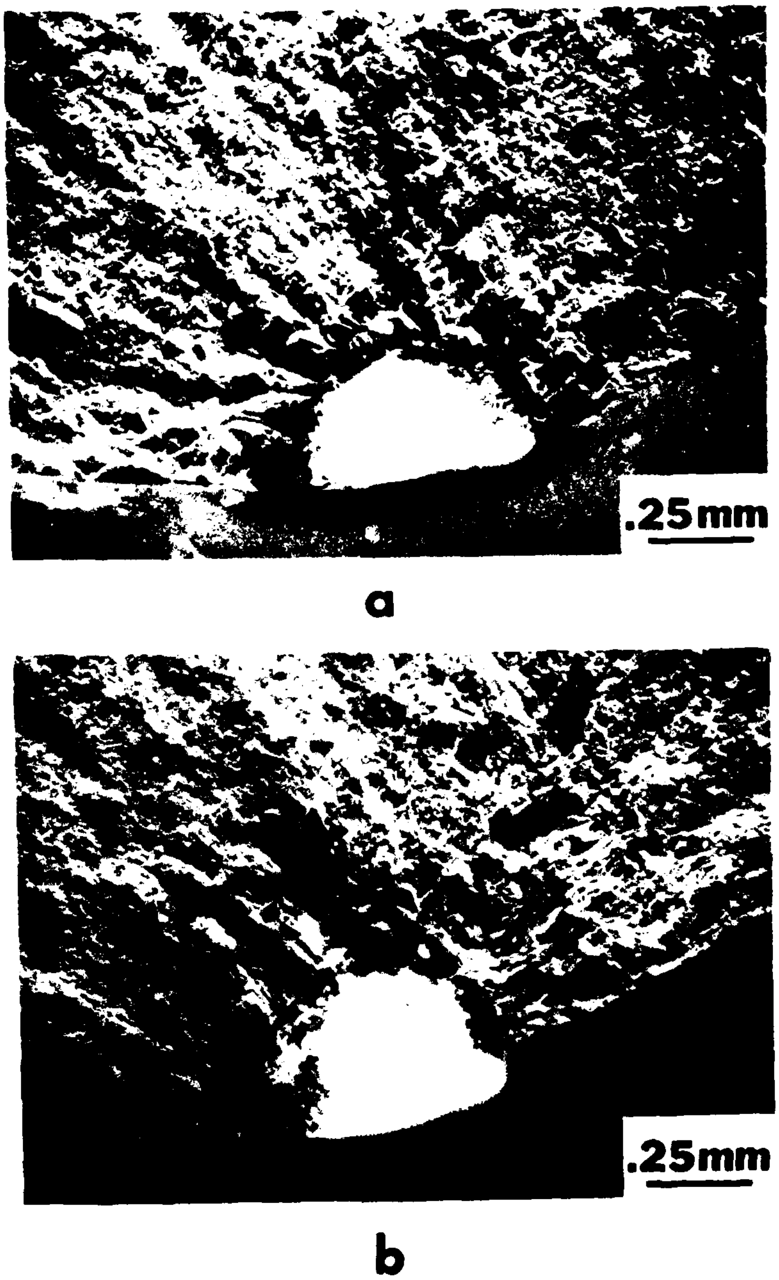

Figure 12 Fractographic features of MERL 76 specimens seeded with 0.51 mm diameter semi-circular alumina inclusions and tested at 20°C, 930 MPa (a) Specimen No. 229 after 23,768 cycles (b) Specimen No. 232 after 69,573 cycles.

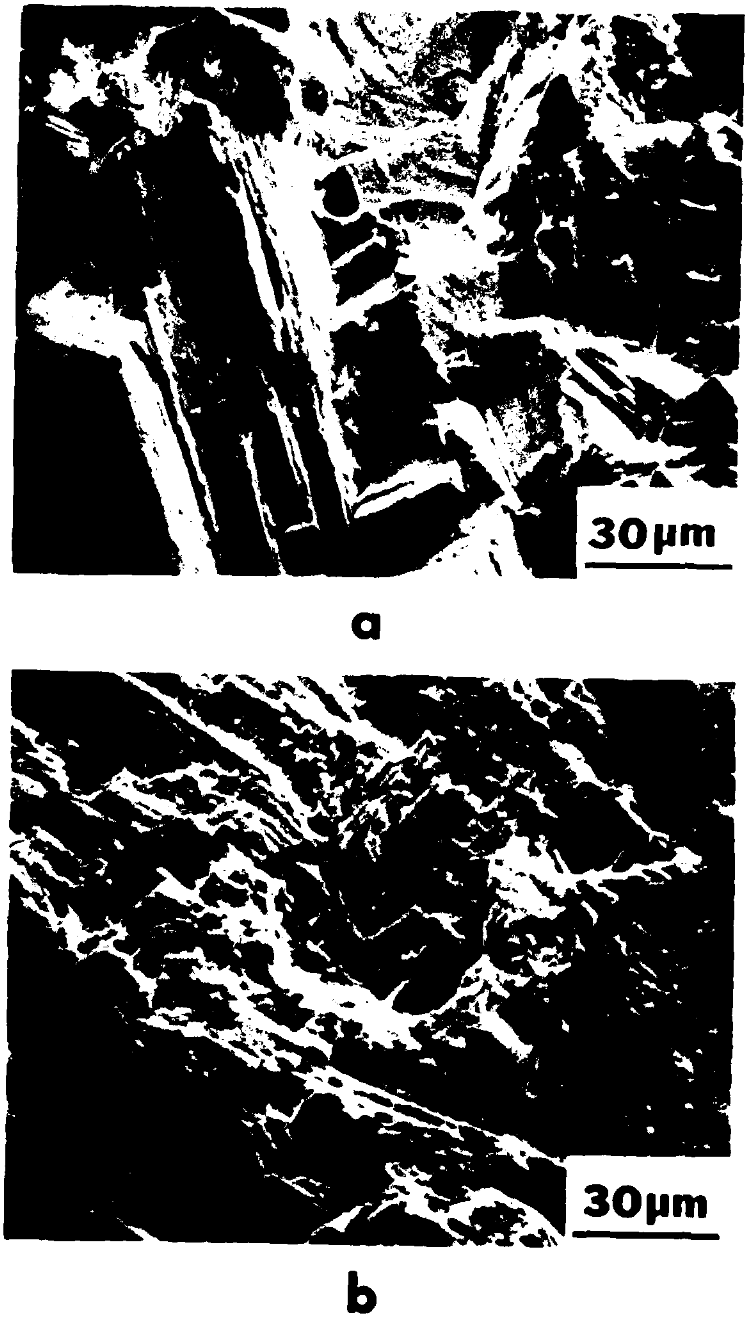
30μm
a
30μm
b

Figure 13 Detailed appearances of the specimens shown in Figure 12 (a) faceted area (b) featureless area.

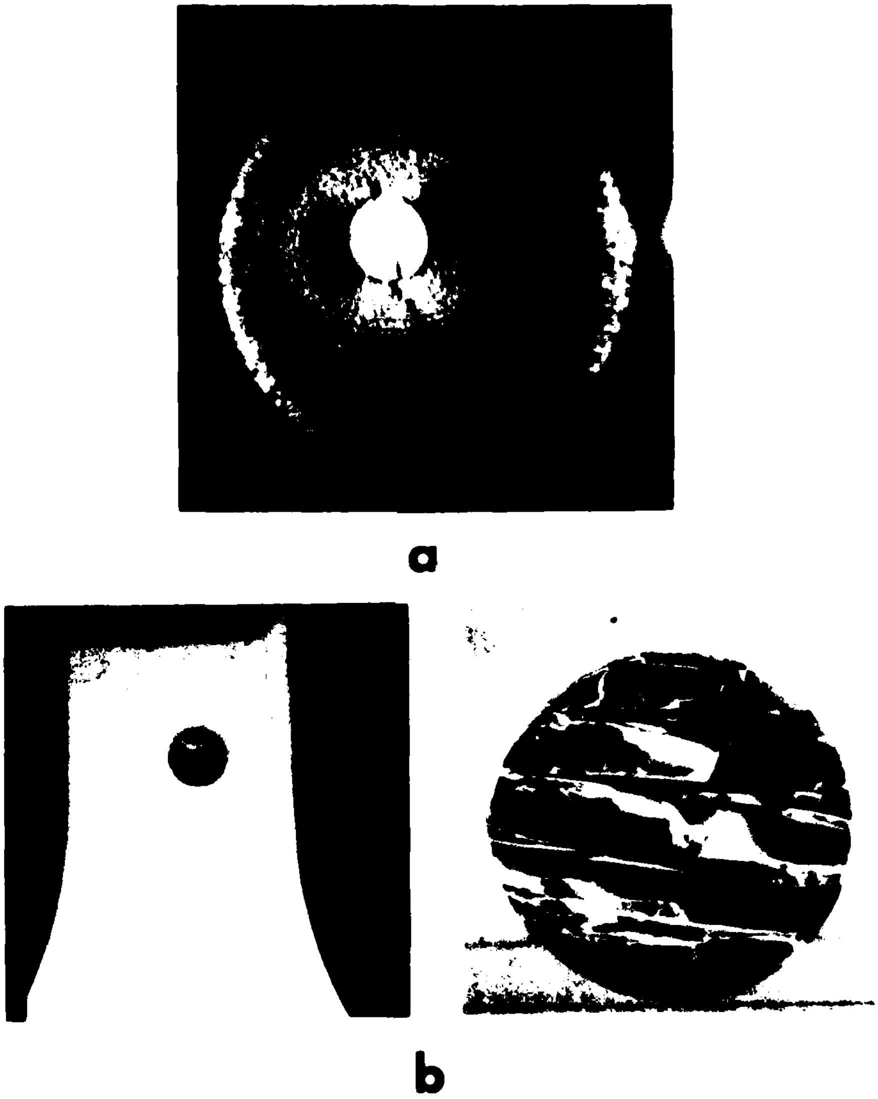

Figure 14 Appearances of (a) subsurface disk-shaped alumina inclusion (b) spherical alumina inclusion after fatigue fracture.

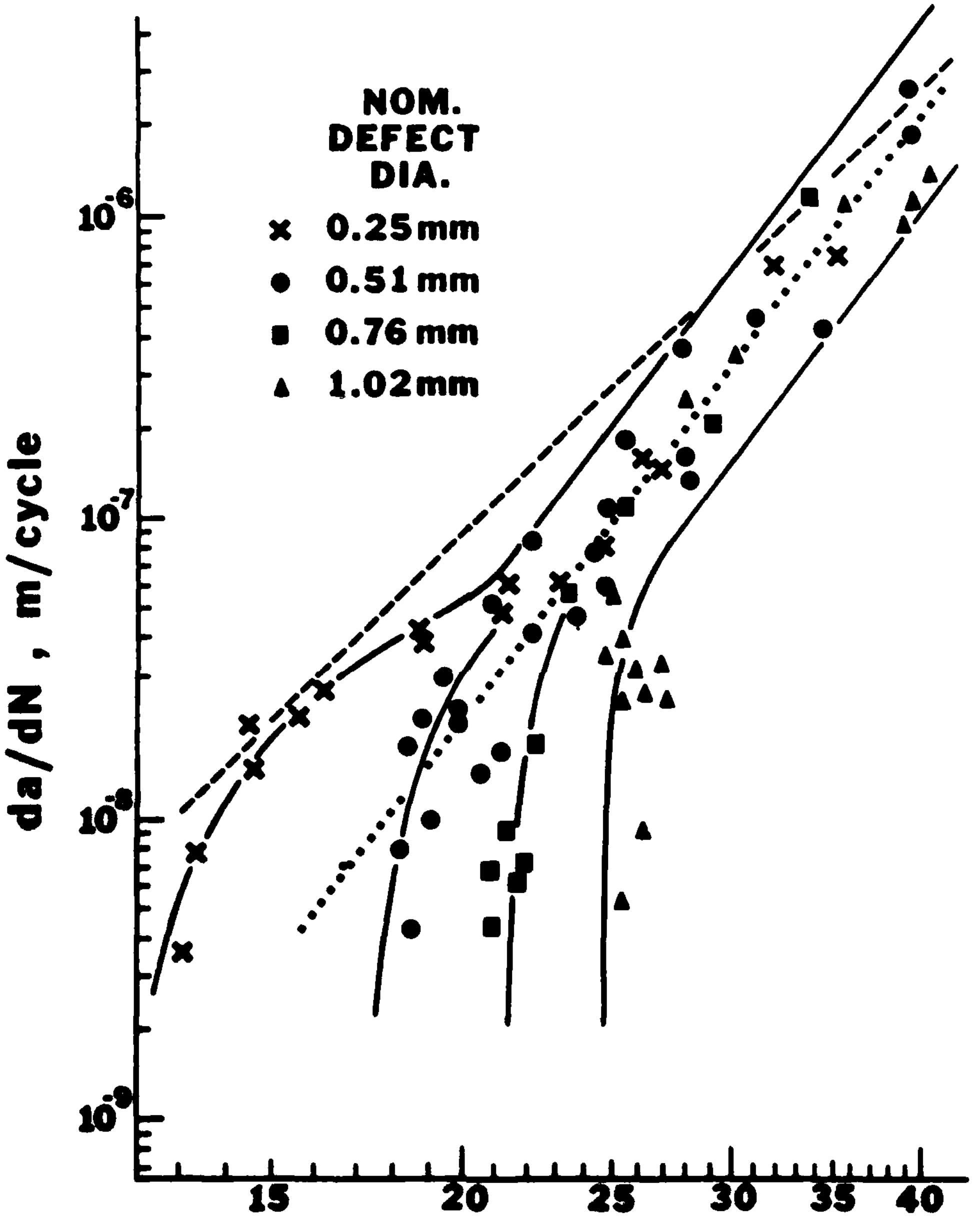

Figure 15 Propagation rates, da/dN versus the cyclic stress intensity factor, ΔK, for cracks emanating from semi-circular inclusions in MERL 76 at 20°C. The crack growth data for IN 100 from reference 10 is shown by the dashed line.

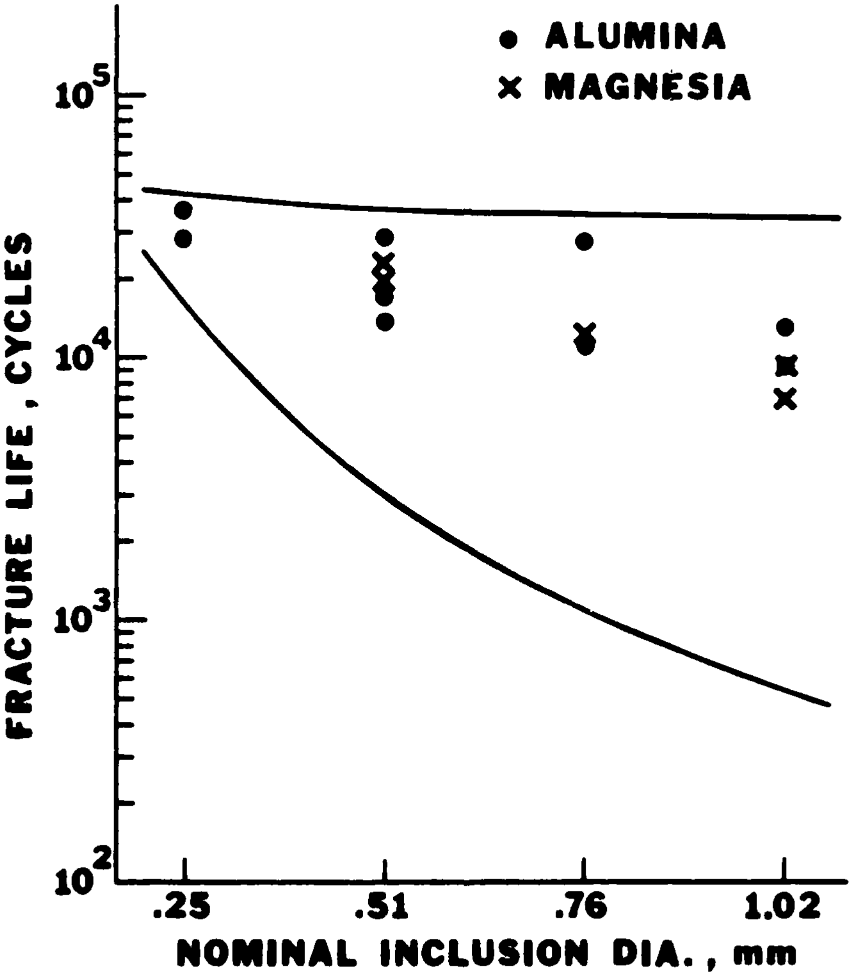

Figure 16 Fatigue lives of MERL 76 specimens containing semi-circular alumina and magnesia inclusions of various diameters tested at 20°C, 1068 MPa, R = 0.03, 2 Hz. The lower curve was calculated by assuming that an inclusion is equivalent to a crack. The upper curve was calculated by treating an inclusion as a notch.

ACKNOWLEDGEMENTS

The authors would like to thank A. E. Gemma, J. T. Hill, and R. N. Weber for their assistance in the numerical calculation of stresses and strains in a notch; Y. O. Chen for treatment of crack growth data and numerous fruitful discussions; F. T. Nardozzi for experimental assistance; J. S. LeShane for experimental assistance, drafting, and preparation of this report. In addition, several most helpful discussions held with Professor R. Raj of Cornell University are acknowledged.

The authors also wish to express their appreciation to Beverly J. Esson for her editorial comments and proofreading of this report.

END

DATE
FILMED

8-80

DTIC